Prefailure Behaviour of Rock at Rockburst Hazard Areas – Laboratory Investigations on Microacoustic Emissions

Dissertation

submitted to and approved by the

Department of Architecture, Civil Engineering and Environmental Sciences
University of Braunschweig – Institute of Technology

and the

Faculty of Engineering
University of Florence

in candidacy for the degree of a
Doktor-Ingenieur (Dr.-Ing.) /
Dottore di Ricerca in Risk Management on the Built Environment *)

by
Nadine Kimme
Born 13.03.1978
from Oldenburg, Germany

Submitted on	18 September 2009
Oral examination on	07 November 2009
Professorial advisors	Prof. Joachim Stahlmann Prof. Giovanni Vannucchi

2009

*) Either the German or the Italian form of the title may be used.

To Carsten &

to Ina and Annette

Acknowledgement

This present research work was carried out at the 'Institut für Grundbau und Bodenmechanik' of the Technical University of Braunschweig and at the 'Dipartimento di Ingegeneria Civile' of the University of Florence within the framework of the International Graduate College 'Risk Management of Natural and Civilization Hazards on Buildings and Infrastructures'. I thank the Deutsche Forschungsgesellschaft for the financial support within the PhD period.

Furthermore, I want to thank my tutors, Prof. Stahlmann and Prof. Vannucchi, for their support during my research work, for the fruitful discussions and for their helpful comments to my work. I say thanks to Prof. Langer for being the examiner of my research work and to Prof. Budelmann for being the chairman of my PhD defence.

Thanks to the Physikalisch Technische Bundesanstalt (PTB) in Braunschweig for the first suggestions to my measurement chain. Martin Oehler (EMG·TUBS), Marcus Petz and Thomas Bunkus (both IPROM·TUBS) as well as Bernhard Romanski and Markus Walbaum (both TEG mbH) gave important support for the data handling and data analysis. Particularly, Karl-Heinz Elmer (ISD·LUH) supported and encouraged me during the difficult stages of my thesis. Thanks a lot to all of you!

Special thanks go to Matthias Rosenberg and Christian Kuhn of the IGB·TUBS for the encouragement and support in the last phase of my research work. I gratefully thank Katharina Kluge for the fruitful comments on the written thesis. Grazie mille.

Last but not least: Thanks to the Italians and Germans that I got to know during my periods in Florence and in Braunschweig. You are friends for life! I do not want to miss it!

Grazie tanto! Thanks! Vielen Dank! Nadine Kimme

Abstract

A rockburst is the sudden and sometimes violent release of accumulated energy when a volume of rock is strained beyond its elastic limit. Rockbursts are mainly induced by mining activity and result in the emission of seismic signals transmitted through the rock. These seismic signals can be recorded by seismic sensors to receive information about the source of the event. Up to now, the monitoring of mining regions to detect stress changes and stress accumulations in rock uses incidences of occurrence and intensities of seismic events that occur due to mining activity. But the investigation of incidences of occurrence and intensities of seismic events does not permit a determination of the time of macroscopic failure. Within this research work, the occurring frequencies of microacoustic events are determined and analysed to find indicators for the approaching macroscopic failure of rock.

The first part of this work treats extensively the basics of rockbursts, fracture mechanisms and acoustic emissions. An overview about tectonic and non-tectonic earthquakes as well as mining induced rockbursts that occurred in the past is given at the beginning. The theories of fracture mechanisms and microcrack propagation, which lead to macroscopic failure, are introduced and described. Finally, microacoustic emissions and their fields of application are described by given examples and applications. Regarding these examples, it becomes obvious that measuring techniques can already give information about stress changes and stress accumulations in rock with the help of incidences of occurrence and intensities of microacoustic events. A prediction of the time of approaching rockbursts is yet not possible. The main focus of this research work is, therefore, the complement investigations of the frequency behaviour of microacoustic events of rock.

Within the second part, the carried out laboratory tests are introduced by the chosen material, the measurement chain and the data acquisition. To investigate the stress changes inside the material, uniaxial compression tests are carried out and the microacoustic events that are generated by the load application are especially analysed in the phase of prefailure. The phase of prefailure describes

the phase of the test in which already existing microcracks inside the specimen grow, interact and coalesce until the specimen fails macroscopically. The carried out laboratory tests are investigated by analysing the frequency behaviour – besides the incidences of occurrence and intensities – of the microacoustic events. It is presented that the frequencies change during load application. Hence, recorded signals and their spectra can be assigned to their state of fracture and their state of loading by investigating the frequencies of signal spectra of the microacoustic events. With these first investigations of their kind, specific indicators are found to identify the present state of fracture and loading.

Kurzfassung

Gebirgsschläge sind durch den Berg- oder den Tunnelbau induzierte seismische Ereignisse, die Bruchereignisse im Untergrund darstellen. Sie entstehen aus Spannungsakkumulationen infolge von Spannungsumlagerungen in Grubengebäuden und im Deckgebirge und resultieren aus der plötzlichen Entspannung des Gebirges unter Freisetzung hoher Energien. Durch lokales Überschreiten von Steifigkeiten brechen Bindungskräfte im Gefüge auf. Das Aufbrechen der Bindungen setzt u. A. elastische Energie frei. Die elastische Energie breitet sich in Wellen im Gefüge aus, die durch Aufnehmer an der Oberfläche registriert werden können. Die registrierten Ereignisse können Auskunft über Änderungen und das Verhalten innerhalb des Gefüges geben. Mithilfe messtechnischer Überwachung in Bergbaugebieten können bis zum heutigen Zeitpunkt Aussagen über Häufigkeiten und Intensitäten auftretender mikroakustischer Ereignisse gemacht werden. Allerdings ist eine Vorhersage zum Zeitpunkt des Versagens nicht möglich. In der vorliegenden Arbeit werden im Speziellen die auftretenden Frequenzen der emittierenden Wellen bestimmt und analysiert, um Indikatoren für die Vorhersage des makroskopischen Bruchs zu ermitteln.

Der erste Teil der Arbeit befasst sich umfassend mit den Grundlagen von Gebirgsschlägen, Bruchmechanismen im Gestein und mikroakustischen Emissionen. Ein Überblick zu tektonischen und nicht tektonischen Beben sowie bergbauinduzierten Gebirgsschlägen in der Vergangenheit leitet diesen Teil ein. Es werden Bruchmechanismen erläutert und die Theorie der Mikrorissausbreitung dargelegt, die zum makroskopischen Bruch im Gestein führt. Abschließend werden mikroakustische Emissionen und deren Anwendungsgebiete ausführlich behandelt. Es wird aufgezeigt, dass messtechnische Überwachungen in Bergbauregionen bereits eingesetzt werden, Vorhersagen über bevorstehende Gebirgsschläge allerdings nicht möglich sind, da sich die Untersuchung der mikro-akustischen Ereignisse auf deren Häufigkeiten und Intensitäten beschränkt. Die ergänzende Bestimmung und Auswertung der auftretenden Frequenzen mikroakustischer Ereignisse wird daher als Kernpunkt dieser Arbeit hergeleitet.

Im zweiten Teil der Arbeit werden die durchgeführten Laborversuche ausführlich beschrieben und dargestellt. Um die Spannungsänderungen des Gesteins genauer untersuchen zu können, werden einaxiale Druckversuche durchgeführt, die mit mikroakustischer Überwachung speziell das Vorbruchverhalten eines Kalksandsteines analysieren. Das Vorbruchverhalten kennzeichnet die Versuchsphase, in der sich einzelne, im Gefüge bereits existierende Mikrorisse verlängern und zu größeren Mikrorissen zusammenschließen, bis der Makrobruch eintritt. Die durchgeführten Laborversuche werden auf Häufigkeiten, Intensitäten und im Besonderen auf die auftretenden Frequenzen der mikroakustischen Ereignisse untersucht und analysiert. Es wird gezeigt, dass sich die Frequenzen der mikroakustischen Ereignisse während des Versuchsverlaufes ändern. Daher ist eine Zuordnung der mikroakustischen Ereignisse anhand ihrer Frequenzgehalte zur jeweiligen Belastungsphase bzw. zum Bruchzustand möglich. Diese Arbeit liefert die ersten Erkenntnisse dieser Art zum Frequenzverhalten mikroakustischer Ereignisse aufgrund einer einaxialen Belastung im Gestein.

Table of Contents

1 Introduction

Rockbursts are phenomena that are generated by a sudden relaxation of rock mass releasing high energies. They result from stress accumulations owing to stress rearrangements in cavities and in covering rock. Local exceedings of fracture strain in the rock mass are indicators for such stress accumulations which can be measured by microacoustic instruments. Rockbursts are locally linked because of man-made conditions and, thus, make them easier locatable than earthquakes.

Rockbursts occur in mining areas throughout the world. The most active rockburst areas were found to be in Poland, the Kola Peninsula in northern Russia, and South Africa; but rockburst areas in North America, Germany, Tajikistan and Japan have also been investigated. One of the largest rockburst – the strongest that has ever occurred as a result of mining activity – was the one near Völkershausen on March 13, 1989, in the Werra potash mining area of Thuringia in central Germany (see Fig. 1-1). Unfortunately, there were no previous indications that a failure would occur. The lack of indicators for occurring rockbursts is the main problem in the scientific research.

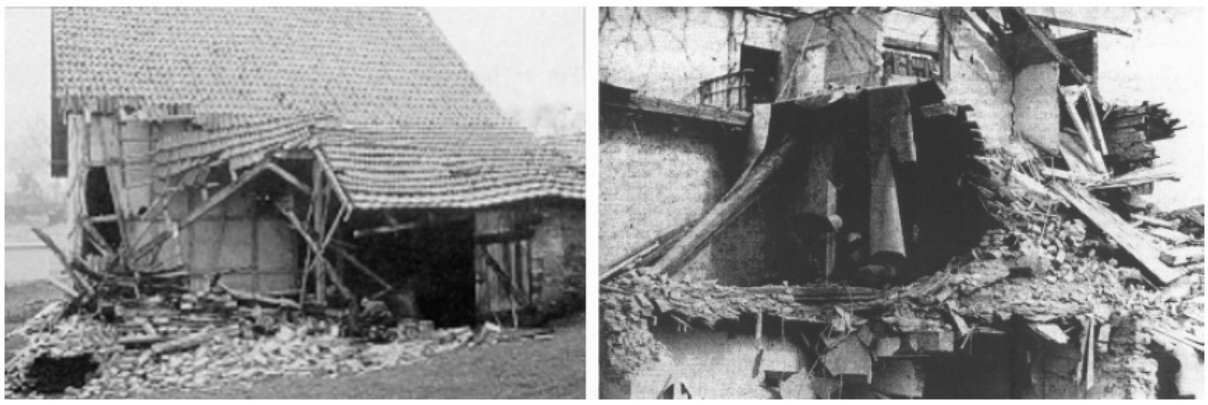

Fig. 1-1: Destroyed buildings in the village of Völkershausen directly above the fracture zone of the rockburst 1989 (MINKLEY et al., 2005)

1.1 Motivation

Underground mining has been one of the mankind's most dangerous pursuits. Since the early days of coal mining when methane explosions were by far the major killer and mining's most profound mystery, that rockbursts have been the mining hazard that is the least understood and the most feared.

In order to develop early warning systems, it is necessary to understand the fracture and failure mechanisms of rock. The mechanism of brittle behaviour of rock is characterised and determined by the propagation of cracks. These cracks release energy and elastic waves which can be recorded by sensors. Up to now, regions of mining areas are seismically monitored and the registered acoustic emissions are examined by analysing its intensities and incidences of microacoustic events. But there is a lack of knowledge about occurring frequencies during the different fracture processes.

The present work aims at analysing the occurring microacoustic events due to uniaxial, compressional loading by means of experimental investigations. The recorded microacoustic events are examined by their intensities, by their incidences and, mainly, by their frequency components of the signal spectra. The objective of this research work is to find specific indicators to assign the microacoustic events on the basis of their frequencies to the corresponding load phases and their state of fracture, respectively. This assignment permits a determination of the state of failure and the approaching macroscopic failure.

1.2 Hazard Assessment

According to the classic definition, a seismic hazard is any physical phenomenon associated with earthquake that has the potential to produce a loss (AKI et al., 2003). Hazard assessments of mining areas are helpful in evaluating the frequency of occurrence and intensity of the accompanying seismic events. Mining induced seismic events can cause strong ground motion and the seismic activity often occurs directly beneath urbanized and industrialized areas. Hazard assessment allows the adoption of measures to reduce both the risks and associated damage from seismicity. The seismic activity in a mine occurs in response to the accumulation of induced stress, e.g. due to properties of rockmass and / or due to various consequences of the applied mining technology. The seismic activity in a mine is related to the geological structures

as well as technological conditions of mining (HOLUB, 1997). Seismic risk calculations require information about the source of the hazard, the people or assets exposed to the hazard (‘elements at risk’) and the effects on these vulnerable elements if the hazard actually occurs (the potential consequences).

The hazard in this work is the accumulation of induced stress that cause seismic events in a mine. These seismic events, in turn, grow, interact and coalesce and may result in macroscopic failure of rock and rockbursting, respectively. The elements at risk that are exposed to the hazard are the mineurs or the machinery working below ground as well as urbanized and industrialized areas above ground. The potential consequences may be injuries or the death of mineurs and / or damage to machinery or areas above ground. To reduce both the seismic risk and associated damage, the present work consists of the investigation of microacoustic events to find basic indicators that describe the present stage of failure. The knowledge of this stage of failure may point to an approaching macroscopic failure and, hence, the risk can be reduced.

1.3 Methodology of Research

It is the aim of the present research work to examine and analyse the behaviour of the microacoustic emissions during a uniaxial compression test in the laboratory. The experiments are carried out on specimen of calcareous sandstone and the recorded emissions are analysed by investigating the intensities, the incidence of events and the occurring frequencies during the different fracture processes due to load application inside the sample. The test series carried out within this research represent the first investigations regarding the frequency behaviour of calcareous sandstone.

Chapter 2 contains an extensive literature review of the basics of rockbursts, fracture mechanisms and microacoustic emissions. It begins with a general overview about tectonic and non-tectonic earthquakes and gives examples of mining-induced rockbursts that occurred in the past. Next, the aspects of fracture mechanisms concerning this research topic are summarized. The theoretical and realistic strength of rock and the Griffith theory treat the subject that real materials contain imperfections which result in failure at much lower stresses than the theoretical strength. The formation and propagation of microcracks lead to macroscopic fracture, which is a result of the growth, interaction and coalescence of many microcracks, and to macroscopic strength, which can be

measured in the laboratory by means of the uniaxial and triaxial compression test. The last subsection treats the theory of acoustic emissions (AE) which are used to characterize rock due to different load applications. After the definition of AE, the application to laboratory studies and to in situ measurements is introduced.

The measurement chain which was developed within this research is presented and described in Chapter 3. The different components like the loading system, the chosen material, the acceleration sensors and the data acquisition system are introduced and their suitability for the carried out tests is presented.

Chapter 4 includes the basics and requirements for competent digital signal processing. The terms of sampling theorem and aliasing are introduced and explained. Furthermore, the theory of Fast Fourier Transform (FFT) and bandpass filtering is carried out. The measured data has to be converted into an acceleration signal concerning the factor of amplification and the specific sensitivity of the sensor. In the following, the principles of digital signal processing are applied to the laboratory test. The chapter concludes with the data processing by extracting the microacoustic emissions out of the acceleration signal and the analysis of microacoustic events with the FFT algorithm.

Chapter 5 treats the analysis of the recorded data with particular emphasis on the microacoustic emissions of specimens of calcareous sandstone due to quasi-static loading. The stress-time curves of the uniaxial compression test can be divided into different phases owing to characteristic sections of the shape of the curves. Each phase can be characterized by a specific fracture process inside the specimen which will be examined by the analysis of the recorded microacoustic emissions. The measured data during the different phases is examined by the analysis of the intensity, the incidence and the frequencies of the microacoustic events. The main investigation treats the signal spectra of the microacoustic events and their frequency behaviour during the different phases. The results gained from the test series are summarised.

Chapter 6 covers the conclusions on the results of the test series and the recommendations for future research topics.

The appendix covers the graphical representation of results of the test series.

2 Rockbursts, Fracture Mechanisms and Acoustic Emissions

A classical earthquake can be defined as a fracture process along a fault plane resulting from the release of elastic strain energy in the earth crust. But not all ground shaking can be related to a classical earthquake, since there are different types of seismic sources which can produce tremors. These can be mining induced events, reactions of the earth crust to extraction of fluids and gas, diffusion processes in the presence of water reservoirs, other human activities (ultrasonic beams, explosions, collapse of roadways, etc.) and landslides. The study of source mechanisms based on seismic records enables to find out, whether a seismic tremor is a 'classical earthquake' or not.

Non-tectonic induced seismic events are classified by their source. First, there are the mining-induced ones which are the major part of the non-tectonic events. For example (see Table 2.1), the opencast mining in Belchatow (Poland) triggered a man-made earthquake with a measured magnitude of 4.6. Furthermore, there are the reservoir-induced events which occur at dam heights greater than 100 m. So far, the largest and most damaging reservoir-induced earthquake was measured in Koyna (India) in 1967 with a magnitude of 6.5. It claimed over 200 human lives, injured 1,500 and rendered thousands homeless (GUPTA, 1992). The last of non-tectonic seismic events are the fluid-induced ones which have their origin in the abstraction of fluid (oil, water) and gas out of the underground or in the grouting of fluids.

Table 2.1: Man-made earthquakes and their magnitudes, from LENHARDT (1998)

Man-made Action	Highest Measured Magnitude	Epicentre (Extreme Example)
Opencast mining	4.6	Belchatow (Poland)
Deep mining	5.5	Völkershausen (Germany)
Reservoir	6.5	Koyna (India)
Gas / Oil-extraction	4.4-5.5	Denver (U.S.A.)

2.1 Terminology of Seismology

Several parameters are necessary to describe a seismic event. The most basic parameters are date and time, location and depth of the epicentre and magnitude or intensity. Only since permanent seismic stations were widely introduced, magnitudes could be determined. These few parameters may look very simple, they are often difficult to determine, however. In the following two subchapters, the terms intensity and magnitude are described.

2.1.1 Intensity – a Measure of the Effect

Effects on surface or underground of remote and local seismic events can either be measured by strong motion instruments or described by intensity scales. The latter scale groups similar and typical effects, which have been grouped by observers into twelve categories, usually called degrees. In many countries the European Macroseismic Scale 98 ‘EMS-98’ has been adopted to classify theses effects for different sites, from which reports could be gathered (GRÜNTHAL, 1998). These reports consist of descriptions on how human beings reacted, how objects were affected and if and how much damage buildings suffered.

This scale appears to have been superseded by the magnitude – but it has not. Although the magnitude can be calculated today almost instantly – that is within a minute whereas collecting macroseismic reports may take hours –, those reports are still collected with great interest by most seismological societies to create shake maps for civil protection purposes and to draw up descriptive scenarios.

According to SPONHEUER (1960), the intensity at a certain location, I_{local}, decreases with distance from the epicentre.

$$I_{local} = I_0 - 3 \log\frac{R}{z} - 1.3\,\alpha\,(R - z) \qquad (2\text{-}1)$$

with:

I_0 epicentral intensity ,

z focal depth in [km],

R distance from the hypocentre in [km],

α attenuation coefficient, usually ranging from 0 – 0.004.

Since intensities and magnitudes are frequently mixed up, care should be taken, when dealing with these values. Intensities are usually referred to as degrees, often stated in roman numerals and are devoid of decimals.

2.1.2 Magnitude – a Measure of the Source

For the years before instrumental data were at hand, magnitudes were estimated from intensities and the focal depth via empirical relationships. The epicentral intensity I_0 can be related to the seismic magnitude M via a scaling law as given by SHEBALIN (1958)

$$M = \frac{2}{3} I_0 + 2.3 \log z - 2 \qquad (2\text{-}2)$$

with:

z focal depth in [km].

Nowadays, seismic events are categorized by magnitudes. The magnitude scale was introduced by FRANCIS RICHTER in 1935 in California using the so-called Wood-Anderson torsion seismometer. According to the resolution of

ground motion of this instrument, RICHTER defined his magnitude-scale, whereby the magnitude represents a logarithmic measure of the released seismic energy at the source. Since the relation between the logarithm of this energy and the magnitude involves a factor of 1.5, a magnitude 6.0 event, for example, releases approximately 1,000 times the energy of a magnitude 4.0 event.

Today, these instruments are replaced by much more sensitive equipment and, hence, magnitudes can be measured which are even below a value of '0'. A magnitude below '-3', for example, corresponds to the opening of a new crack in a tunnel wall. In addition, different instruments were developed due to different measurement purposes which only record waves within specific frequency bands. This led to the introduction of several magnitude scales, such as body wave magnitudes, surface wave magnitudes, etc. each of which representing different frequencies of waves which could be observed at different seismic stations at different distances from the source. The most modern magnitude scale is the so-called 'moment magnitude' scale. It is determined from the frequency spectra of seismograms from so-called broad band stations, which means that these stations monitor ground motions over a very wide identical amplification. Such records can also be used to determine the mechanism of the source.

2.2 Tectonic Earthquakes

Friction of faults is often unstable and slip occurs rapidly as a rupture dynamically propagates over the fault surface. These sudden motions generate seismic waves and this is the mechanism of the most common and important type of earthquake.

The first clear connection between earthquakes and dynamic faulting and its relationship to tectonic processes was made by G. K. GILBERT in 1884. The extensive rupturing of the San Andreas fault during the 1906 San Francisco earthquake and the geodetic measurements finally led to the faulting theory of earthquakes as expressed in the analysis of that earthquake by REID (1910). The modern era of earthquake source studies began with the installation of the Worldwide Standardized Seismic Network in the early 1960s and with the widespread use of computers (SCHOLZ, 2002).

An earthquake may be considered to be a dynamically running shear crack. The energy balance of crack propagation, Equation (2-3), includes terms for the mechanical energy, the surface energy, the kinetic energy and the frictional work done on the crack surface behind the tip. Ignoring gravitational energy, the total energy of an earthquake is

$$U = \left(-W + U_e\right) + U_s + U_k + U_f . \qquad (2\text{-}3)$$

W is the work done by external forces, U_e is the change in internal strain energy. The combined term in parentheses is referred to as the mechanical energy. There is an expenditure of energy in creating the new surfaces U_s. U_k is the kinetic energy and U_f the work reaching against friction. A further consideration of the energy balance is given in chapter 2.4.2 within the GRIFFITH theory.

2.3 Non-Tectonic Earthquakes

In contrast to tectonic earthquakes, there are numerous perturbations to the Earth's upper crust that also result in earthquakes, the so-called non-tectonic earthquakes. Many of these perturbations are due to human activities, including underground mining, reservoir impoundment, liquid injection and fluid extraction. The causes of non-tectonic seismicity can be quantified in terms of at least one of the following: stress changes, pore pressure change, volume change and application or removal of a load. The seismicity can be classified as either induced or triggered. The adjective 'induced' applies to seismicity resulting from a substantial change in crustal stress or pore pressure from its ambient state; whereas 'triggered' describes a situation for which the crust is sufficiently close to failure state due to natural tectonic processes that only a small change in either stress or pore pressure stimulates earthquakes. For example, earthquakes due to deep, hard-rock mining operations are generally induced; whereas, those associated with reservoir impoundment are triggered. Generally the maximum magnitudes for induced earthquakes are determined largely by the scale of the causative activity and for triggered earthquakes by tectonic factors, such as pre-existing fault segments or the thickness of the seismogenic upper crust (MCGARR and SIMPSON, 1997).

Triggered seismicity occurs when the modification of the stress system by an external stimulant is sufficient to cause failure. This can occur because of either an increase in the stresses driving the fault or a decrease in strength of the fault. The strength of a fault, or the shear stress required for failure, can be expressed as

$$\tau = \mu(\sigma_n - P) + c' \qquad (2\text{-}4)$$

where μ is the coefficient of friction, σ_n is the normal stress across the fault, P is the pore pressure within the fault zone and c' is the cohesion. A fault may slip due to an increase in shear stress (τ) or, if the shear stress remains the same, a decrease in normal stress (σ_n) or an increase in pore pressure (P), as can be seen in equation (2-4).

2.3.1 Reservoir-Induced Earthquakes

By the early seventies, over a dozen cases of reservoir-induced earthquakes were known. In GUPTA (1992), a number of features are described which are characteristic for reservoir-associated earthquake sequences and which can be used to discriminate RIS (reservoir-induced seismicity) from the natural earthquake sequences in the same region. Over the years, the number of RIS cases has increased considerably and until now, more than seventy such cases are known. Although the phenomenon of RIS is not yet fully understood, it is clear that the stress changes caused by the reservoir are small and that a region must already be stressed close to failure for reservoir-induced earthquakes to occur.

The three main effects of reservoir loading relevant to induce man-made earthquakes are: (a) the increase of elastic stress that follows the filling of the reservoir; (b) the increase in fluid pressure in saturated rocks (due to the decrease in pore volume caused by compaction) in response to the elastic stress increase; and (c) pore pressure changes related to fluid migration. Most of the RIS sites exhibit these common characteristics, particularly during the initial phase of reservoir-induced earthquakes.

Reservoir loading may induce man-made earthquakes by an increase of pore pressure in the ground. The shear strength is related to the ratio of the shear

stress along the fault to the effective normal stress across the fault. The effective normal stress is equal to the normal stress minus the pore pressure. When the pore pressure increases, the shear stress is not changed, but the effective stress decreases by the amount of pore pressure. Therefore, the ratio of shear to normal stress increases. If rocks are under initial shear stress, an increase in pore pressure can trigger shear failure. Thus, earthquakes of induced seismicity may have been triggered by pore pressure changes.

Induced earthquakes occur in the immediate vicinity of a reservoir. Areas of low natural seismicity are most vulnerable since these are the sites where adequate precautions are not taken to build structures to resist earthquakes, large induced earthquakes have mostly occurred in such areas. In areas of high seismicity, reservoirs have less impact in changing the seismic regime and civil works are designed to withstand natural earthquakes. In an area of low seismicity, where the return period of the maximum expected earthquake may be thousands of years, an increase in the probability of triggering the largest expected earthquake during the lifetime of a reservoir will alter the risk estimate significantly.

2.3.2 Mining-Induced Earthquakes – Rockbursts

Rockbursts result of a sudden relaxation of rock mass releasing high energies. They result from stress accumulations owing to stress rearrangements in cavities and in covering rock. Local exceedings of fracture strain in the rock mass are indicators for such stress accumulations. Rockbursts are locally linked because of man-made conditions and thus, make them easier locatable than earthquakes.

Rockbursts occur in mining areas throughout the world; and, although their consequences are mostly not too serious, they have the potential for extensive damage. According to BENNETT et al. (2000), 104 historical rockbursts are reported in literature. Their locations are shown in Fig. 2-1.

The most active rockburst areas were found to be in Poland, the Kola Peninsula in northern Russia, and South Africa; but rockburst areas in North America, Germany, Tajikistan, and Japan have also been investigated. One of the largest rockburst – the strongest that has ever occurred as a result of mining activity – was the one near Völkershausen on March 13, 1989, in the Werra potash mining area of Thuringia in central Germany (see Chapter 2.3.2.1). Unfortunately, there were no previous indications that a failure would occur.

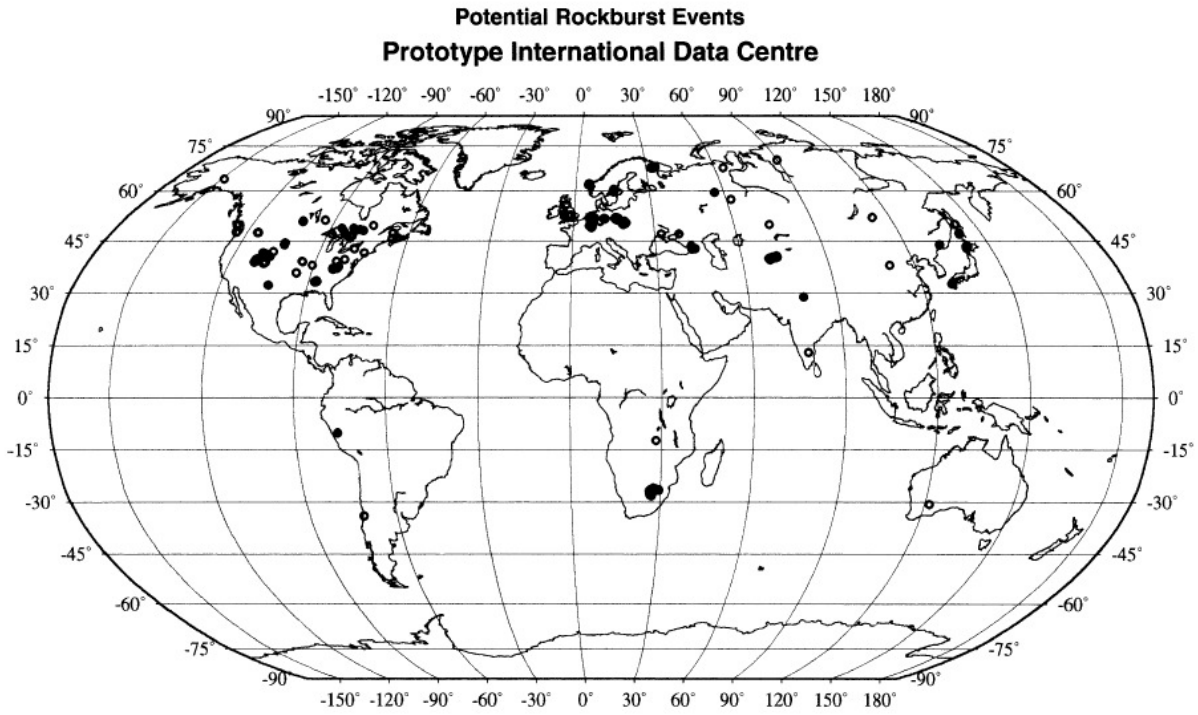

Fig. 2-1: Locations of 104 historical rockburst areas worldwide (BENNETT et al., 2000)

In order to develop early warning systems, it is necessary to understand the fracture and failure mechanisms of rock. The mechanism of brittle behaviour of rock is characterised and determined by the propagation of cracks, which may occur on all scales. The aim to understand the basic strength properties of rock has been a practical pursuit for a long time, both because of the importance of mining and because rock was the principal building material (SCHOLZ, 2002).

The history of rockbursts is as old as the mining itself. The first research started with the instruments with which the concussions could be recorded. In 1903, the first seismograph named after 'Wiechert' was installed in Pribram (Czech Republic). In 1910, there were the first recorded concussions with a 'Wiechert' in Witwatersrand (South Africa).

2.3.2.1 Rockbursts in the Past

In the region of the German district of potash mining, an amount of large rockbursts occurred in the past. There were rockbursts in Krügershall (May 24, 1940), in Heringen (22nd February 1953), in Merkers (8th July 1958), in Sünna (23rd June 1975), in Völkershausen (13th March 1989), and at latest in Teutschenthal (11th September 1996).

Rockburst near of Völkershausen in 1989

The rockburst near Völkershausen on March 13, 1989, in the Werra potash mining area of Thuringia in central Germany was the strongest that has ever occurred as a result of mining activity. Nearly 80 % of the buildings in Völkershausen, a small village situated directly over the rockburst field, suffered damage. The effects at the surface were disastrous; an example of damaged houses is depicted in Fig. 2-2.

Fig. 2-2: Damaged houses in Völkershausen after the rockburst (SIEBERT, 2004)

Nearly 6.8 km² of the extraction field which is located at a depth of 830 m in the mine 'Ernst Thälmann' were destroyed, 3200 carnallititic rock pillars were involved in the rockburst. Subsidence at the surface amounted to a maximum of 81 cm after 18 hours, with additional 5 cm in the following two weeks (AHORNER, 1998).

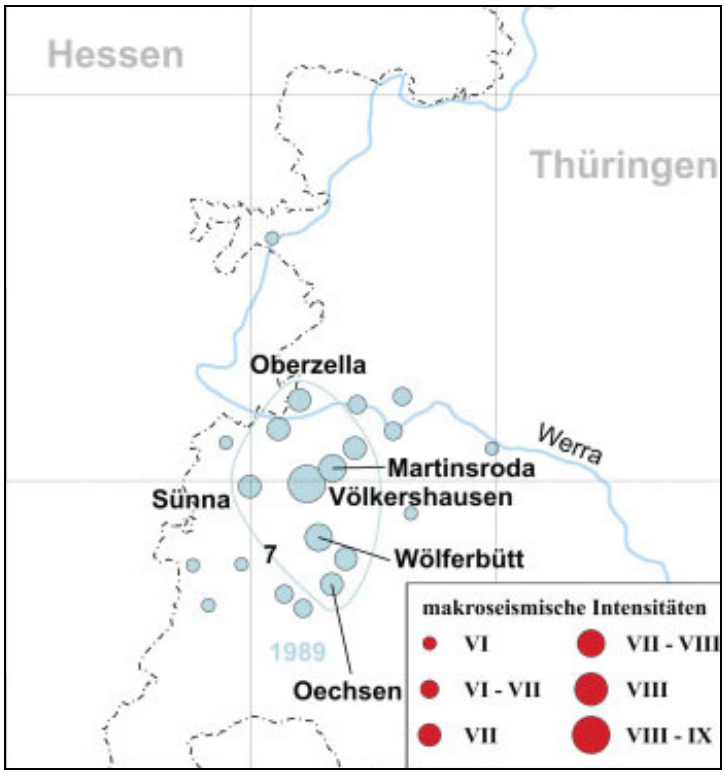

Fig. 2-3: Locations with observed intensities I greater than VI during the rockburst in the Werra potash mining district according to intensity assignments (GRÜNTHAL, 2005)

This corresponds to an intensity of VIII-IX on the MSK scale at the epicentre (see Fig. 2-3). The damage decreased rapidly with increasing distance from the epicentre, indicating a shallow seismic source. The vibrations were felt at a considerable distance away, especially in the upper floors of tall buildings.

A theoretical epicentral intensity, depth of focus and absorption coefficient were computed in an iterative procedure using KÖVESLIGETHY's formula (1907) on the basis of the radii of the isoseismal lines. The isoseismal lines ideally are concentrical circles around the epicentre whose radii increase with decreasing intensities. In Table 2.2, there are the pairs of variates (I_i, R_i) with $i = 1,...,n$, I_i as ith isoseismal line of intensity I and R_i as the depending radius of the isoseismal line in [km].

Table 2.2: Radii of the isoseismal lines

Intensity I	VIII	VII	VI	V	IV
Radius R in [km]	1.4	4.4	8.1	14.7	29.1

The formula by KÖVESLIGETHY (equation (2-5)), advanced and tested intensively by SPONHEUER (1960), describes the decrease of intensities I_i with the distances R_i to the epicentre depending on the epicentral intensity I_0, the focal depth z [km] and the absorption coefficient α [per km]:

$$I_i = I_0 - 3 \cdot \log\left(\frac{\sqrt{z^2 + R_i^2}}{z} \right) - 3 \cdot \alpha \cdot \log(e) \cdot \left(\sqrt{z^2 + R_i^2} - z \right) \quad . \qquad (2\text{-}5)$$

LEYDECKER et al. (1998) determined the three unknown values I_0, z and α in an iterative calculation method using the values of I_i and R_i of Table 2.2. The results, computed with equation (2-5) are:

epicentral intensity	$I_0 = 8.48 \pm 0.32$	MSK
focal depth	$z = 1.41 \pm 0.45$	km
absorption coefficient	$\alpha = 0.016 \pm 0.006$	km^{-1}.

The so-determined and observed intensity at the epicentre corresponded very well; and therefore, the epicentral intensity I_0 can be determined to $I_0 = VIII - IX$. But the computed focal depth of 1400 m is deeper than the known depth (about 830 m) of the mine galleries that collapsed. This can be explained by the shallow depth and wide area of the focus, which differs considerably from the point source assumed in KÖVESLIGETHY's formula.

The data of macroscopic quantities gives an insight into the damage of an earthquake which is not possible only regarding the magnitude of the event. The seismological findings clearly show that the Völkershausen rockburst was primarily caused by the failure of a group of pillars at the 800 m to 900 m level. These pillars consisted of carnallite, which is extremely brittle. They obviously were not strong enough to bear the weight of the overburden over a long period of time and collapsed due to the shock from blasting in the immediate neighbourhood of the unstable pillars a few seconds before the initial rockburst. Beginning with this event, the failure process spread out as an autodynamic chain reaction over the whole rockburst field destroying a total of 3200 pillars within an area of 6.8 km² in about 2.1 seconds (AHORNER, 1998).

Rockburst near Teutschenthal in 1996

The rockburst in the Saale potash mining district on September 11th, 1996, occurred without a considerable releasing event. An area of 2.5 km² of the mine structure collapsed in a depth of 700 m under ground level. The epicentral intensity of the rockburst was determined to VI-VII on the MSK scale and the local magnitude was $M_L = 4.8$. The maximum subsidence on the surface resulting from this rockburst event was 45 cm. Fig. 2-4 shows the macroscopic intensities of the rockburst region evaluated of the reports of damages and the questionnaires answered by the population.

The rockburst led to concussions of the ground surface which could be registered in a distance of thousand kilometres. The population sensed the concussions within a circuit of 80 to 100 km. The intensity of VII corresponds to a velocity greater than 200 mm/s. This intensity extended in an area of no housing. There were only little slope tumblings at the boundary of a nearby lake. The intensity of VI with a velocity of greater than 100 mm/s reached a circuit of 3 km and therefore, nearby villages. There were masonry cracks, collapses of chimneys, roofs, or gables.

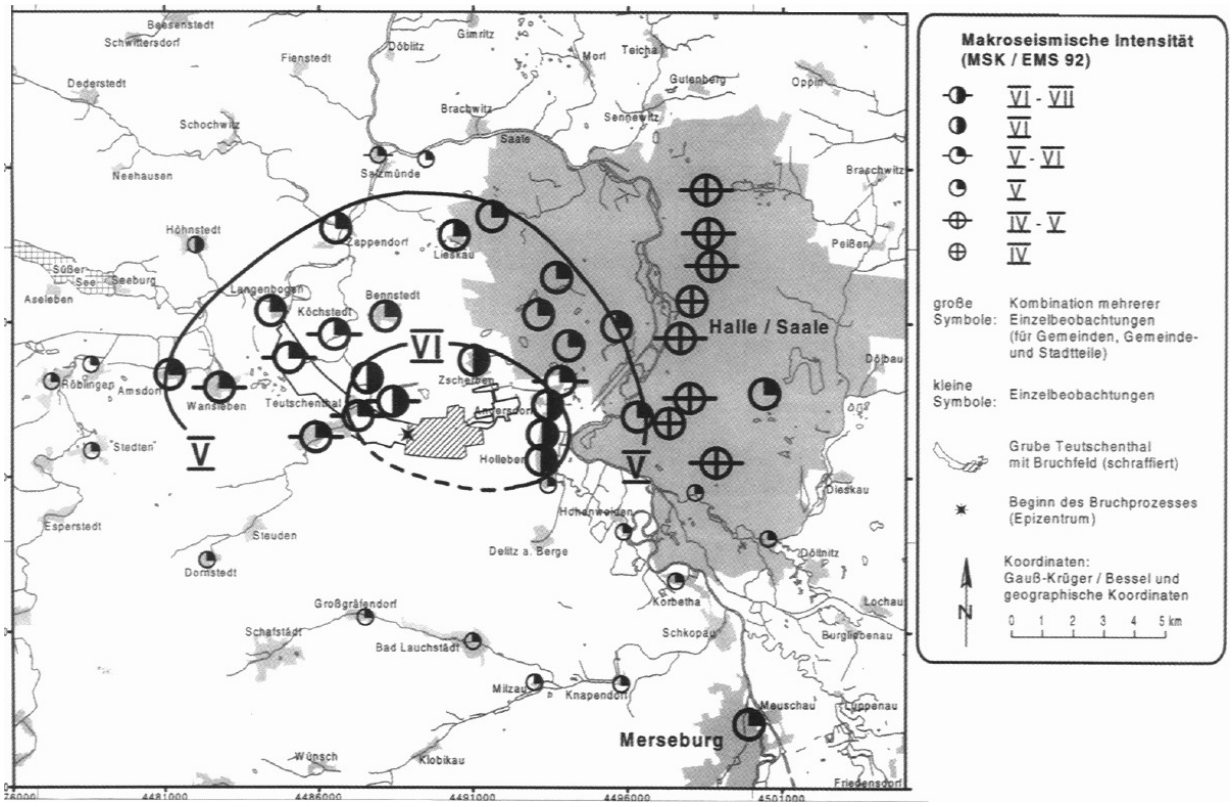

Fig. 2-4: Macroseismic map of the rockburst near Teutschenthal (BGR, 2005)

2.3.3 Fluid-Induced Earthquakes

According to MCGARR and SIMPSON (1997), one important aspect of cases of seismicity caused by injection appears to be that the injection takes place in a formation that has hydraulic connection to the fault zone on which the earthquakes occur. The earthquake activity is usually concentrated, in both lateral and vertical extent, near the bottom of the injection well. Thus the anomalous pressures are transmitted directly to the depths at which earthquakes occur. There is also evidence of hysteresis and time dependency in injection related seismicity. Initial stages appear to be concentrated near the injection point and respond rapidly to changes in injection pressure or volume. As injection proceeds, the zone of influence increases, earthquake magnitudes increase and the direct response to input pressure is obvious. For events close to injection point, activity usually stops immediately after the injection ends; whereas, events farther from the injection well may continue for some time after pumping stops. The mechanism which induces seismicity results from a decrease in effective normal stress caused by increased formation pressure.

One of the earliest and most spectacular examples of seismicity related to fluid injection occurred near Denver, Colorado in the 1960's (MCGARR and SIMPSON, 1997). Hazardous wastes were be injected under high pressures at depth of 3.7 km at the Rocky Mountain Arsenal. Soon after injection started, earthquakes began to be felt in the Denver area, a region that previously had shown little or no earthquake activity. The seismicity was initially concentrated near the bottom of the injection well, but eventually spread along a linear zone extending up to 5 km from the injection site. Activity continued for more than three years after injection ceased.

2.4 Fracture Mechanisms

Rock is not a manufactured material which was produced by specifications. It was influenced by extreme mechanical, thermal and chemical progresses over millions of years. Usually, rock is strongly structured and has a large number of interfaces. Hence, it is a discontinuum; and, therefore, there are different properties at various places and in different directions. Rock was one of the first materials for which strength was studied with scientific investigation because of its early importance as an engineering material.

There are different types of interfaces in rock. The interfaces change from microcracks to cracks, joints, and stratification plane and, finally, there exist faults. The knowledge about the geological origin of these discontinuities helps to understand the mechanical structure and the properties of the rock material. And besides the knowledge of rock properties before the failure, it is also quite important to get to know the behaviour after the failure of rock. To study the behaviour of rock, triaxial tests are used to determine properties as Young's elastic modulus, Poisson's ratio and the fracture criterion.

An external acting force and an exceeding of the rock strength yield to failure of the rock fabric. There are three types of failure mechanisms which can result from a triaxial shearing test, depicted in Fig. 2-5 as cleavage fracture (brittle fracture), shear fracture and fabric fracture.

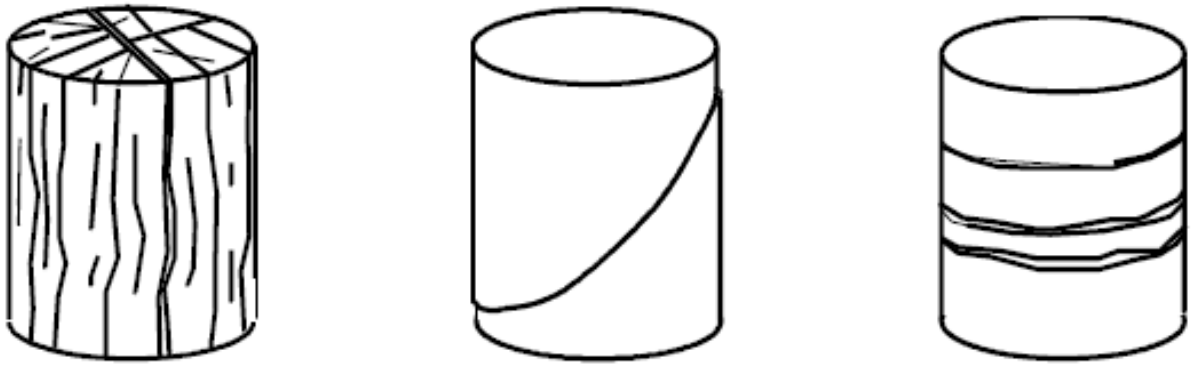

Fig. 2-5: Failure mechanisms of rock, (a) cleavage fracture, (b) shear fracture, and (c) fabric fracture (SCHUBERT, 2007)

A cleavage or brittle fracture occurs when rock experiences uniaxial compression without being stabilized by sufficient lateral pressure. The fracture is characterized by a sudden material failure without the occurrence of significant previous plastic deformations. It is well documented that brittle fracture involves the growth of microcracks from stress concentrations such as voids, inclusions and dissimilar grain contacts that result in contrast of elastic properties (LOCKNER, 1993). This irreversible damage results in both inelastic strain and acoustic emissions. This behaviour can be seen in Fig. 2-14 which shows the uniaxial compression of a rock sample under a confining pressure of 50 MPa. After an approximately linear elastic increase of the stress-strain-curve, a small branch of plastic deformation can be seen (in Fig. 2-14: a to b). Exceeding the maximum peak stress (b), the granite behaves in a rapidly sloping

way. Hence, the maximum strength is reached with only small plastic deformation.

Shear fracture (Fig. 2-5 (b)) is formed by triaxial loading; the angle of shear depends on the angle of friction and the geometrical boundary conditions, respectively. Shear fracture is a dislocation inside the grain skeleton, like yielding on a sliding surface.

In contrast to brittle and shear fracture, fabric fracture results from a uniform compression on the sample. There are no specified surfaces of failure but a destruction of the inner structure or the grains. An example can be seen in Fig. 2-5 (c).

2.4.1 Theoretical and Realistic Strength of Rock

The modern theory of brittle fracture arose as a solution to a crisis in understanding the strength of materials, brought by the atomic theory of matter. In simplest terms, strength can be viewed as the maximum stress that a material can support under given conditions. Fracture must involve the breaking of atomic bonds. An estimate of the theoretical strength of a solid is therefore the stress required to break the bonds across a lattice plane. In the simple anharmonic model of OROWAN (1949), this theoretical strength σ_t is approximately $E/2\pi$, where E is Young's modulus. The energy per unit area which is required for the separating of the planes by $\lambda/2$ is the specific surface energy γ

$$2\gamma = \frac{\lambda\sigma_t}{\pi} \qquad (2\text{-}6)$$

which yields the estimate $\gamma \approx E\lambda/4\pi^2$ with E, the Young's modulus and λ, the separation parameter which describes the range of interatomic force interaction. With $E = 30-60\,GPa$ and $\lambda = 10^{-10}m$, the energy required to break the bonds across a lattice plane, i.e., the theoretical strength of the rock equals to 5 – 10 GPa. Nevertheless, this estimate is several orders of magnitude higher than the real strength of this material. This discrepancy was explained by the postulation and later recognition that all real materials contain defects. Two types of defects are important: cracks, which are surface defects; and

dislocations, which are line defects. Both types of defects may propagate in response to an applied stress and produce yielding in the material. This already occurs at applied stresses much lower than the theoretical strength given above, because both mechanisms require that the theoretical strength be achieved only locally within a stress concentration deriving from the defect. The two mechanisms result in huge different macroscopic behaviour. When cracks are the active defect, material failure occurs by its separation into parts, often catastrophically: this is brittle behaviour. Plastic flow results from dislocation propagation, which produces permanent deformation without destruction of the lattice integrity (SCHOLZ, 2002).

2.4.2 Griffith Theory

All modern theories of strength recognize that real materials contain imperfections which – due to stress concentrations they produce within the body – result in failure at much lower stresses than the theoretical strength. A simple example, Fig. 2-6 (a), is a circular hole within a plate loaded with a uniform tensile stress σ_∞. It can be shown from elasticity theory that at the top and the bottom of the hole a compressive stress of magnitude $-\sigma_\infty$ exists and that at its left and right sides there will be tensile stresses of magnitude $3\sigma_\infty$. These stress concentrations arise from the lack of load-bearing capacity of the hole and their magnitudes are determined solely by the geometry of the hole and not by its size. If the hole is elliptical, as shown in Fig. 2-6 (b), the stress concentrations at the ends of the ellipse increase proportionally to the ratio of the semi-axes c/d (with $c > d$). The stress can be estimated to

$$\sigma \approx \sigma_\infty \left(1 + 2c/d\right) . \qquad (2\text{-}7)$$

It becomes clear that for a long narrow crack with $c >> d$ the theoretical strength can be attained at the crack tip also if $\sigma_\infty << \sigma_t$. Since the stress concentration will increase as the crack lengthens, crack growth can lead to a dynamic instability.

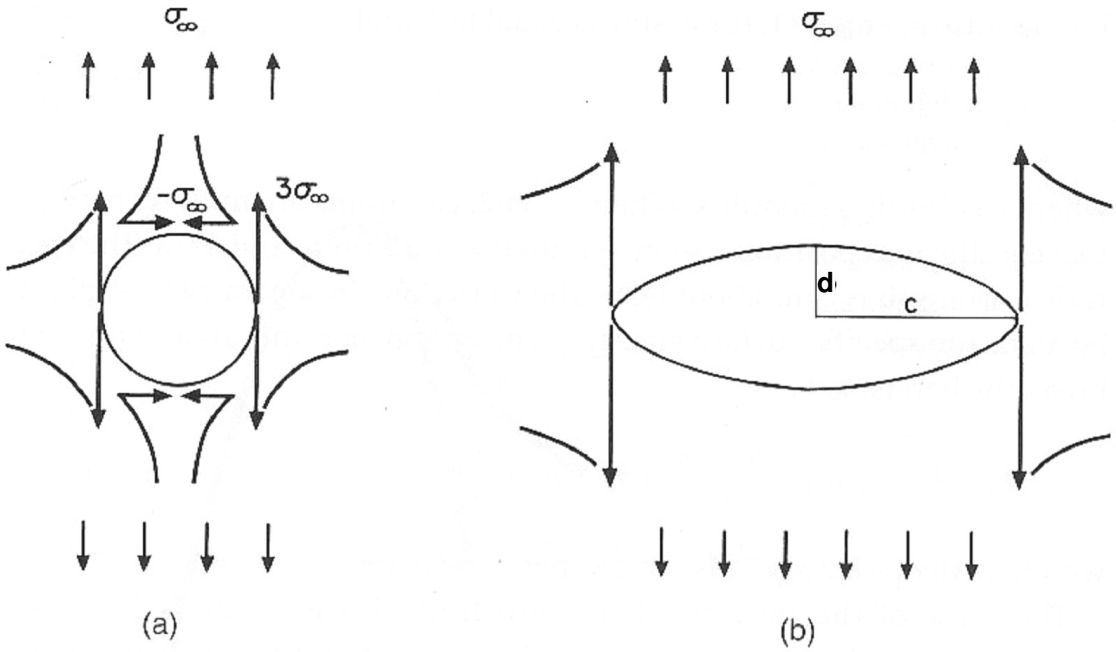

Fig. 2-6: Stress concentrations around (a) a circular hole and (b) an elliptical hole in a plate subjected to a uniform tension σ_∞ (SCHOLZ, 2002)

GRIFFITH (1920, 1924) posed this problem at a more fundamental level, in form of an energy balance for crack propagation. GRIFFITH analysed the case of a rod under uniform tension. The system he considered is shown in Fig. 2-7 (a) and consists of an elastic body that contains a crack of length $2c$. It is loaded by a stress σ applied on its external boundary. If the crack extends an increment δc, work W will be done by the external forces and there will be a change in the internal strain energy U_e. U_s is the surface energy involved in creation of the crack. Thus, the total energy of the system, U, for a crack, will be

$$U = \left(-W + U_e\right) + U_s . \tag{2-8}$$

The combined term in parentheses is referred to as the mechanical energy. It is clear that, if the cohesion between the incremental extension surfaces δc were removed, the crack would accelerate outward to a new lower energy configuration: Thus, mechanical energy must decrease with crack extension. The surface energy, however, will increase with crack extension, because work must be done against the cohesion forces in creating the new surface area. There

are two competing influences; for the crack to extend there must be reduction of the total energy of the system, and hence at equilibrium there is a balance between them.

The energy partition for the process is depicted in Fig. 2-7 (b). It can be seen that the crack propagates without limit when the position of unstable equilibrium is reached. The body fails macroscopically.

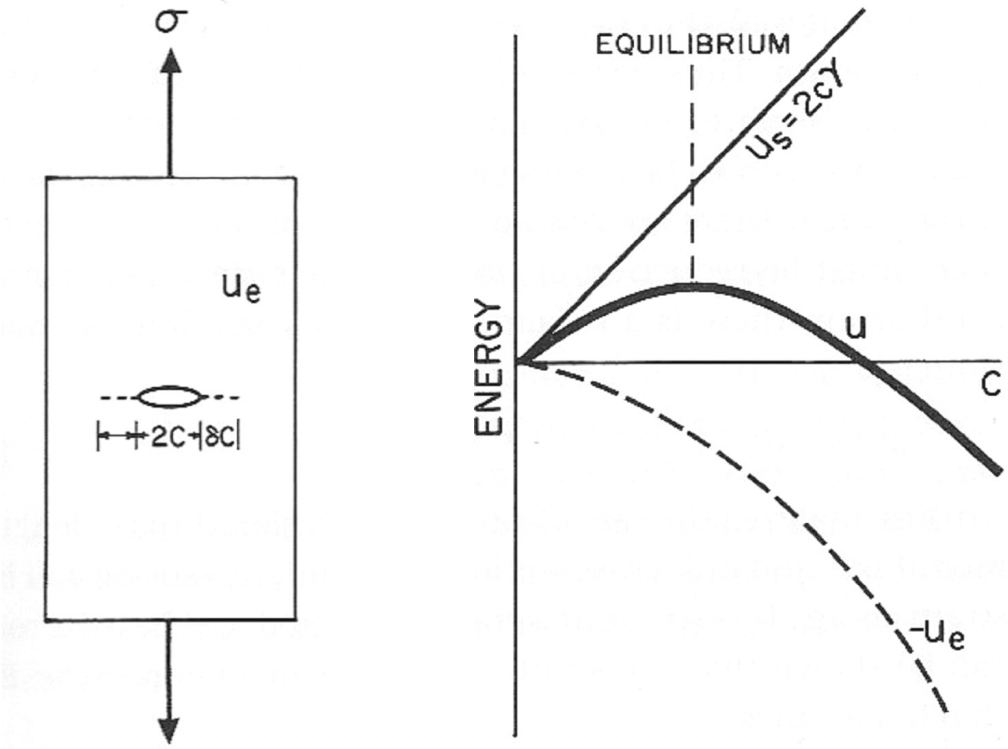

Fig. 2-7: GRIFFITH's model for a crack propagating in a rod (a), and the energy partition for the process (b) (SCHOLZ, 2002)

GRIFFITH (1920) and OROWAN (1949) posed the conditions for an enlargement of a static defect (crack), existing already in the fabric. Fracture in rock under compressive boundary loads is a result of the coalescence of many microcracks, not the growth of a single crack. Some crack configurations are more favourable for coalescence than others. As deviatoric stress increases and rock failure is approached, the microcrack population changes spatially from random to locally intense zones of cracking (KRANZ, 1983).

2.4.3 Strain Energy Rates

PERKINS and KREACH (1966) found that the rate of strain energy release for cracks propagating in sandstone increased as pressure increased, indicating an increase of resistance to fracture at higher pressure (KRANZ, 1983). Values of strain energy rates for minerals are in the range of 0.1 to 10 Jm^{-2}, while for rocks these values tend to be one to two orders of magnitude higher. The difference is most likely due to the fact that a small, but macroscopic crack propagating through rock has an apparent surface much less than the real area of a new surface created as it propagates through and around grains (FRIEDMAN et al., 1972).

2.4.4 Formation of Microcracks

Within the last 10 years, an enormous amount of work has been done to advance the knowledge about microcracks in rock. For obvious reasons, much of this work has been directed toward understanding how microcracks affect physical rock properties such as compressibility, strength, elastic wave velocities, permeability and electrical conductivity. Of equal interest are microcracks as separate entities: how they form, respond to various stress states, grow and interact, as well as their actual morphologies and population statistics. Studies of microcracks may be used to infer local stress domains. They may be used for comparisons between in situ and laboratory conditions, and because of apparent morphological and mechanical similarities between microcracks, joints and faults, they may be useful for geophysical scaling problems (KRANZ, 1983).

As stated by SIMMONS and RICHTER (1976), “cracks in the rock are produced when the local stress exceeds the local strength”. Local stress can be mechanically or thermally induced. The local strength can be increased, e.g., by stress concentrations at grain boundary contacts. Local strength can be reduced along cleavage planes, along grain boundaries and along any internal surface as a result of corrosion by chemically active fluids. In the absence of sufficient mechanically induced deviatoric stresses, differences in temperature, in time and space can cause microcrack nucleation by inducing requisite stresses. This is accomplished primarily through differential and incompatible thermal expansion (or contraction) between grains with different thermoelastic moduli or between similar, but misaligned anisotropic grains. In KRANZ (1983), the various means of mechanically and thermally induced crack nucleation and generation are described in detail and need not to be repeated here.

SIMMONS and RICHTER (1976) defined the word microcrack as:

> "an opening that occurs in rocks and has one or two dimensions smaller than the third. For flat microcracks, one dimension is much lesser than the other two and the width to length ratio, termed crack aspect ratio, must be less than 10^{-2} and is typically 10^{-3} to 10^{-5}. The length is typically in the order of 100 µm or less."

They subdivide microcracks into grain boundary cracks (associated and perhaps coincident with the grain boundary), intragranular or intracrystalline cracks (lying totally in the grain) and intergranular or intercrystalline cracks (extending from a grain boundary crossing into one or more other grains). The more detailed description of these crack types can be looked up in SIMMONS and RICHTER (1976).

2.4.5 Crack Propagation Modes

Linear elastic fracture mechanics is an approach that has its roots in the GRIFFITH energy balance, but that lends itself more readily to the solution of general crack problems. It is continuum mechanics approach in which the crack is idealized as a mathematically flat and narrow slit in a linear elastic medium. It consists of analysing the stress field around the crack and then formulating a fracture criterion based on certain critical parameters of the stress field. The macroscopic strength is thus related to the intrinsic strength of the material through the relationship between the applied stress and the crack-tip stresses. Because the crack is treated as residing a continuum, the details of the deformation and fracturing processes at the crack tip are ignored.

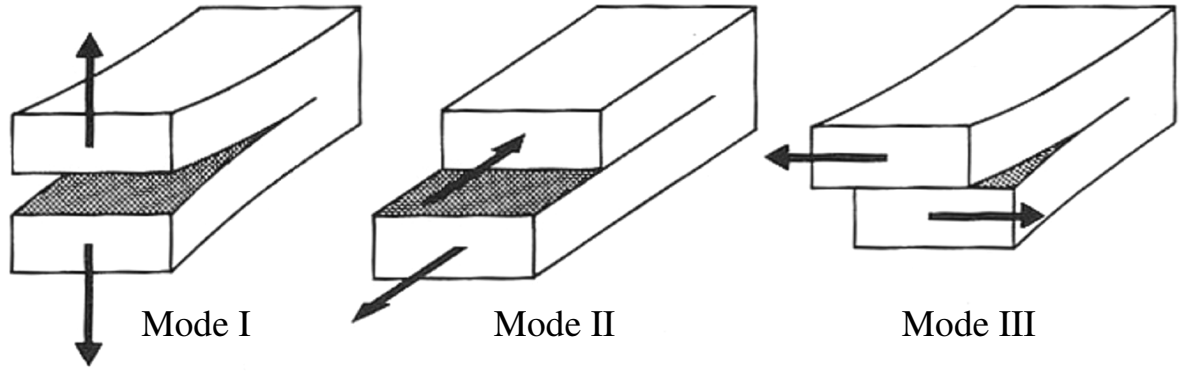

Fig. 2-8: The three crack propagation modes: Tensile mode (I), in-plane shear (II) and antiplane shea (III) (SCHOLZ, 2002)

The displacement field of cracks can be categorized into three modes (see Fig. 2-8). Mode I is the tensile, or opening, mode in which the crack wall displacements are normal to the crack. There are two shear modes: in-plane shear, Mode II, in which the displacements are in the plane of the crack and normal to the crack edge; and antiplane shear, Mode III, in which the displacements are in the plane of the crack and parallel to the crack edge. The latter are analogous to edge and screw dislocations, respectively.

2.4.6 Crack Paths

Generally, a crack tends to follow the local maximum stress trajectory, bending out of its initial plane, if necessary, to minimize shear stress effects and maximize the strain energy release rate. The presence of cleavage planes, pores, other cracks and inclusions will affect the crack propagation path by modifying the stress field in their vicinity or by introducing an anisotropy in local cohesive strength. Furthermore, the material discontinuity at a grain boundary can serve to arrest or deflect a propagating crack.

Since the rock and the local stress field are generally heterogeneous, continuum approaches to crack propagation in rock on the scale of interest here may not meet with desired success. Unless some sort of statistical approach is used, one may only get, at best, the trend of macroscopic crack paths (KRANZ, 1983).

2.4.7 Macroscopic Fracture

Fracture in rock under compressive boundary stresses is a result of the growth, interaction and coalescence of many microcracks, not the growth of a single

crack. Understanding crack interaction is therefore essential to understand the formation of fracture in rock (KRANZ, 1983). Early model studies of crack arrays (BOMBOLAKIS, 1964, 1968, 1973; HOEK ET AL., 1965) indicated that certain array configurations and orientations are more favourable for coalescence than others and that coalescence strongly depends on the distance between neighbouring cracks. Interaction of pairs of cracks has been studied with models and has been observed microscopically. The amount of crack overlap with respect to the maximum principal stress is a major factor in determining whether and how cracks link.

A large body of observational evidence now exists which indicates that if a deviatoric stress is raised on a rock sample, the microcrack population which is initially random spatially, becomes more and more localized and intense as the failure stress is approached. Microcrack population studies in limestone (OLSSON, 1974), sandstones (HOSHINO et al., 1970; SANGHA et al., 1974), granite (PENG et al., 1972; TAPPONNIER et al., 1976; KRANZ, 1979), gabbro (RONG et al., 1979) and quartzite (HALLBAUER et al., 1973) support this, as well as indirect measurements of surface strain (LIU at al., 1976; SOBOLEV et al., 1978; SPETZLER et al., 1981) and acoustic emissions (SONDERGELD et al., 1981).

Crack densities increase and appear to change from spatially random to non-random higher density regions as stress is increased and failure is approached. Significant high density locations of cracks do not appear until a few percent of the peak stress. The ratio of grain boundary cracks to intragranular cracks decreases at higher applied loads. The number of cracks generated prior to failure is greater at higher confining pressure, but for rock containing mostly calcite, cracking may be suppressed at higher pressures. Densities decrease rapidly, reaching the background level within a few grains away from a fault (KRANZ, 1983).

SCHOLZ (1968a) was one of the first to consider the failure of rock from a statistical viewpoint. His model assumes that local stresses in rock are randomly distributed but constant over small volumetric partitions, which have a specific strength. The distribution function for the local stress changes as the mean, applied stress changes. When the local strength is exceeded by the local stress, the region fails; a crack propagates and is arrested if it enters a region of higher

strength. In a subsequent paper (SCHOLZ, 1968b), time and frequency of cracking were introduced into the model.

2.4.8 Macroscopic Strength

The strength of rock is commonly measured in the laboratory by means of the uniaxial and triaxial compression test. Tensile strength can be determined by one of several direct and indirect means. Descriptions of the various experimental procedures can be found, for example in JAEGER et al. (1976) and PATERSON (1978). The two principal modes of failure are sketched in Fig. 2-9 (a) and (b). Fig. 2-9 (a) shows tensile failure involving parting on a surface approximately normal to the σ_3 axis induced by uniaxial and triaxial compression. Whereas Fig. 2-9 (b) shows shear on a surface inclined at an acute angle to σ_1. Apart from those failure modes, splitting parallel to σ_1 is often observed in uniaxial compression tests (Fig. 2-9 (c)); although this behaviour is suppressed by quite small confining pressure and it is not clear if it is an effect of end conditions or intrinsic fracture mode.

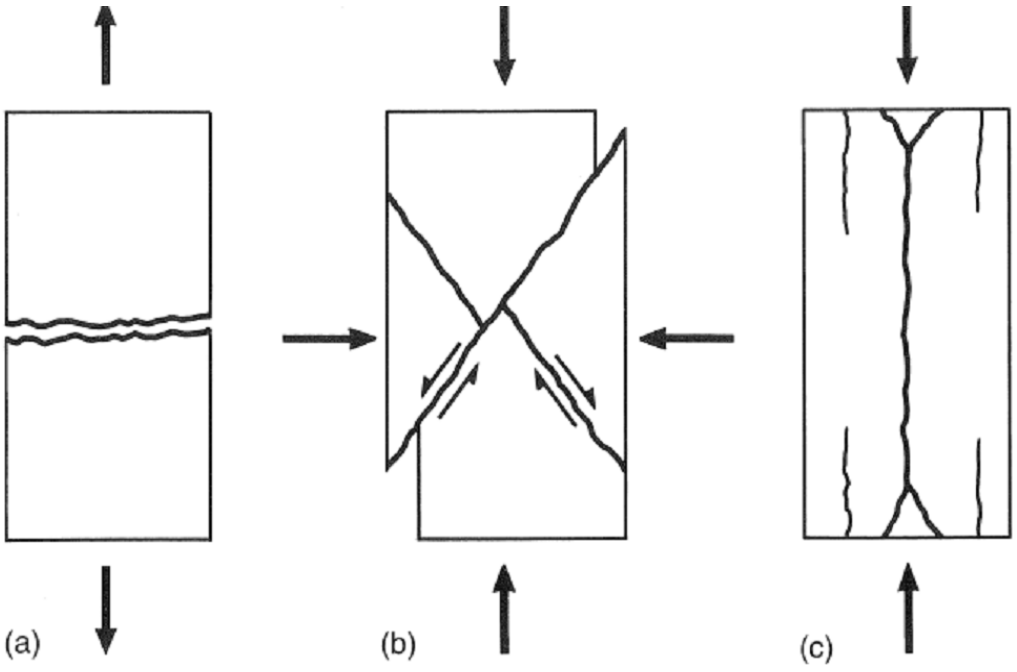

Fig. 2-9: Three modes of fracture: (a) tensile fracture; (b) faulting in a compression test; (c) splitting observed in a compression test at low confining pressure (SCHOLZ, 2002)

The nature of prefailure deformation may be understood by examining all strain components. In Fig. 2-10 axial and volumetric strain are plotted versus

deviatoric stress for a typical uniaxial compression test. These stress-strain curves can be divided into four characteristic stages (BRACE et al., 1966). Owing initial loading (Stage I) the stress-axial-strain curve is concave upwards and the rock undergoes more volumetric compaction than it would be expected from solid elasticity. This behaviour is caused by the closing of pre-existing cracks, primarily those oriented at high angles to the applied stress. This stage is not observed in triaxial compression tests, because the confining test pressure closes the cracks before stress is applied. After these cracks have largely closed, the rock deforms in a nearly elastic manner, according to its intrinsic elastic constants (Stage II).

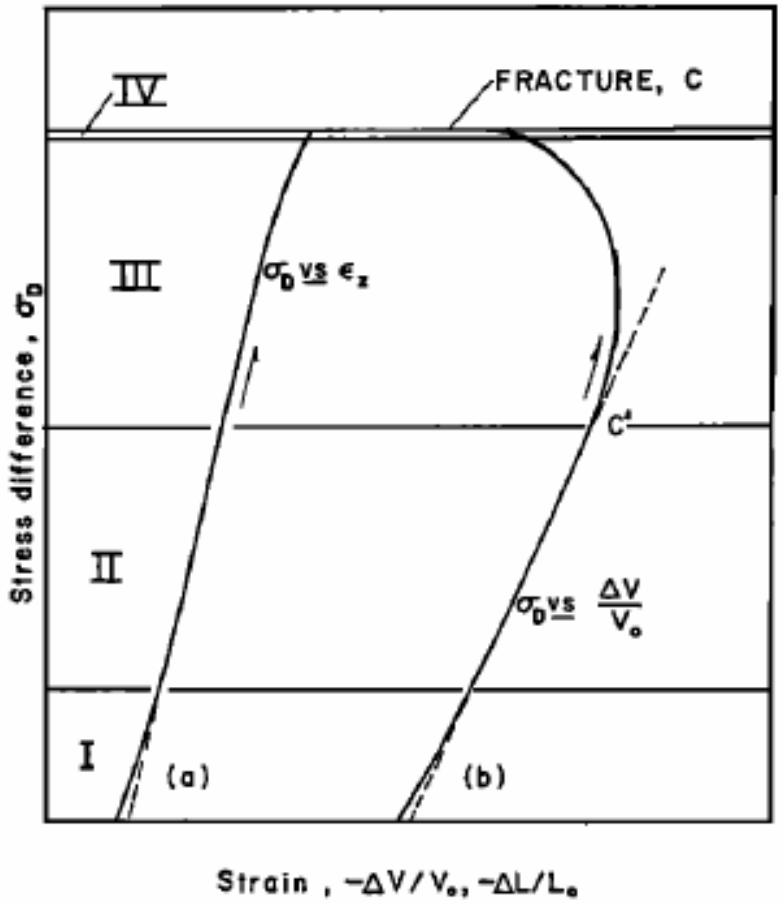

Fig. 2-10: Curves of stress versus axial strain (ε_z) and volumetric strain $(\Delta V/V)$ for a brittle rock in a compressive test to failure (BRACE et al., 1966)

At a stress commonly found to be at half the fracture stress, the rock is observed to dilate relative to what would be expected from linear elasticity (Stages III and IV). This is accompanied by a reduction to axial modulus, but is primarily due to nonelastic lateral expansion of the rock (not shown). The rheological property, in which volume dilation occurs as a result of application of deviatoric stress, is

called dilatancy. Prior to the work of BRACE et al. (1966), this was primarily understood as a property of granular materials. BRACE et al. (1966) interpreted it as being due to the development of pervasive microcracking within the rock, primarily in a direction parallel to σ_1, with a concomitant increase in void space.

2.5 Acoustic Emissions

Different measurement techniques are used to characterize rock. Those measurement techniques can be active or passive techniques. The active technique measures the rock properties using the ultrasonic pulses or artificial shots. By means of the received data, wave duration, and amplitudes of the compressional (P-) and shear (S-) waves can be determined. Seismic velocities of P- and S- waves and the attenuation of the amplitude on the wave path are calculated by the wave duration and the amplitudes. In the passive technique, the microcracks (acoustic emissions) in the medium are the seismic sources. The locations of the acoustic emissions are determined by the wave duration of the P- and S- waves. The intensity of acoustic emissions results from the amplitudes of the waves.

The passive and active proceedings complement each other. On the one hand, the active methods are used to determine the occurred dilatation which results from the formations of microcracks. From the passive methods, on the other hand, follows the intensity of the microfractures.

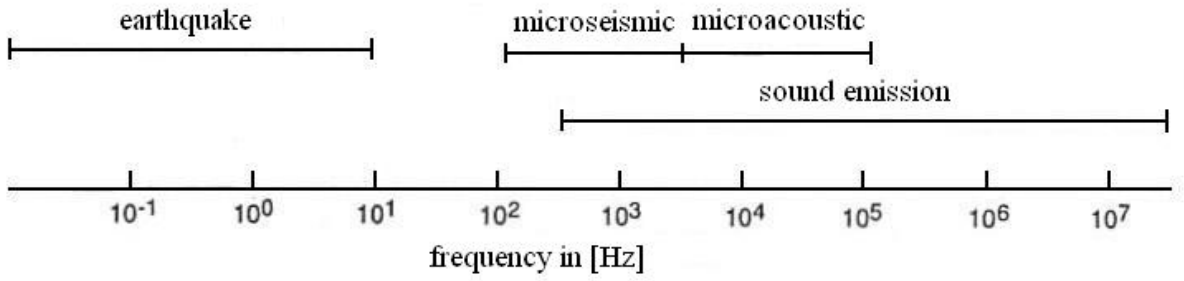

Fig. 2-11: Frequency ranges of earthquakes, microseismic, microacoustic and sound emissions (MANTHEI et al., 1993)

Examples of measurement techniques are microseismic, microacoustic and sound emission methods. They differ in the magnitude of their frequencies. The frequency ranges of different seismic sources are shown in Fig. 2-11 (MANTHEI et al., 1993). Frequencies in the hearing sound, up to 16 kHz,

belong to microseismic methods. They are used to observe mining regions (1-50 km). The microacoustic method is a higher-frequency measuring system (frequency range: 5-100 kHz). The localisation of the seismic sources is more precise and the sensitivity is higher. The sound emission measuring method uses frequencies above 100 kHz. Sound emission monitoring is a tool for observing induced fracturing and the response of a medium to applied stress (YOUNG, 1999).

2.5.1 Definition Acoustic Emission (AE)

LOCKNER (1993) defines an acoustic emission (AE) as a transient elastic wave generated by the rapid release of energy within a material. It is not surprising that in the geological sciences, significant overlap exists between the studies of AE and seismology. Both disciplines concern with the generation and propagation of elastic waves, although at different scales in source dimension and over different frequency ranges. Classical seismology has primarily been interested in seismic radiation from earthquakes greater than magnitude zero, having source dimensions from metres to hundreds of kilometres, and recorded frequencies below a few tens of hertz. Early AE studies in mines (OBERT, 1941; OBERT et al., 1942) were motivated by a desire to predict rockbursts and mine failures.

MANTHEI et al. (1993) gave a quite similar definition: If energy is released at a certain point in the specimen elastic waves are emitted. These elastic waves can be recorded by sensors. The sensors can be piezoelectric ones or geophones. The causes of releasing energy can be crack initiation, crack continuation or fracturing, friction events in a crack and plastic deformation. The dimensions range from macroscopic over microscopic to submicroscopic.

The acoustic signals that are generated during laboratory studies provide information about the size, location and deformation mechanisms of the events as well as properties of the medium through which the waves travel (e.g. velocity, attenuation and scattering).

2.5.2 AE in Laboratory Studies

In the laboratory, sample dimensions are typically less than a metre and limit the size of the largest possible fracture events. The most common acoustic emissions studied in the laboratory are controlled by flaws on the scale of the grain size so that most source events are less than a millimetre in dimension. As a result, laboratory studies are generally conducted in the 100 kHz to 2000 kHz range.

Laboratory deformation experiments appear to exhibit many of the foreshock and aftershock sequences first identified in earthquake studies. Focal mechanisms of AE source events have also been analysed with some success. Given the similarities between sequences of earthquakes and AE events, a primary aim of laboratory studies has been to investigate the fracture process with the intention of identifying precursory sequences that could be used as earthquake prediction tools (LOCKNER, 1993). Whereas earthquakes are generally assumed to occur on previously existing faults, the majority of AE studies are conducted on intact laboratory samples. LOCKNER (1993) gave a number of reasons that can be used to justify this approach: 1) It is likely that faults heal and strengthen between earthquakes (BLANPIED et al., 1991). 2) Natural faults are not smooth and must break through sections of rock where they interlock – in which case laboratory tests would model breaking of these local asperities. 3) Earthquake statistics and AE statistics are similar in many ways. 4) Slip on faults and fracture of intact rock involve the same micromechanical processes (LOCKNER et al., 1993).

2.5.2.1 Recording AE and Frequency-Magnitude Relation

The simplest detection system, and one that can easily be realized, involves attaching a piezoelectric transducer to the sample assembly and counting acoustic emissions. Since this technique gives equal weight to all detected events regardless of size, a common modification involves recording peak amplitude and coda length to obtain a rough estimate of the energy radiation by the event. The coda wave describes in seismology the part of the wave which follows after the arrival of the P-wave at an earthquake. Depending on the strength and in situ conditions, the coda can last a few minutes or in maximum longer than an hour.

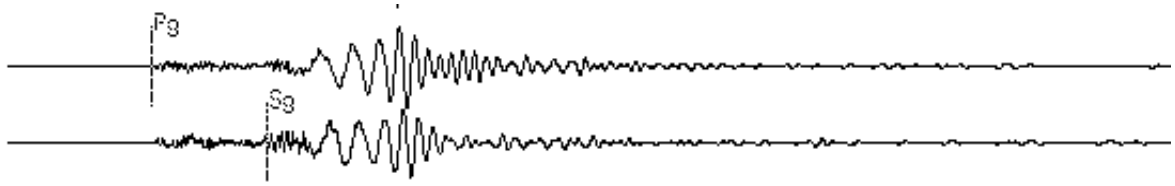

Fig. 2-12: Example of a seismogram after the rockburst in Teutschenthal, 1996 (BGR, 2005)

Fig. 2-12 shows two waves after the rockburst occurred in 1996 near Teutschenthal. The waves display the vertical (top plot) and the horizontal (bottom plot) components of the recorded seismogram. The first motions of the P- and S-wave are marked (P-wave at the top and S-wave at the bottom plot of Fig. 2-12). The decreasing later waves are termed coda waves. The analysis of seismograms gives information about the source mechanisms of an event.

With just a single transducer, however, no corrections can be made for attenuation and radiation pattern of individual events so that the energy estimates may not be accurate. Even so, since good correlations have been reported between inelastic strain rate and AE rate (MOGI, 1962; SCHOLZ, 1968c; LOCKNER et al., 1977b; MIZUTANI et al., 1985; LOCKNER et al., 1991), monitoring AE with a single transducer can be useful in describing the damage accumulation rate during a deformation test (HOLCOMB et al., 1986).

Apart from the correlation found between AE rate and strain rate, numerous studies have noted a power law frequency-magnitude relation for AE events (HIRATA, 1987; SCHOLZ, 1968a; WEEKS et al., 1978; CAI et al., 1988; IMOTO et al., 1986; MEREDITH et al., 1990; ZHAOYONG et al., 1990; SAMMONDS et al, 1992). This corresponds to the well-known GUTENBERG-RICHTER b-value relation for earthquakes

$$\log N(M) = a - bM \tag{2-9}$$

where N is the number of earthquakes with a magnitude greater than magnitude M and a and b are constants. MOGI (1962) and SCHOLZ (1968) have shown that microseismic activity follows the same trend and the b-value has been found to be characteristic of a material and its deformation mechanism. The AE magnitude M is calculated for each located event as given in (2-10) and (2-11):

$$M = \log\left(\frac{\sum_{m=1}^{n}\left(W_{RMS.d_m}\right)}{n}\right) \tag{2-10}$$

$$W_{RMS} = \sqrt{\frac{\sum_{i=1}^{x} W_i^2}{x}} \tag{2-11}$$

where n is the number of sensors and d_m is the distance between receiver m and the AE location. W_{RMS} is the 'root mean square' (RMS) waveform amplitude calculated on each receiver, using the waveform amplitude W at each point i, averaged over x data points (THOMPSON et al., 2006).

Different attempts have been made to explain the apparent universality of Eq. (2-9). EVANS (1978) noted that the amplitude of a stress wave can be related to the tensile stress. Further, he noted the strong sensitivity of the stress wave amplitude on crack size. EVANS (1978) derived the following equation to describe the microcrack distribution

$$\log\Phi(V) = a - \beta \log V \tag{2-12}$$

with an expected event amplitude distribution $\Phi(V)$ and β as a shape parameter. This Eq. (2-12) is equivalent in form to the GUTENBERG-RICHTER Eq. (2-9).

With regard to the frequency-magnitude relations (Eqs. (2-9) and (2-12)), numerous studies, e.g., MOGI (1962), have confirmed this general feature of AE amplitude distributions. Most of these studies were motivated by the expectation that changes in the b-value occur prior to failure and, therefore, could be used for failure prediction. However, the laboratory tests showed that one difficulty in using the b-value to predict failure is that detectable changes in b are generally the result of large changes in stress. This places strong constraints on the nucleation region of an earthquake. Indeed, prior to failure in many laboratory samples, inelastic deformation occurs at nearly constant stress. In addition, the amount of strain-weakening observed in some rock types prior to failure may be

significantly reduced when loaded in a compliant system such as the earth. Recent studies, for example, LOCKNER et al. (1992), found that prefailure decreases in b-value were not consistently observed in a series of fracture tests on granite and sandstone samples.

According to LOCKNER (1993), it is possible to predict failure in the laboratory: once the failure envelope for a rock is determined, failure can be determined from the stress history. Even without knowledge of the failure envelope, increasing strain rate and acoustic emission rate are good indications of approaching failure. Furthermore, he states that the shift from uniform microcracking associated with grain-size or subgrain-size flaws to the growth of a macroscopic fracture represents a jump in scale of flaw size. An isolated microcrack in an overall compressional stress state cannot grow indefinitely without the continued application of strain energy. Thus, macroscopic faulting appears to be the culmination of a process dominated by crack interaction.

LOCKNER (1993) states, since AE is a natural by-product of brittle fracturing and microcrack growth, analysis of AE signals is well suited to studying the processes occurring at the grain scale. The strong correlation between AE activity and inelastic strain has been used to measure damage accumulation in brittle rocks.

2.5.2.2 AE during Compressive Tests

BRACE et al. (1966) loaded a rock sample in a triaxial compression test. The curves of stress versus axial strain and volumetric strain are depicted in Fig. 2-10. SCHOLZ (1968a) analysed the acoustic emission (AE) that occurs during compressive failure experiments. The results confirmed the interpretation of the strain data. As shown in Fig. 2-13, AE begins at the onset of dilatancy and this activity accelerates in proportion to the rate of dilatancy in Stage III, as shown in Fig. 2-10. Stage IV is distinguished from Stage III because there is often an observed localization of both deformation and acoustic emission in this stage (SCHOLZ, 1968b; LOCKNER et al., 1977a; SOGA et al., 1978; SONDERGELD et al., 1982). Stage IV thus appears to involve the coalescence of microcracks leading to the formation of the macroscopic fracture.

Strain data as shown in Fig. 2-10 indicate that most of the microcracks responsible for dilatancy are nearly parallel to the maximum principal stress

direction. Scanning electron microscope (SEM) examination of specimens following their stressing to various stages prior to failure has confirmed the majority of axial cracks among those that are stress induced (TAPONNIER et al., 1976; KRANZ, 1979).

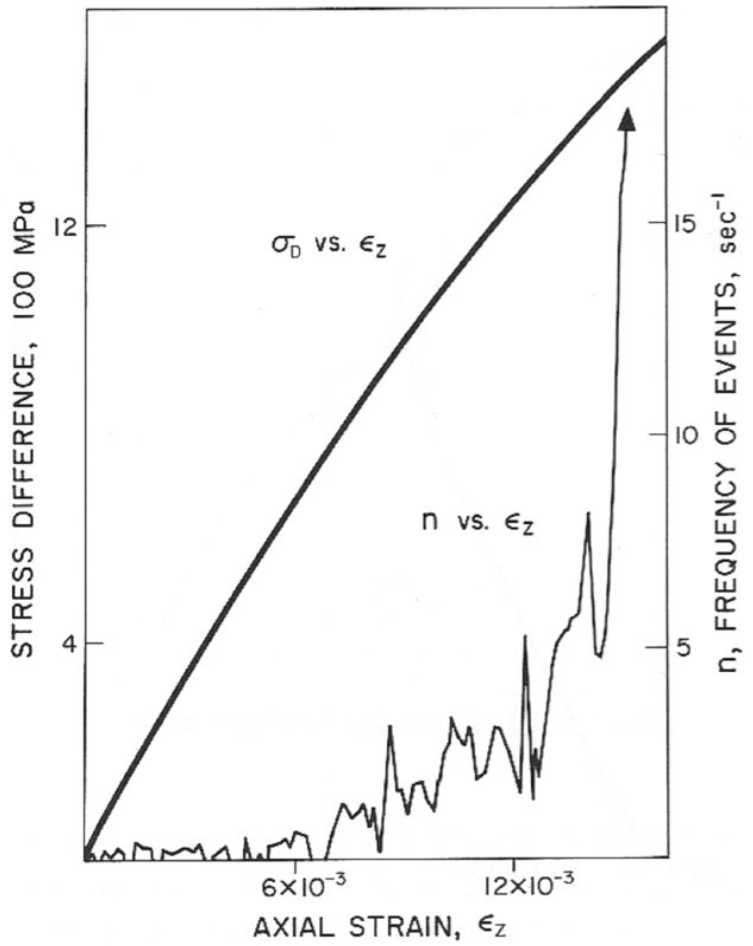

Fig. 2-13: Acoustic emission observed during the brittle fracture of rock in triaxial compression (SCHOLZ, 1968A)

The use of a dynamically stiffened testing machine allows the observation of the complete stress-strain curve as it is shown in Fig. 2-14. With normal testing apparatus, the experiment would be terminated by instability just after the peak stress (b), depicted in Fig. 2-14. In the experiment of LOCKNER et al. (1991), AE events were located in the specimen, and these locations are shown in Fig. 2-15, keyed to the stages in Fig. 2-14.

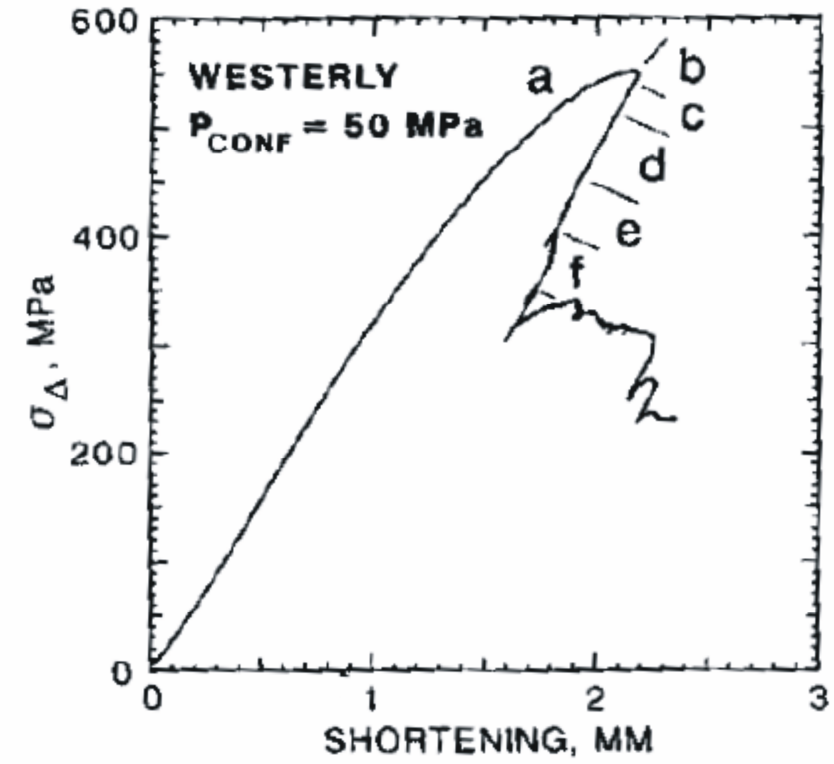

Fig. 2-14: Stress-strain curve of Westerly granite (LOCKNER, 1993)

In Fig. 2-15, there are the six stages during the compressional test of a sample of Westerly granite. The panels show the side view of the sample; and the lower panels are orthogonal from the upper ones. The nucleation and growth of the fault are seen from the localization of the AE. At the beginning of fracturing, AEs are widely distributed in the sample (a). Compared with Fig. 2-14, it as the linear elastic stage of the stress-strain curve of the Westerly granite. A narrowing of this AE process zone near the peak stress (b) was observed and appeared to be the nucleation of a fault inclined to the specimen axis. As failure proceeded along the postyield curve (c-f), the AE events indicated that the fault propagation gradually across the specimen until it completely transected the specimen (f). The strength plateau after point (f) in Fig. 2-14 represent the frictional strength of the fault that had been created. Thus, in forming the fault, there was substantial stress drop, from the yield point to the residual frictional strength.

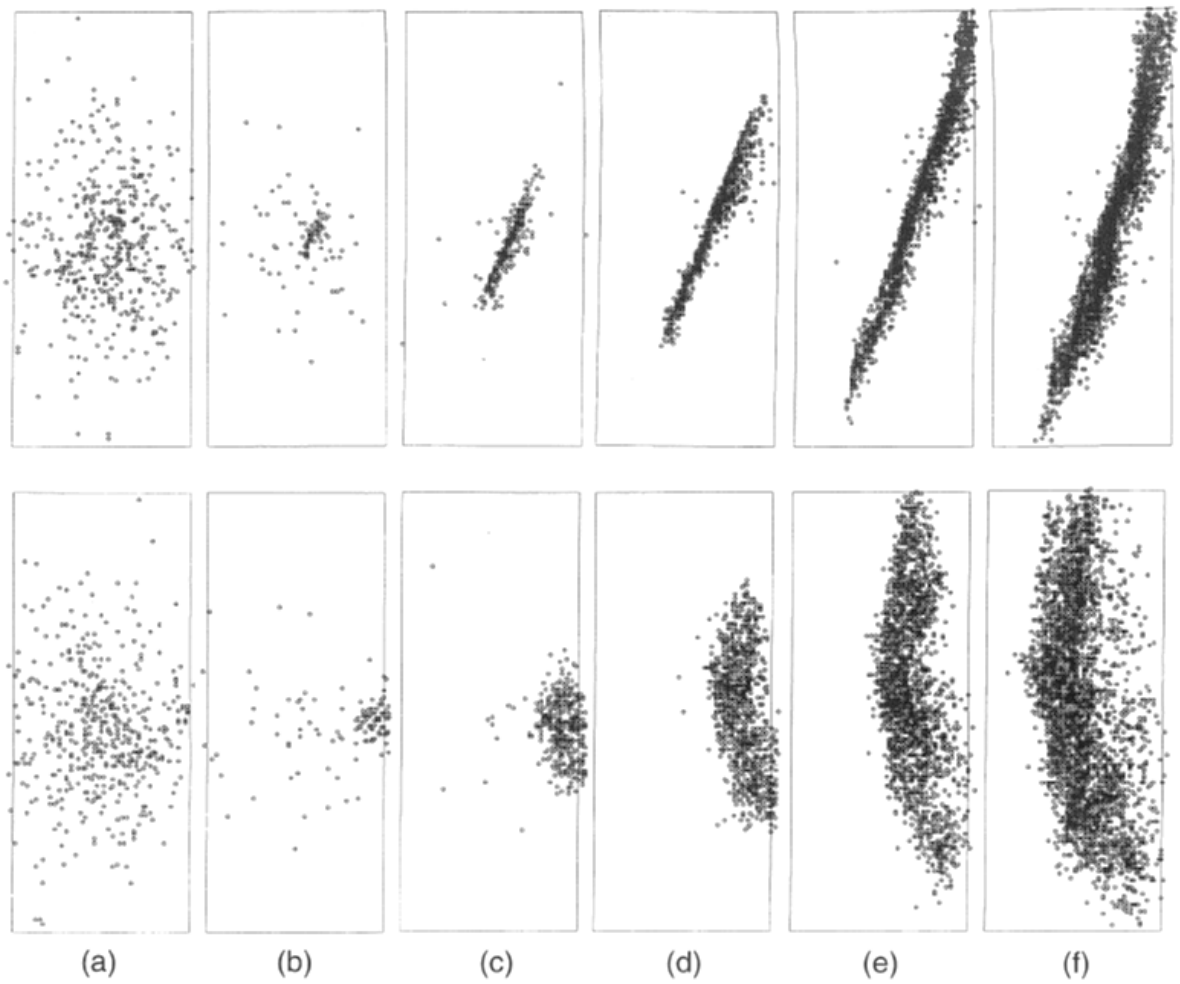

Fig. 2-15: Acoustic emissions located in the specimen during the test shown in Fig. 2-14. (LOCKNER et al., 1991)

2.5.2.3 Elastic Wave Propagation and Changes of Rock Properties

AYLING et al. (1994) analysed the microcracking during triaxial deformation of porous rocks and monitored the changes in the rock properties. It is well known that the presence of cracks reduces the elastic moduli of solids (e.g., WALSH, 1965; O'CONNELL et al., 1974) and, as a consequence, the velocity of elastic waves propagating through cracked solids. Since a cracked and porous rock sample is subjected to differential loading, changes in the moduli of the sample firstly occur as cracks and pores are closed during compaction, and then secondly, at higher stress differences, as dilatant cracks nucleate and propagate.

AYLING et al. (1994) measured changes in rock properties during deformation in order to quantitatively characterize the evolution of this precursory microcrack damage. It has been shown, however, that it is not only the number

of voids in a solid that affects the elastic-wave velocities, but also their shape and orientation. WALSH (1965) determined that the effective elastic moduli are related to a parameter that is proportional to the cube of the long dimension of the void (i.e., crack length). Consequently, for the same orientation and void volume voids with low aspect ratios (crack-like) have a much greater influence on elastic moduli (and hence on the elastic-wave velocities) than voids with high aspect ratios (pore-like). Furthermore, equidimensional pores are far more resistant to both closure and extension under an applied stress. Hence, in order to simplify the analysis, AYLING et al. (1994) assumed that the observed changes in elastic-wave velocities were primarily due to the closing and opening of cracks, and neglected any effect of non-crack-like pores.

A simple but physically realistic analogue model of crack closure and opening in triaxial stress regimes can be postulated. There is crack closure at low differential stress if the cracks are oriented perpendicularly to the maximum principal stress (σ_1) direction, ((a) shown in FIG. 2-16), and cracks are opening if they are parallel to the maximum principal stress direction at some higher differential stress (see FIG. 2-16 (b)). The normals of the axially aligned cracks can be considered to be randomly oriented with cylindrical transverse isotropy (since $\sigma_2 = \sigma_3$ in conventional triaxial tests).

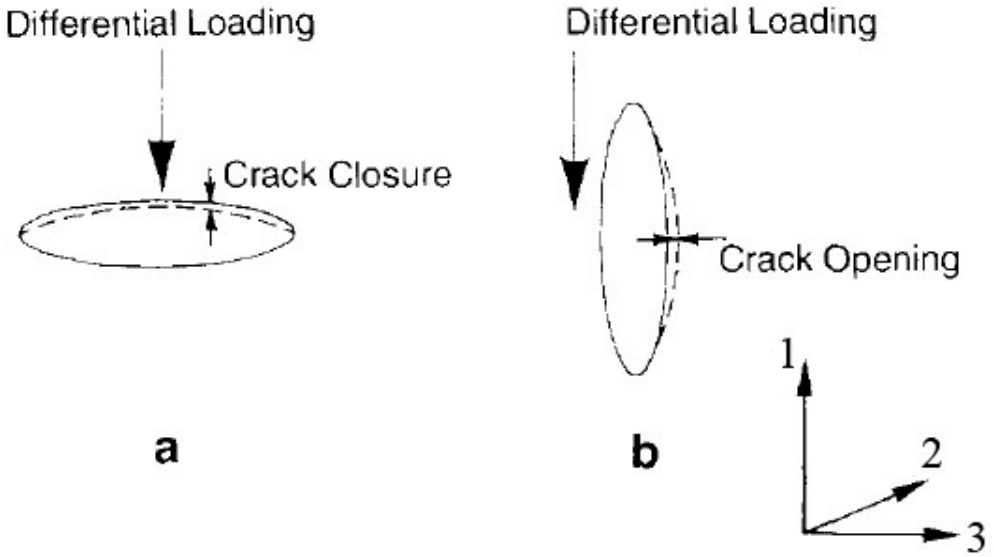

Fig. 2-16: Schematic diagram showing idealised radial crack closure (a) and axial crack opening (b) in response to increasing differential stress (AYLING et al., 1994)

Following SOGA et al. (1978), the effects of these two mechanisms can be summed, and constants substituted into the equations leading to expressions for ε_1 (the cracks density parameter for cracks lying perpendicular to the loading axis) and for $\varepsilon_2 (= \varepsilon_3)$ (the crack density parameter for the cracks lying parallel to the loading axis and therefore normal to the 2 and 3 axes). These are (see AYLING, 1991):

$$\varepsilon_3 = 4.28\left(1 - (V_S / V_{S0})^2\right) - 1.77\left(1 - (V_P / V_{P0})^2\right) \qquad (2\text{-}13)$$

$$\varepsilon_1 = 0.92\left(1 - (V_P / V_{P0})^2\right) - 0.57\left(1 - (V_S / V_{S0})^2\right) \qquad (2\text{-}14)$$

V_{P0} and V_{S0} are the P-wave velocity and the S-wave velocity through the uncracked solid respectively, and are determined at high confining pressure where all cracks are expected to be closed (JONES et al., 1989; AYLING, 1991). There are two important consequences which follow from the equations (2-13) and (2-14): (1) as radial cracks close (i.e. ε_1 decreases), V_P will increase proportionally more than V_S; and (2) as axial cracks open (and ε_3 increases), V_S will decrease proportionately more than V_P.

AYLING et al. (1994) state that initial closure of suitably oriented cracks (mainly perpendicular to the loading axis) is followed by dilatant crack growth occurring predominantly parallel to the major loading axis. Significant crack linkage appears to commence just prior to peak stress, causing a rapid reduction in both V_P and V_S. This crack linkage also reduces the load bearing capacity of the sample, leading to strain-softening. Cracks continue to coalesce, producing a smaller number of larger active cracks, and with V_P and V_S continuing to decrease during this phase but at much reduced rates. The rock sample fails catastrophically with the onset of significant angled cracking in the region of the final macroscopic fault.

In order to determine the stress changes of rock, SPIES et al. (2000) ran an experiment to analyse the behaviour of the properties of a material. They loaded a sample of rock salt in a compression test and measured the properties volume change, seismic velocity, permeability and the differential stress in dependency on time (Fig. 2-17) and registered the acoustic emission rate during the test. The

test could be divided into three stages. The first stage (I) was the stage of compaction. Existing voids in the sample were closed. The density increased and, hence, the seismic wave velocity increased (the denser a material the higher is the wave velocity). The permeability and the volume decreased. In the second stage (II), microacoustic emissions occurred. They arose from microcracks and shear strain, respectively. The permeability of the sample rapidly increased, and, therefore, the volume change slightly increased. There was a decrease of the seismic wave velocity because of the weakened structure of the material. During the loading in stage III, the length of the microcracks increased and these microcracks overlapped and joined each other. The rate of acoustic emission and the volume change increased until the sample macroscopically failed. The connecting microcracks led to shear failure.

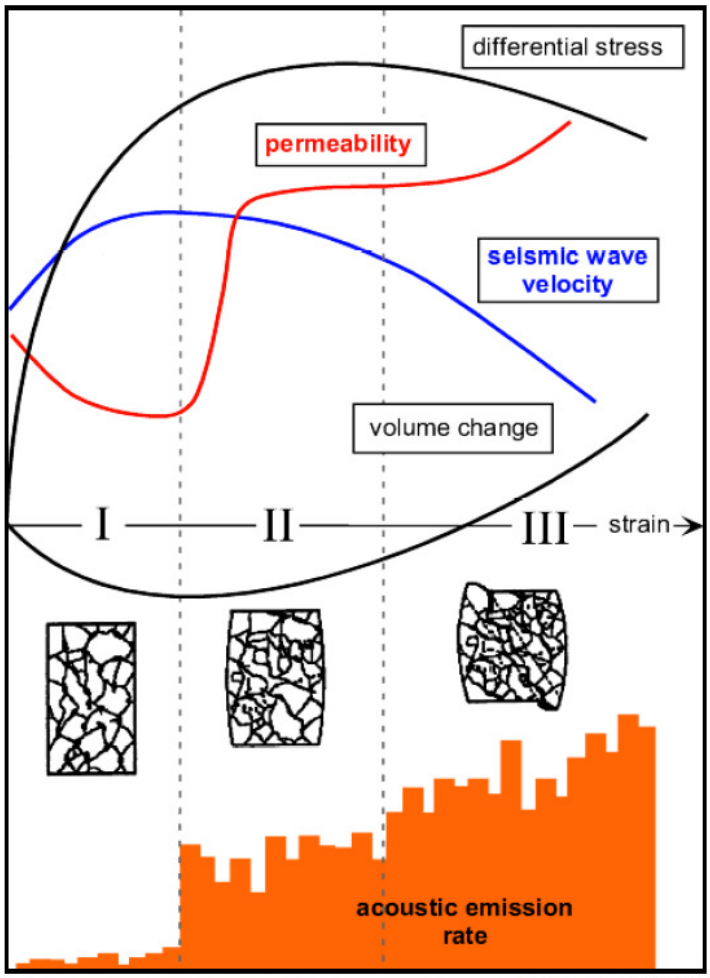

Fig. 2-17: Rock behaviour during deformation (schematic): Development of properties is used for monitoring and determination of dilatancy and permeability (SPIES et al., 2000)

The application or removal of hydrostatic pressure could theoretically cause microcracking through differential compressibility of constituent minerals. One would expect these to be mostly coincident grain boundary cracks. Acoustic emission during hydrostatic pressure cycling are usually one or two orders of magnitude less frequent than during the application of deviatoric stresses and principally occur after the first loading (TODD, 1973; SONDERGELD, 1982). These emissions, however, are most likely a result of crushing of grain boundaries and pre-existing cracks and not a result of new cracks (KRANZ, 1983).

2.5.3 Acoustic Emission Measurements in situ

Since the 1940's, rockburst research related to seismic principles has concentrated on the analysis of seismic signals below frequencies of 20 kHz. The reason for this was that equipment simply did not exist to monitor and record higher frequency ranges. Nowadays, instrumentation used in non-destructive testings can measure energy in the MHz ranges. Also, microprocessor technology has advanced to a state which allows recording and analysing of these signals at reasonable cost and with acceptable speed.

2.5.3.1 High Frequency Monitoring in Mining

In 1985, SEMADENI and CALDER carried out a research program to study high frequency microseisms in frequency ranges higher than 20 kHz. They obtained microseismic data during a series of high frequency monitoring trials at a number of hard rock mines in Ontario, Canada. A novel instrumentation was utilised to sense and record microseisms in the bandwidth of 40 kHz to 500 kHz. Piezoelectric transducers were installed in boreholes in intact rock, away from the relaxed zone which surrounds any underground opening in hard rock. The intact rock was important as microcracks in the relaxed zone preferentially attenuated high frequency components of a wave form.

SEMADENI and CALDER (1990) analysed the data from two sites under differing stress regimes and considered waveform characteristics such as event rate, amplitude distributions and frequency spectra. The lower stress site exhibited a principal stress of 13 MPa; the higher stress site was under a principal stress influence of 34 MPa. The rate of microseismic emission was highly variable and often varied for no apparent reasons. Therefore, the event rate was not used as the only criterion for predicting stress level. The frequency

spectra were analysed in terms of distributions of the center frequencies. A center frequency is defined as the frequency in the frequency spectrum which bisects the total energy. In Fig. 2-18, the two distributions of the center frequencies with the stress levels of 13 MPa (a) and 34 MPa (b) are shown. SEMADENI and CALDER (1990) found out that the microseisms produced at the high stress site generally contained higher frequency components than those produced at the low stress site. The relationship between stress level and frequency content was given for areas which had been under given stress level for some time. When they monitored areas which experienced sudden changes in stress levels the relationship was ambiguous.

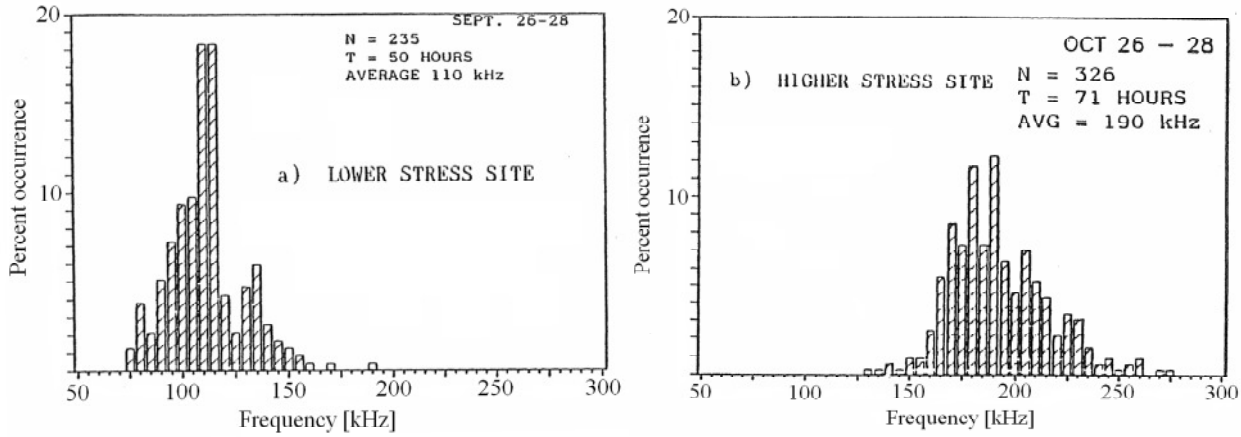

Fig. 2-18: Distributions of center frequencies with stress levels of 13 MPa (a) and 34 MPa (b) (SEMADENI and CALDER, 1990)

According to SEMADENI and CALDER (1990), the areas under higher stress levels produced events of greater amplitude. The amplitude distributions were good indicators of changing ground conditions. They concluded that spectral frequency analysis as well as amplitude distribution of microseisms were good indicators of static stress levels and the degree of failure of monitored rock masses.

2.5.3.2 Microseismic Measurements at the Gotthard Base Tunnel

The Gotthard Base Tunnel is a railway tunnel under construction in Switzerland. At the beginning of the construction, there was a series of microearthquakes that has probably been triggered by the tunnelling. Starting in 2004, ten microearthquakes with local magnitudes between 0.9 and 1.9 have been observed in the area of Faido. Prior to 2004, the same area was seismically quiet, to see in Fig. 2-19a. In the area of the blue triangles (the later additionally

installed seismic stations), no seismic activity was recorded. The seismic station Fusio (black triangle) of the 'Schweizerischer Erdbebendient' (SED) is located in the surrounding of the multifunctional station (MFS) Faido. The geology at the construction site was dominated by the fault zone between the Lucomagno and the Leventina Gneis, causing severe difficulties in the construction of the tunnel. Numerous rockbursts have been observed, some of which clearly associated spatially and in time with the occurrence of the earthquakes. To investigate whether the microearthquakes were triggered by local stress variations in the vicinity or along the fault zone caused by the tunnel construction, a dense network of additional seismometers has been installed around Faido (HUSEN et al., 2005).

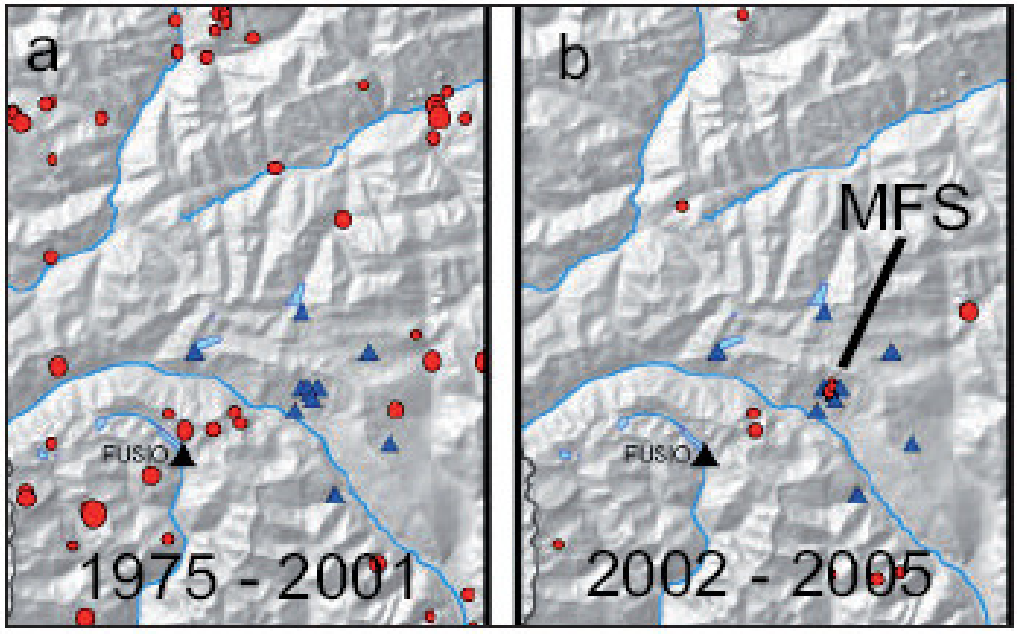

Fig. 2-19: Map of the seismic station Fusio with the registered microearthquakes (KISSLING, 2007)

Shortly after the beginning of construction of the tunnel, the seismic station Fusio registered some microearthquakes with magnitudes of 1.5 (see Fig. 2-19b, red points). To increase the localisation exactness, ten seismic stations were installed additionally. With the newly installed seismic stations, it was possible to locate the origin of the microearthquakes and the rockbursts. It was found that the microearthquakes had their origin at fracture planes, to be located in a distance of some hundred metres of the tunnel. The rockbursts, which were derived of stress accumulations, occurred in direct vicinity to the tunnel tube.

Fig. 2-20: Damage caused by a rockburst at the Gotthard Base Tunnel, Switzerland (SCHOCH, 2005)

In Fig. 2-20, an example of a damage is shown that resulted from a rockburst occurred during the tunnel excavation. On the right part of the picture, the rock broke out explosively. The reinforcement buckled through the shotcrete. Fortunately, nobody was injured.

2.5.3.3 Microseismic Monitoring in the Research Mine Asse

Another example of microseismic monitoring is the research mine Asse in Remlingen, nearby Braunschweig. In the year 1979, the storage with radioactive material was stopped. Nowadays, the mine is being closed. In 1995, they started to stabilize the mining by backfilling them with salt. To observe the procedure, a monitoring network was installed. It measured among other things the occurring acoustic emissions (AE) during and after the backfilling. The AE give information about the microcrack activity in the minings.

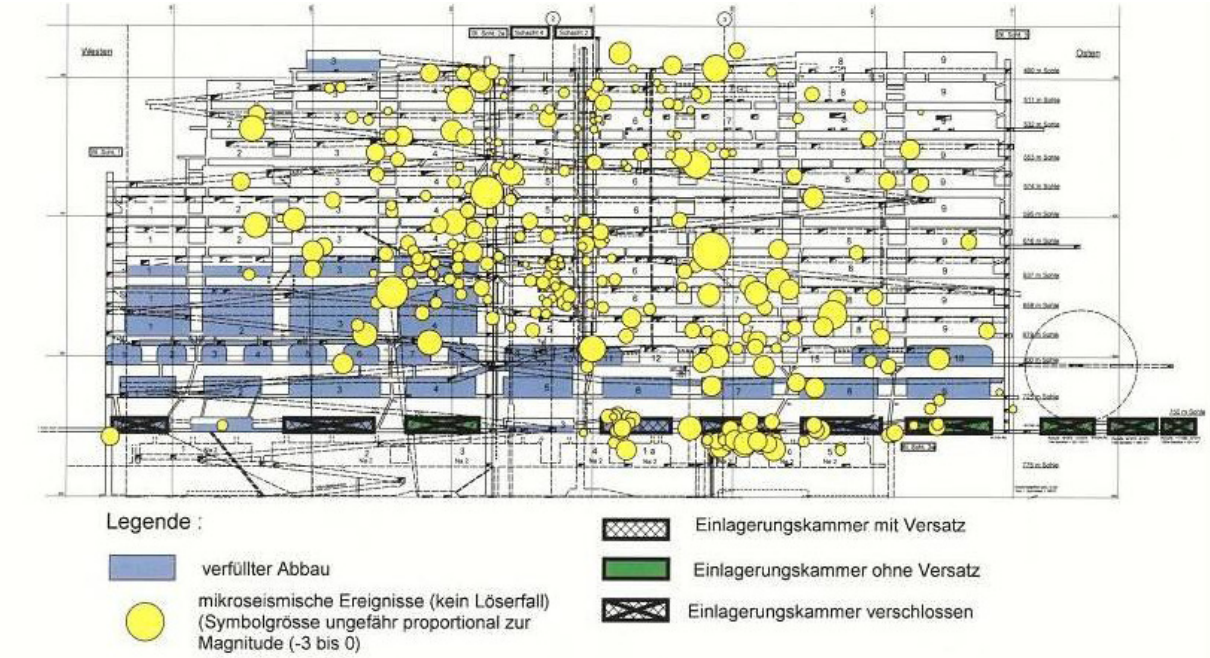

Fig. 2-21: Microseismic activity and backfilling in the year 1995 (KAPPEI, 2005)

In Fig. 2-21, the occurred acoustic emissions in the excavation chambers are shown. The lower parts of the mining are backfilled and the yellow points depict the registered AE after a first stabilizing of the mining at the bottom. It can be seen that the AE are distributed all over the mining. In the parts of the backfilled chambers, there are less acoustic emissions.

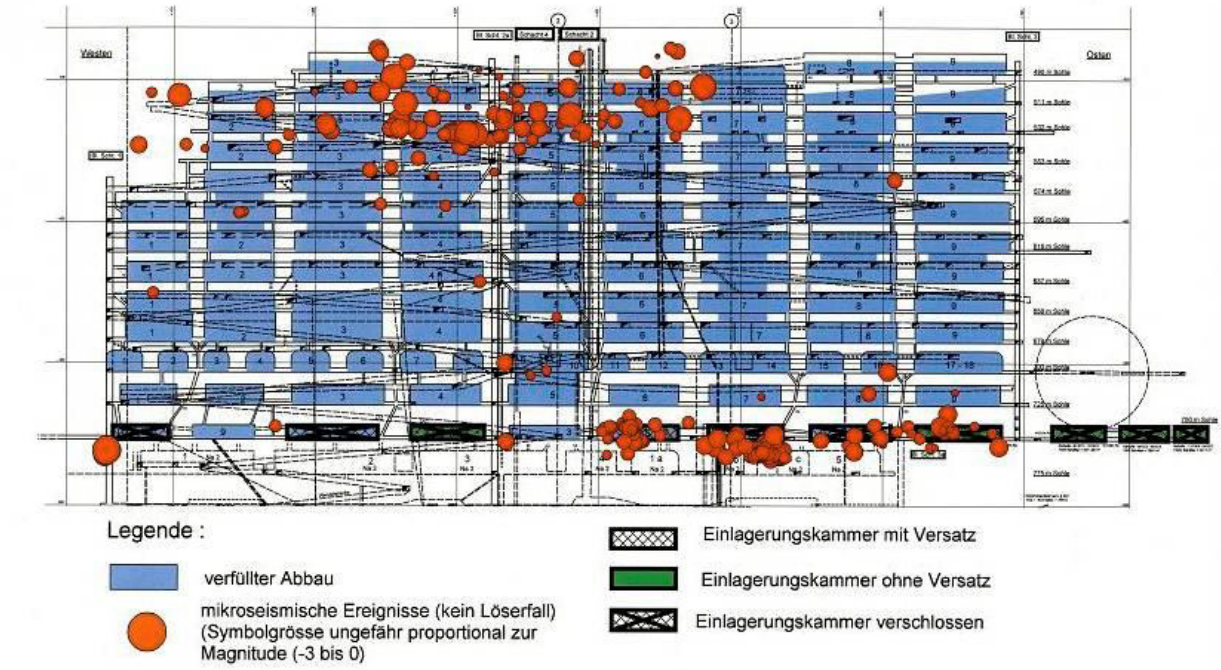

Fig. 2-22: Microseismic activity and backfilling in the year 2004 (KAPPEI, 2005)

The backfilling was done until the year 2004. Today, the excavation chambers are fully backfilled. The AE decreased and only occurred in the upper and at the very bottom parts of the chambers (see Fig. 2-22). The AE at the very bottom part are resulting from the storage of the radioactive waste. The barrels of the waste lost their concrete shields and therefore, there's a lot of friction between the barrels. This friction produces the acoustic emissions in the part of the chamber. In the other parts, the acoustic emissions are minute. There are still some acoustic emissions resulting from microcracking in the upper parts. The reason is the convergence of the backfilled salt that has creeping material properties.

2.6 Summary and Conclusions

Although rockbursts are locally linked because of man-made conditions and, nowadays, mining regions mostly are seismically monitored, there is still lack of prediction of occurring rockbursts. The fracture mechanisms inside rock are extensively examined and analysed by a large number of researchers. It is well documented, e.g., that brittle fracture, which is characterized by a sudden material failure without the occurrence of significant previous plastic deformations, involves the growth of microcracks from stress concentrations such as voids, inclusions and dissimilar grain contacts that result in contrast of elastic properties. This irreversible damage results in both inelastic strain and acoustic emissions. These acoustic emissions give information about the fracture processes inside the rock and by recording them, an investigation can follow. Up to now, acoustic emissions are used to locate the source of the fracture process. Furthermore, an accumulation of AE indicates greater fracture processes.

The present research work attends to investigate the frequency behaviour of recorded acoustic emissions by a laboratory test. The frequency components of an event can be correlated to the energy content of the fracture process at the source. Hence, the aim of the investigations undertaken within this work is to examine the frequency components recorded during a uniaxial compression test and to reveal the frequencies at different phases of load application. The test series represent the first investigations of their kind and are regarded as first steps towards the ambitious aim to predict macroscopic failure.

3 Measurement Chain of the Laboratory Test

In the laboratory test, a specimen of calcareous sandstone is subject to a uniaxial compression test. The occurring acoustic emission events were recorded by two acceleration sensors. The signals were amplified tenfold by the voltage amplifier to allow greater accuracy and resolution, and stored with a data acquisition instrument.

3.1 Loading System

To supply a load on the sample, a uniaxial compression test was performed. The specimen was centrically placed between the loading platens of the press. The maximum press load capacity is given by 100 kN. Since the sample had to be loaded until it broke, the maximum sample size was 7.1 x 7.1 x 11.5 cm³. In Fig. 3-2, the sample and the installation in the press are depicted. The tests were carried out with a path-controlled velocity. The specimen was compressed until its failure.

3.2 Material

The material used for the test series was calcareous sandstone. The material was chosen because it is an artificially produced material and, therefore, the reproducibility of the results is given. The material properties of the sandstone are almost homogenous and brittle. A homogenous material is a material which has the same material parameters in any direction and any point. A brittle material is specified by linear elastic stress-strain behaviour with only little plastic deformation.

In Fig. 3-1, a sample of calcareous sandstone is depicted with the dimensions chosen for the test set-up. The material properties of calcareous sandstone are quite similar to the ones of natural rock and are shown in Table 3-1. The values

for the calcareous sandstone are given by the manufacturer, and the values of natural sandstone, rock (stiff, stable) and rock (soft, unstable) are found in SCHMITT ET AL. (2006).

Table 3-1: Material properties of different materials

	Density	**E-modulus**	**Poisson's ratio**
	[kN/m³]	[MN/m²]	[-]
Calcareous sandstone [1)]	20.0	5,000	0.2
Natural sandstone [2)]	25.0	10,000	0.2
Rock (stiff, stable) [2)]	26.0	10,000	0.2
Rock (soft, unstable) [2)]	26.0	4,000	0.2

1) Manufacturer's information, 2) SCHMITT et al. (2006)

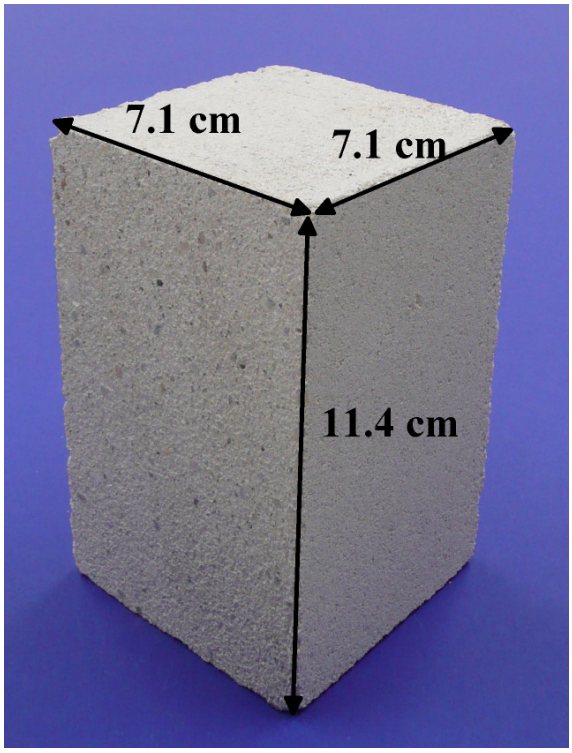

Fig. 3-1: Sample of calcareous sandstone

3.3 Measurement Chain

First tests were carried out with the PTB (Physikalisch-Technische Bundesanstalt) in Braunschweig. The PTB has a high wealth of experiences in building acoustics; hence the PTB put the measurement equipment at the institute's disposal for the first test series. Owing to the first results done with the PTB, a measurement chain was developed within the present research work to continue and deepen the tests. The test set-up and its parameters were modified and improved with regard to the behaviour of prefailure during the test.

To register the microacoustic emissions during the compression test, the acceleration sensors were applied to the sandstone. The sensors were fixed laterally by fast solidifying putty with small adapter plates (see Fig. 3-2). The measuring sensors registered the accelerations at the fix points and an external displacement transducer measured the strain of the sample during the test. Afterwards, the signals were amplified by a low-noise voltage amplifier. A data logger recorded the acceleration with a USB-supported system; it achieved a speed of 1 MHz at a 16-bit resolution. The components of the measurement chain are shown in Fig. 3-2.

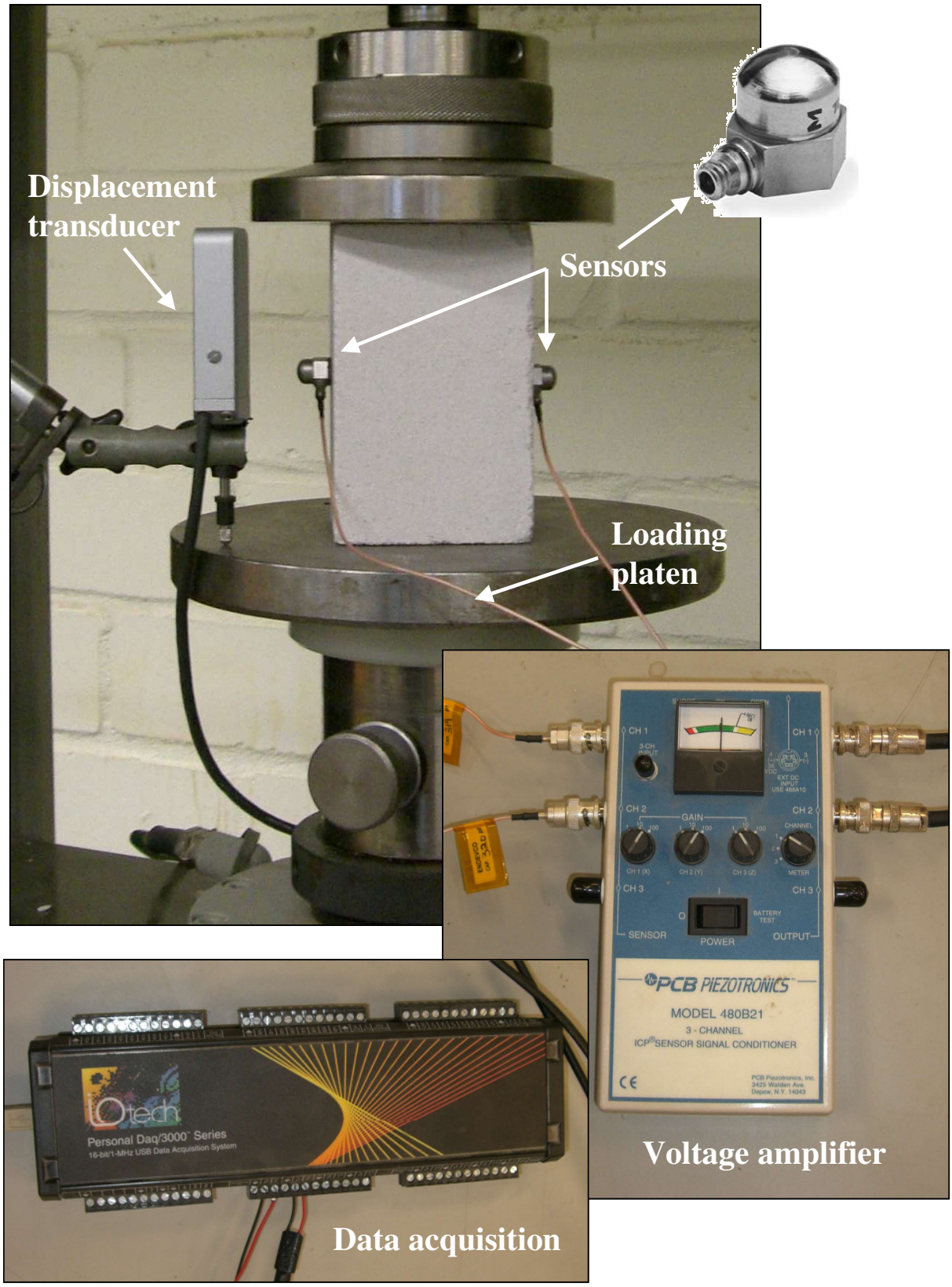

Fig. 3-2: Components of the measurement chain

3.3.1 Acceleration Sensor

An acceleration sensor converts elastic waves into electrical signals. The electric output signal depends on the sensitivity, directivity, and frequency response of the sensor. An ideal AE sensor should be able to measure over the full frequency bandwidth of the signals. The majority of sensors used in AE measurements are made of piezoelectric materials such as PZT ceramic. This kind of sensor is resonant and therefore very sensitive at its resonant frequency.

In the measurements carried out for this research, the sensor (type Endevco® 7259B-100, see Fig. 3-2) was a piezoelectric accelerometer with integral electronics. It used a piezoelectric crystal element which exhibited low base strain sensitivity, wide bandwidth, and good output stability over time. The sensor design allowed for high seismic resonance and ruggedness.

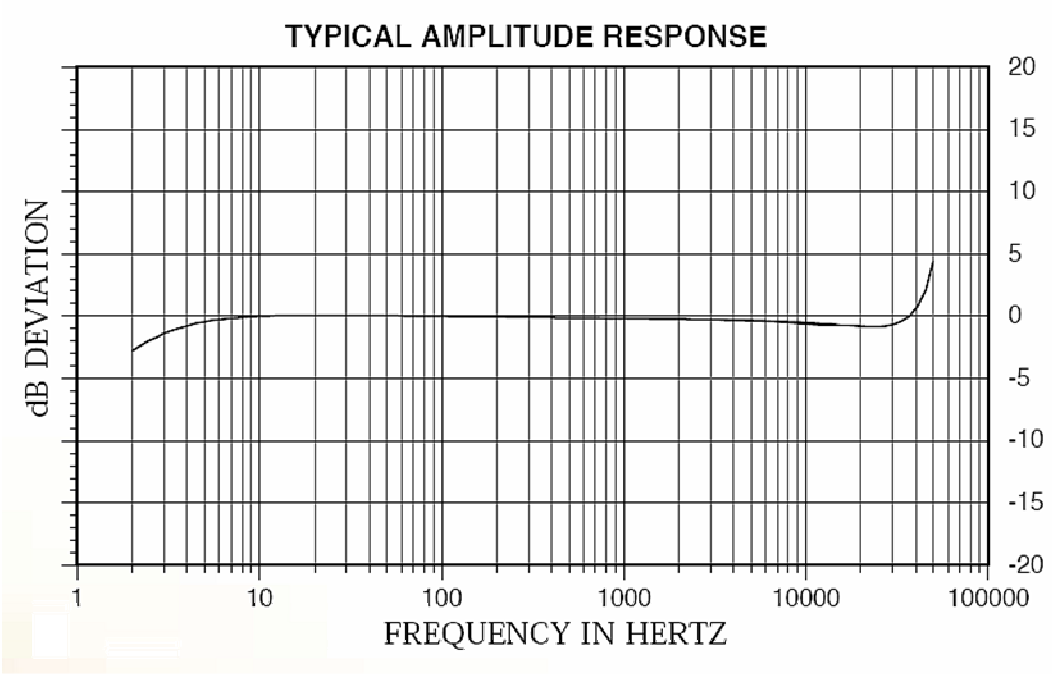

Fig. 3-3: Calibration curve of acceleration sensor (DATASHEET ENDEVCO)

In Fig. 3-3, a typical calibration curve of this type of sensors is shown. The calibration curve begins at a frequency of 2 Hz and ends at the corner frequency of 50 kHz. The resonance frequency of the sensors is given at 90 kHz. The two sensors used for this research had output sensitivities of 103.5 mV/g and 98.13 mV/g. The sensors were connected differentially to the data acquisition system to reduce signal errors and the induction of noise resulting from ground current. A low-noise coaxial cable was supplied for error-free operation.

3.3.2 Voltage Amplifier

The used voltage amplifier is a 3-channel ICP® battery power signal conditioner, as depicted in Fig. 3-2. The voltage gain switches offer amplification factors of 1, 10 and 100. The model 480B21 of PCB Piezotronics operates from three self-contained 9-volt transistor radio batteries and supply constant-current power to the built-in sensor amplifier in ICP® sensors. The unit, being battery operated, is especially noise-free and unaffected by ground loops. A notable feature is the unit's low-frequency response. The current output is fixed at 3 mA. This current will adequately handle high-frequency signals in cables up to approximately 100 ft long. Longer cables can be driven, but with sacrifice of high-frequency response.

3.3.3 External Displacement Transducer

Since the displacement transducer of the press measured the entire deformation of the press, an external displacement transducer had to be implemented in order to measure the deformation of the sample. The external displacement transducer is shown in Fig. 3-2.

3.3.4 Data Acquisition Instrument and DaqView

All experimental data were acquired by a data acquisition instrument, called Iotech® PersonalDaq3005. It was a 16-bit/1-MHz A/D-converter and was connected by a USB port to the host PC. An analog-to-digital converter (A/D-converter) converted an analog voltage to a digital number. The module included a high-speed, low-latency, highly deterministic control output mode that operated independently of the PC. The data acquisition instrument is depicted in Fig. 3-2, too.

The software program DaqView included in the PersonalDaq3005 and distributed by Iotech® was used for the settings of the data acquisition system. For example, the sampling frequency, the differential mode of connecting and the range of voltage were set in the software. The recording of the data was started and stopped manually.

The recorded data was transferred to MATLAB® for the data analysis. Further details of the analysis are given in Chapter '4 Data acquisition and data processing'.

3.4 Verification of Measurement Chain

To verify the output data of the measurement chain, it was necessary to comprehend the data processing. Thus, a defined frequency of 159.2 Hz was applied by a calibration exciter to the acceleration sensor. Three different modes of gain (no gain, tenfold, hundredfold) were set at the voltage amplifier; and the data acquisition instrument recorded the values in voltage [V].

At the top of Fig. 3-4, the graph shows the measured voltage over time which resulted from the applied frequency of 159.2 Hz having set the ‘no gain’ mode. The data was not gained and the voltage is in a range of ± 0.14 V. The middle diagram depicts the same input signal but converted into the function of acceleration in [m/s²].

The graph at the bottom of Fig. 3-4 depicts the spectrum of frequency determined by the Fast-Fourier-Transformation (FFT) which is explained in the following Chapter ‘Data acquisition and data processing’. The main frequency of the spectrum is given by 160.8 Hz which is almost the defined and applied frequency of the calibration exciter.

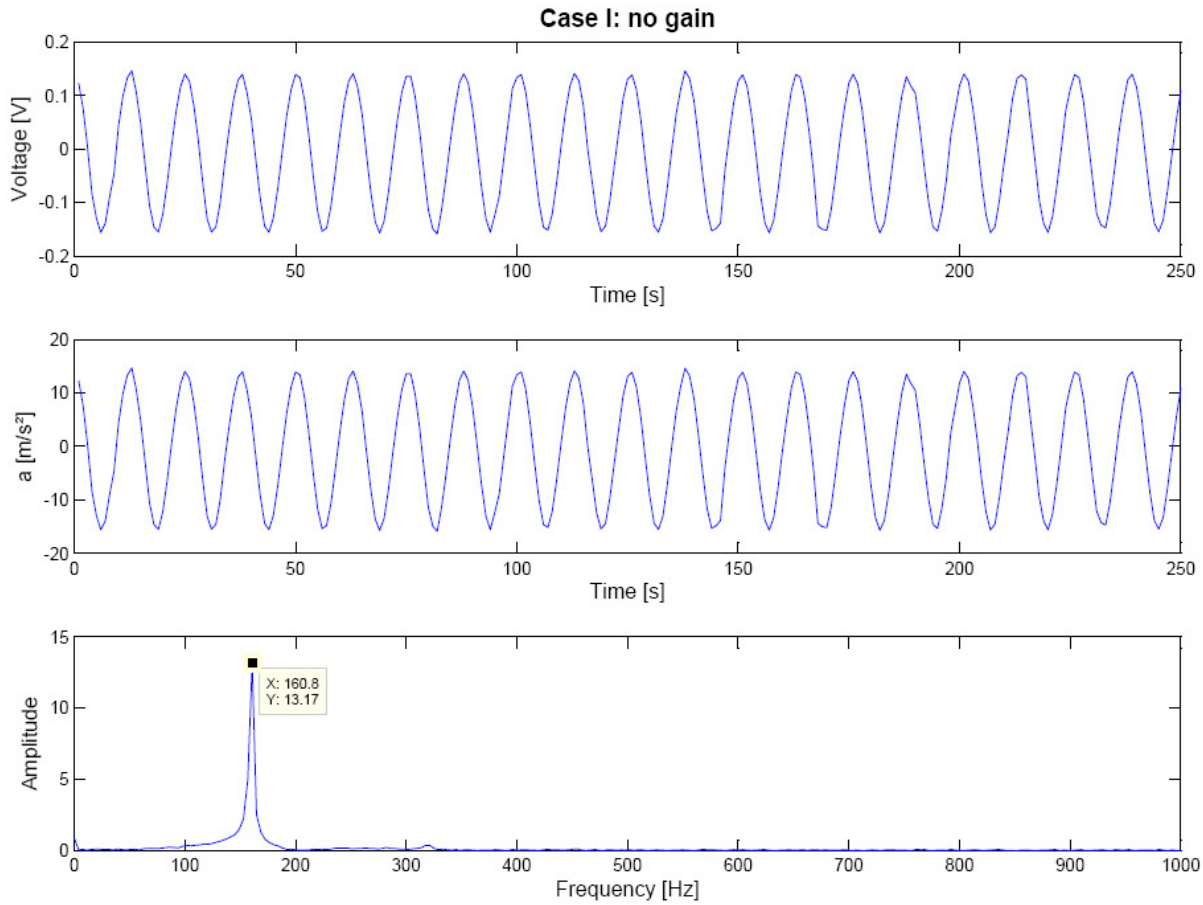

Fig. 3-4: Case I: Data with no gain and spectrum of frequency

In Fig. 3-5, the second case of signal amplification is shown. Therefore, the input signal was tenfold gained by the voltage amplifier. The data acquisition instrument recorded the data in voltage again. The difference to the first case is shown in the range of the measured voltage which is depicted at the top of Fig. 3-5. The range of the voltage is ± 1.4 V and, hence, ten times higher than in the first case. After converting the signal, the recorded signal is depicted as a function of acceleration, in the middle diagram of Fig. 3-5. The values of the acceleration are equal to those of case I and range between ± 14 m/s². The evaluation of the frequency spectrum also shows a significant frequency of 160.8 Hz which almost corresponds to the applied frequency of the calibration exciter of 159.2 Hz.

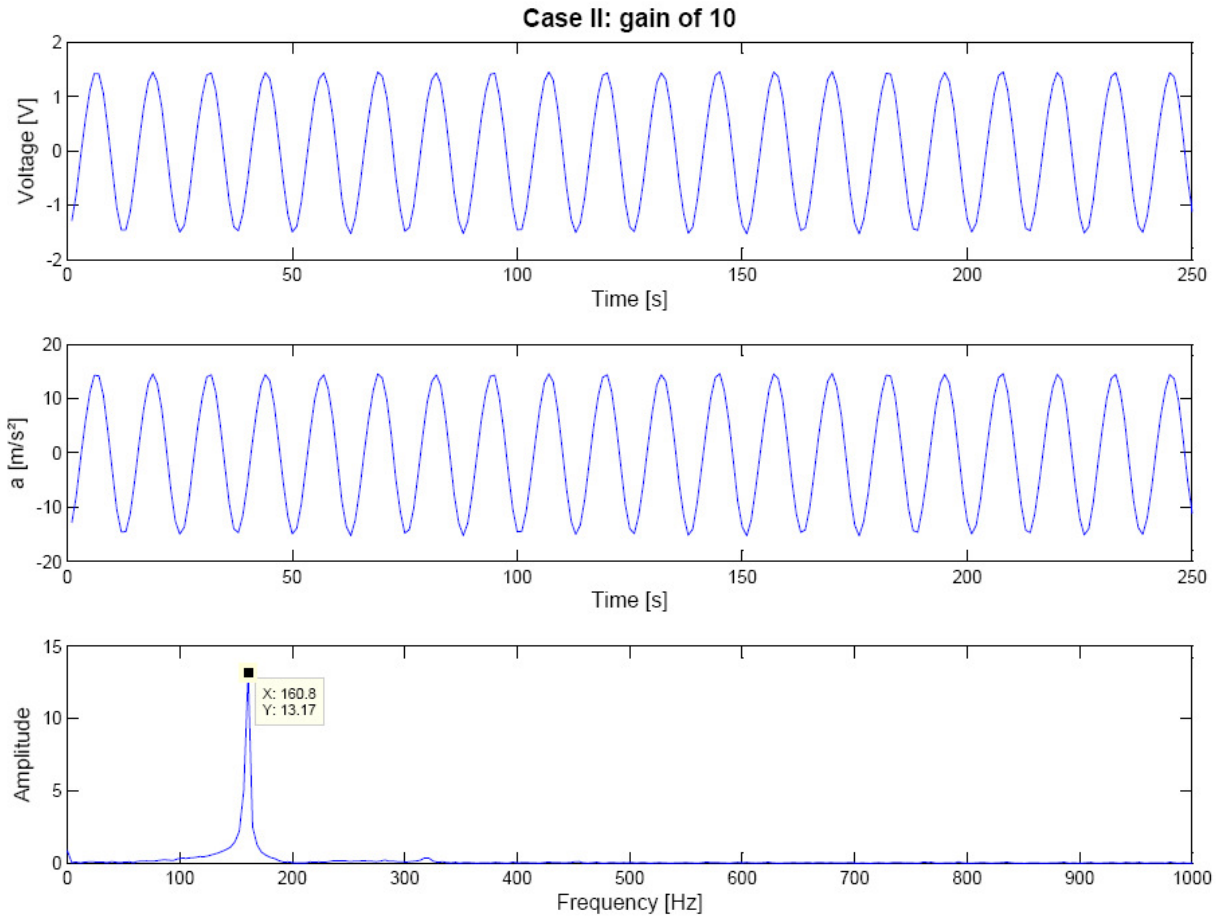

Fig. 3-5: Case II: Data with a gain of '10' and spectrum of frequency

The amplification of the input signal with a factor of '100' revealed corresponding results. The range of the voltage increased to ± 14 V depending on the higher factor of gain. The values of the acceleration stayed the same (± 14 m/s²). The spectrum of frequency also gave a significant frequency of 160.8 Hz.

Hence, the measurement chain consisting of all components is checked and operative for the laboratory test set-up.

4 Data Acquisition and Data Processing

4.1 Data Acquisition

During the test set-up, an analog input signal is recorded. The acceleration sensor converts the nonelectrical signal to the analog electrical signal (voltage). This analog signal is sampled at a rate high enough to attenuate aliasing distortion. The signal is then converted via the analog-to-digital conversion unit into the digital signal, which is discrete both in time and amplitude. The digital signal is fed to a digital filter, which is applied to limit the frequency range of digital signals. The purpose of filtering is to remove frequency components outside the frequency range of the sensor. The data acquisition system then accepts the band-limited signal at the output of the digital filter and is than ready to work with.

Sampling is the conversion of a continuous-time signal into a discrete-time signal obtained by taking samples of the continuous-time signal at discrete-time instants. If an analog signal is not appropriately sampled, aliasing will occur, which causes unwanted signals in the desired frequency band. The sampling theorem requires that the sampling rate be twice as large as the highest frequency of the analog signal to be sampled. It ensures the complete reconstruction of the analog signal without aliasing distortion. Aliasing concerns the effect of sampling a continuous function that is not bandwidth-limited to less than the Nyquist critical frequency. Any frequency component outside of the frequency range is aliased into the range by the very act of discrete sampling.

In time domain, representation of digital signals describes the signal amplitude versus the sampling time instant or the sample number. However, in some applications, signal frequency content is very useful otherwise than as digital signal samples. The representation of the digital signal in terms of its frequency

component in a frequency domain, that is, the signal spectrum, is quite useful. The algorithm transforming the time domain signal samples to the frequency domain components is known as the Fast Fourier Transform, or FFT. The FFT also establishes a relationship between the time domain representation and the frequency domain representation. Therefore, the FFT is used to perform frequency analysis of a time domain sequence.

4.1.1 Theory of Fast Fourier Transform

Microseismic data can be described either in the time domain, by the values of some quantity h as a function of time t, e.g., $h(t)$, or else in the frequency domain, where the process is specified by giving its amplitude H as a function of frequency f, that is $H(f)$, with $-\infty < f < \infty$. For many purposes, it is useful to think of $h(t)$ and $H(f)$ as being two different representations of the same function. One goes back and forth between these two representations by means of the Fourier transform equations,

$$H(f) = \int_{-\infty}^{\infty} h(t) e^{2\pi i f t} dt$$
$$h(t) = \int_{-\infty}^{\infty} H(f) e^{-2\pi i f t} df. \qquad (4\text{-}1)$$

If t is measured in seconds, then f in equation (4-1) is in cycles per second, or Hertz. If h is a function of position x (in meters), H will be a function of inverse wavelength (cycles per meter).

In computational work, especially with experimental data, there is almost never given a continuous function $h(t)$ to work with, but is given, rather, a list of measurements of $h(t_i)$ for a discrete set of t_i's. The profound implications of this seemingly unimportant fact are the subject of the next subchapter.

4.1.2 Theory of Sampling Theorem and Aliasing

In the most common situations, function $h(t)$ is sampled at evenly spaced intervals in time. Let Δ denote the time interval between consecutive samples, so that the sequence of sampled values is

$$h_n = h(n\Delta) \qquad n = ..., 3, -2, -1, 0, 1, 2, 3, ... \qquad (4\text{-}2)$$

The reciprocal of the time interval Δ is called the sampling rate; if Δ is measured in seconds, for example, then the sampling rate is the number of samples recorded per second.

For any sampling interval Δ, there is also a special frequency f_c, called the Nyquist critical frequency, given by

$$f_c \equiv \frac{1}{2\Delta}. \qquad (4\text{-}3)$$

If a sine wave of the Nyquist critical frequency is sampled at its positive peak value, then the next sample will be at its negative trough value, the sample after that at the positive peak again, and so on. Expressed otherwise: Critical sampling of a sine wave is two sample points per cycle. One frequently chooses to measure time in units of the sampling interval Δ. In this case, the Nyquist critical frequency is just constant 1/2.

The Nyquist critical frequency is important for two related, but distinct, reasons. The first reason is the fact known as the sampling theorem: If a continuous function $h(t)$, sampled at an interval Δ, happens to be bandwidth-limited to frequencies smaller in magnitude than f_c, i.e., if $H(f) = 0$ for all $|f| \geq f_c$, then the function $h(t)$ is completely determined by its samples h_n. In fact, $h(t)$ is given explicitly by the formula

$$h(t) = \Delta \sum_{n=-\infty}^{+\infty} h_n \frac{\sin[2\pi f_c(t - n\Delta)]}{\pi(t - n\Delta)}. \qquad (4\text{-}4)$$

This is an important theorem for many reasons; among them that it shows that the ‘information content’ of a bandwidth-limited function is, in some sense, infinitely smaller than that of a general continuous function. Often, one is dealing with a signal that is known on physical grounds to be bandwidth-limited (or at least approximately bandwidth-limited). For example, the signal may have

passed through an amplifier with a known, finite frequency response. In this case, the sampling theorem tells us that the entire information content of the signal can be recorded by sampling it a rate Δ^{-1} equal to twice the maximum frequency passed by the amplifier (see equation (4-3)).

Another important reason of the Nyquist critical frequency concerns the effect of sampling a continuous function that is not bandwidth-limited to less than the Nyquist critical frequency. In that case, it turns out that all of the power spectral density that lies outside of the frequency range $-f_c < f < f_c$ is spuriously moved into the range. This phenomenon is called aliasing. Any frequency component outside of the frequency range $(-f_c,\ f_c)$ is aliased into the range by the very act of discrete sampling. Little can be done to remove aliased power once the signal is discretely sampled. The way to overcome aliasing is to (i) know the natural bandwidth of a signal – or else enforce a known limit by analog filtering of a continuous signal, and then (ii) sample at a rate sufficiently rapid to give at least two points per cycle of the highest frequency present. Fig. 4-1 illustrates these considerations.

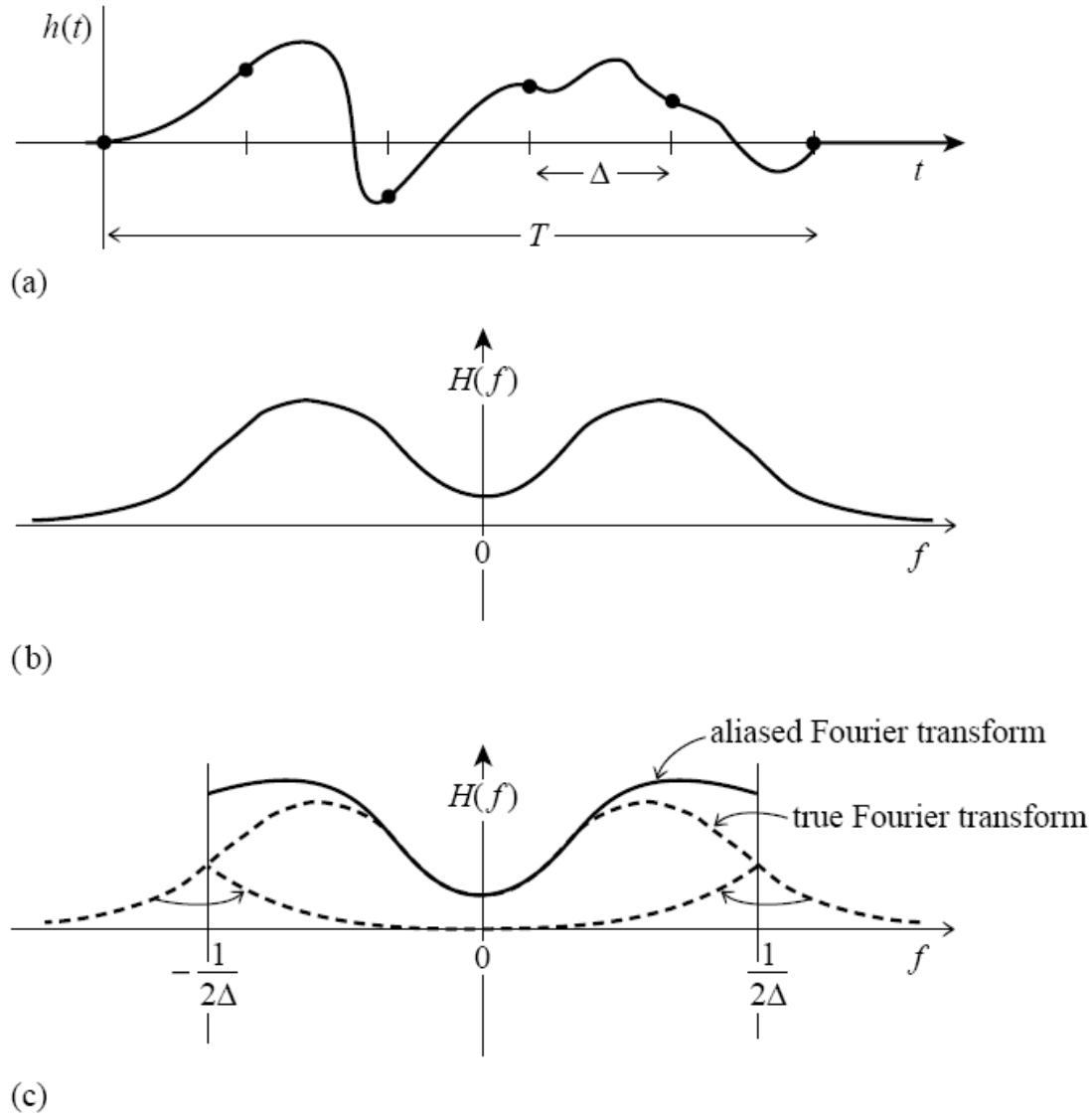

Fig. 4-1: Effect of aliasing (PRESS et al., 1992)

The continuous function shown in Fig. 4-1 (a) is nonzero only for a finite interval of time T. It follows that its Fourier transform, whose modulus is shown schematically in (b), is not bandwidth-limited but has finite amplitude for all frequencies. If the original function is sampled with a sampling interval Δ, as in (a), then the Fourier transform (c) is defined only between plus and minus the Nyquist critical frequency. Power outside that range is folded over or 'aliased' into the range.

If a continuous function has been competently sampled (aliasing effects minimized), then the Fourier transform is equal to zero outside of the frequency range in between $-f_c$ and f_c. If, on the contrary, the transform is going towards

some finite value, then chances are that components outside of the range have been folded back over onto the critical range.

It has to be ensured that samples are collected at a rate high enough that the original analog signal can be reconstructed or recovered later. In other words, it is necessary to look for the minimum sampling rate to acquire a complete reconstruction of the analog signal from its sampled version.

4.1.3 Theory of Bandpass Filter

In general, a filter is designed based on specifications primarily for the passband, stopband, and transition band of the filter frequency response. The filter passband is the frequency range with the amplitude gain of the filter response being approximately unity. The filter stopband is defined as the frequency range over which the filter magnitude response is attenuated to eliminate the input signal whose frequency components are within that range. The transition band denotes the frequency range between the passband and the stopband. The design specifications of the bandpass filter are illustrated in Fig. 4-2. The bandpass filter attenuates both low- and high-frequency components while remaining the middle-frequency component.

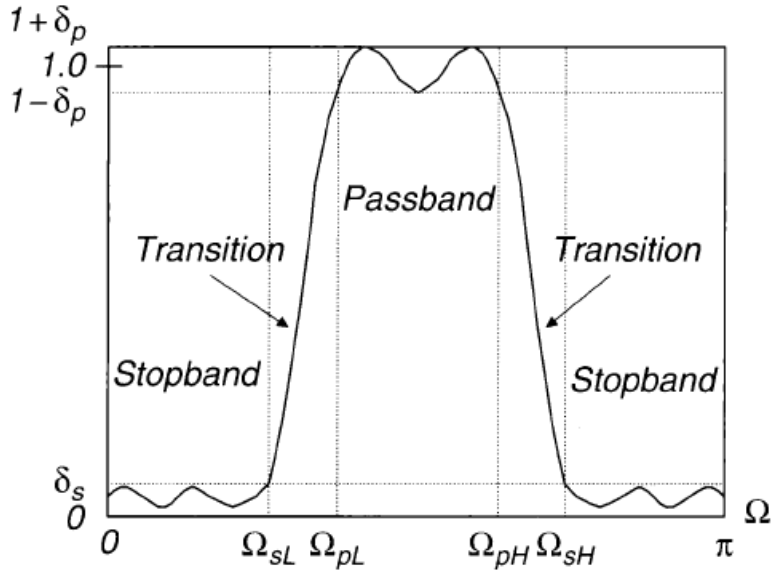

Fig. 4-2: Magnitude response of the normalized bandpass filter (TAN, 2007)

As illustrated in Fig. 4-2, Ω_{pL} and Ω_{sL} are the lower passband cutoff frequency and the lower stopband cutoff frequency, respectively. Ω_{pH} and Ω_{sH} are the

upper passband cutoff frequency and the upper stopband cutoff frequency, respectively. δ_p is the design parameter to specify the ripple of the frequency response in the passband, while δ_s specifies the ripple of the frequency response in the stopbands.

4.2 Application to Laboratory Test

4.2.1 Conversion of Measured Values in Accelerations

The measurement chain described extensively in the previous chapter recorded the values of the test as a signal in *volt*. To get accelerations for the following procedures, the measured signal had to be converted in a signal of unit *m/s²* in dependency on the factor of gain and the factor of the sensor's sensitivity. That is

$$acceleration\ [m/s^2] = \frac{measured\ value\ [V] - mean\ value\ [V]}{calibration\ \ factor\left[V/_{m/s^2}\right] \cdot gain\ \ factor}. \qquad (4\text{-}5)$$

Equation (4-5) describes the conversion of the signal of the measured values in a signal of accelerations. The factors of calibration are given in chapter '03' and were determined specifically for each sensor. The factor of gain resulted from the settings of the voltage amplifier. Furthermore, the mean value of the acceleration signal was determined and was subtracted from each measured data point to reduce the offset. The signal then oscillated on its zero line. After this conversion, the signal describes the accelerations during the laboratory test.

4.2.2 Sampling Frequency of the Laboratory Test

Because of the lack of knowledge about occurring frequencies in rock, especially in calcareous sandstone, an oversampling of the analog signal is useful to improve resolution of analog-to-digital conversion. Oversampling uses a sampling rate, which is much higher than the maximum frequency of the sensor. The benefit from an oversampling includes helping to design a simple analog aliasing filter before analog-to-digital conversion.

The maximum sampling frequency which can be set at the data acquisition system using two sensors is 500 kHz. To exclude the effect of aliasing, first tests were performed with a sampling frequency of 500 kHz. The accelerations were measured continuously and single events were cut out of the signal to analyse them with the FFT algorithm.

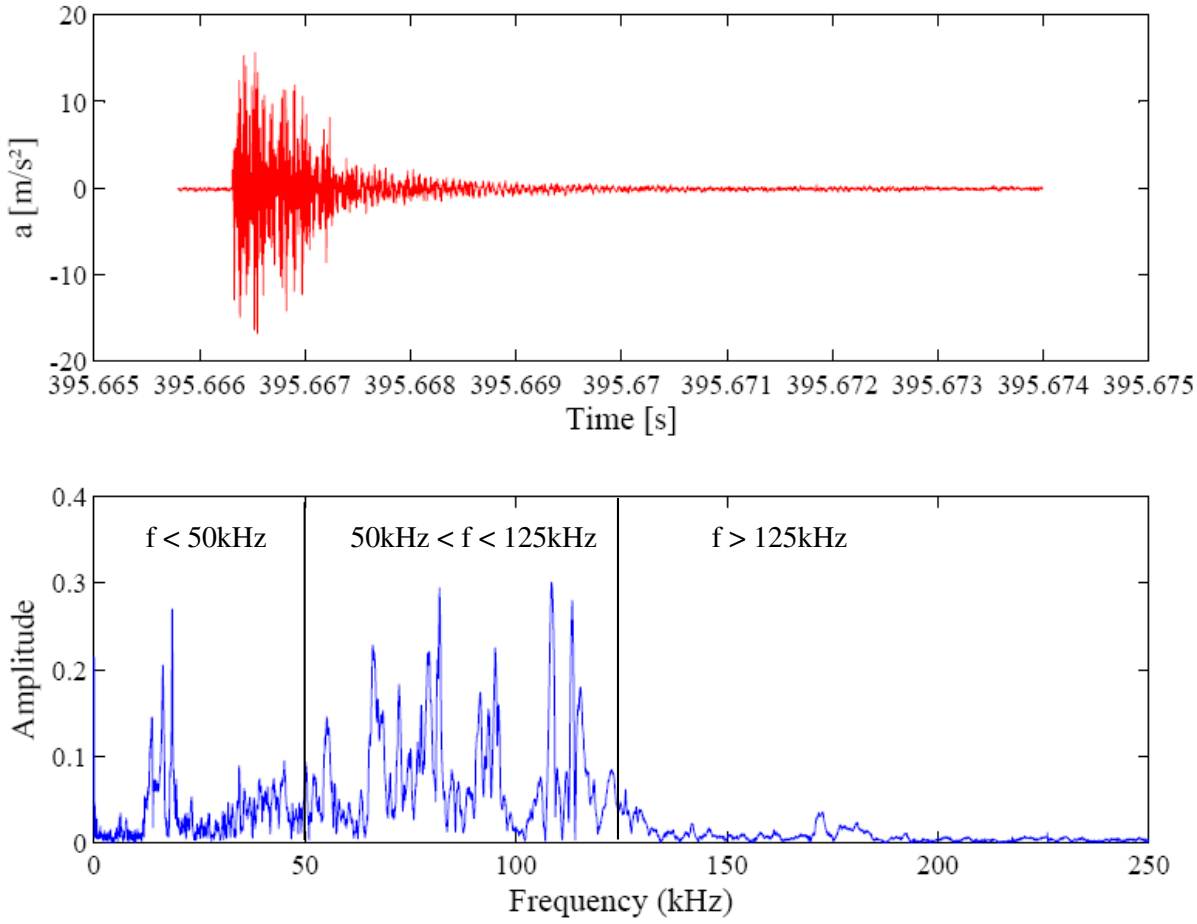

Fig. 4-3: Acceleration signal (top) and frequency spectrum (bottom)

At the top plot of Fig. 4-3, a single event which is cut out of the continuous signal is depicted as an acceleration-time signal. The cut out signal consists of 4,096 sampling points resulting from a sampling frequency of 500 kHz and a time duration of 4.096 ms. The calculated signal spectrum (frequency content), defined as the signal amplitude versus its corresponding frequency, is shown at the bottom plot of Fig. 4-3. Hence, the frequency content display presents clear frequency information of the recorded acceleration signal. It can be observed that there are spectral peaks in the range between 0 and 125 kHz. The Fourier transform is almost zero from frequencies higher than 125 kHz. The transform is not going towards some finite value; thus, components outside of the range have

not been folded back over onto the critical range. In order to neglect the aliasing effect in the further tests, the sampling rate is chosen double the Nyquist frequency, namely 250 kHz. With this sampling rate, the signal is sampled competently.

4.2.3 Bandpass Filter of the Laboratory Test

Regarding the bottom plot at Fig. 4-3, there are still bursts in the signal that have higher frequencies than 50 kHz which is the corner frequency of the acceleration sensor and, therefore, the maximal frequency which is calibrated. To exclude the frequencies above the corner frequency, a digital bandpass filter was taken. According to the frequency range of the sensors, a bandpass filter attenuates both low- and high-frequency components while remaining the middle-frequency component of the digital sampled signal. The frequency range is given by 2 Hz to 50 kHz.

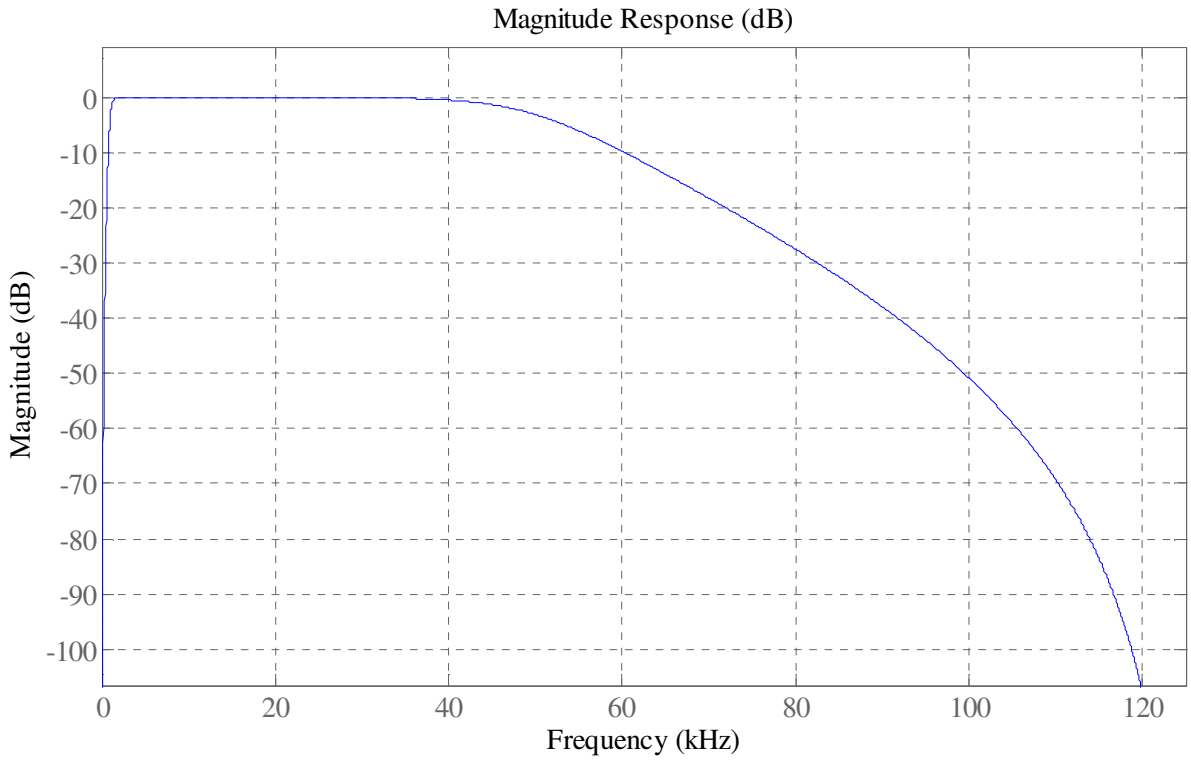

Fig. 4-4: Magnitude Response of the bandpass filter

In Fig. 4-4, the magnitude response of the designed bandpass filter is depicted. The designed filter is an 8^{th}-order Butterworth filter which is characterized by a magnitude response that is maximally flat in the passband and monotonic overall. Butterworth filters sacrifice rolloff steepness for monotonicity in the

pass- and stopbands. The filter has an order of '8' which describes the steepness of the damping. The upper passband cutoff frequency Ω_{pH} was set to 50 kHz and is that frequency where the magnitude response of the filter is $\sqrt{1/2}$.

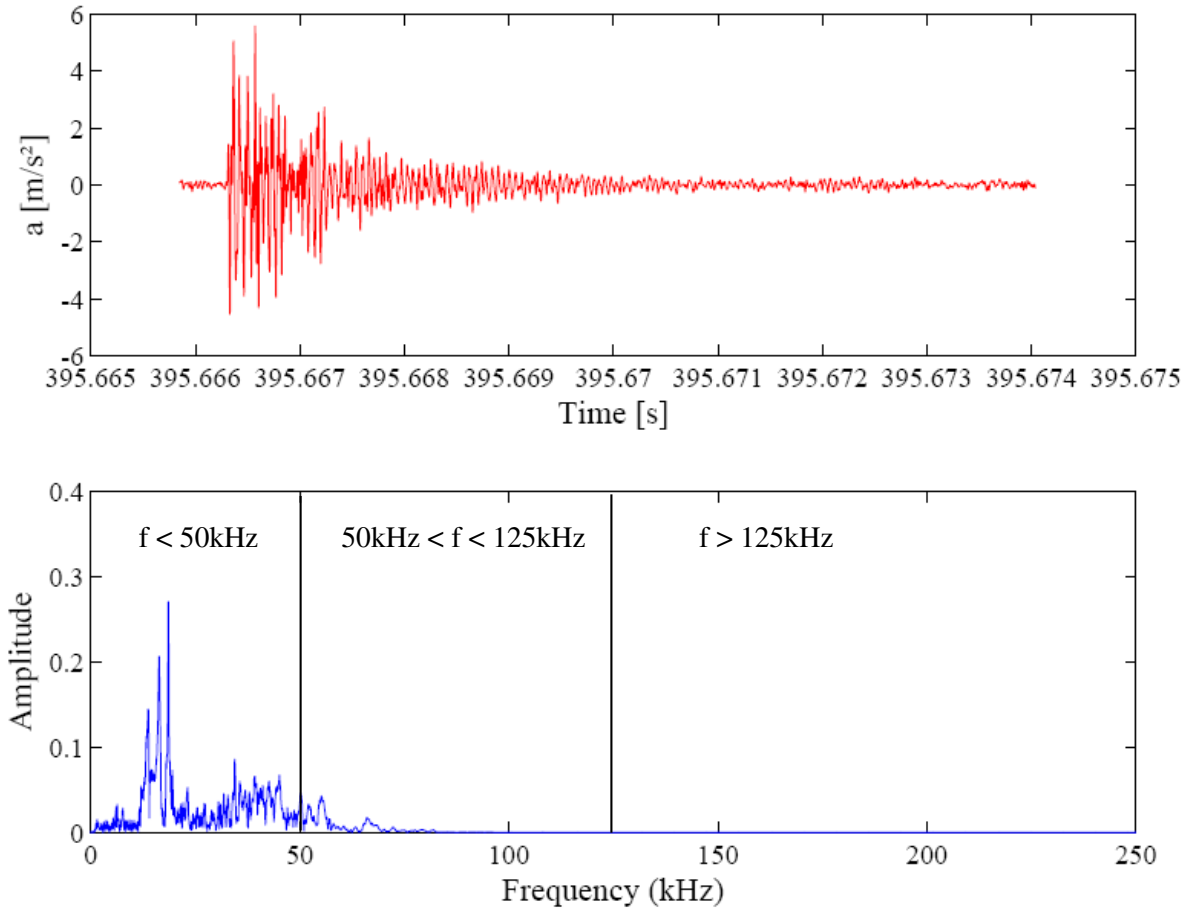

Fig. 4-5: Bandpass-filtered acceleration signal (top) and frequency spectrum (bottom)

In Fig. 4-5, the same acceleration signal than in the top plot of Fig. 4-3 is depicted which is filtered by the designed bandpass filter of Fig. 4-4. The signal seems to be thinned. The reason is the lack of higher frequency components that are attenuated by the bandpass filter. Regarding at the same time the signal spectrum at the bottom of Fig. 4-5, it can be seen that the designed bandpass filter significantly reduces low-frequency components, which are less than 2 Hz, and high-frequency components, above 50 kHz, while letting the signals with frequencies ranging from 2 Hz to 50 kHz pass through the filter. Now, the spectrum only contains frequencies in the range in which the acceleration sensors are calibrated.

4.3 Data Processing – Frequency Behaviour

In the following, the data processing of the converted signal is described and the data is analysed by the Fast Fourier Transform to shift the signals from the time into the frequency domain. The signal spectrum in the frequency domain gives information of the behaviour of the rock during the loading.

The signal recorded during the test contains information of the microacoustic events which occurred inside the sample during the loading. These microacoustic emissions result from the lengthening of a single microcrack or from the unification of two or more microcracks. During these processes, seismic waves are generated and propagate through the sample. At the surface, there are recorded by the acceleration sensors.

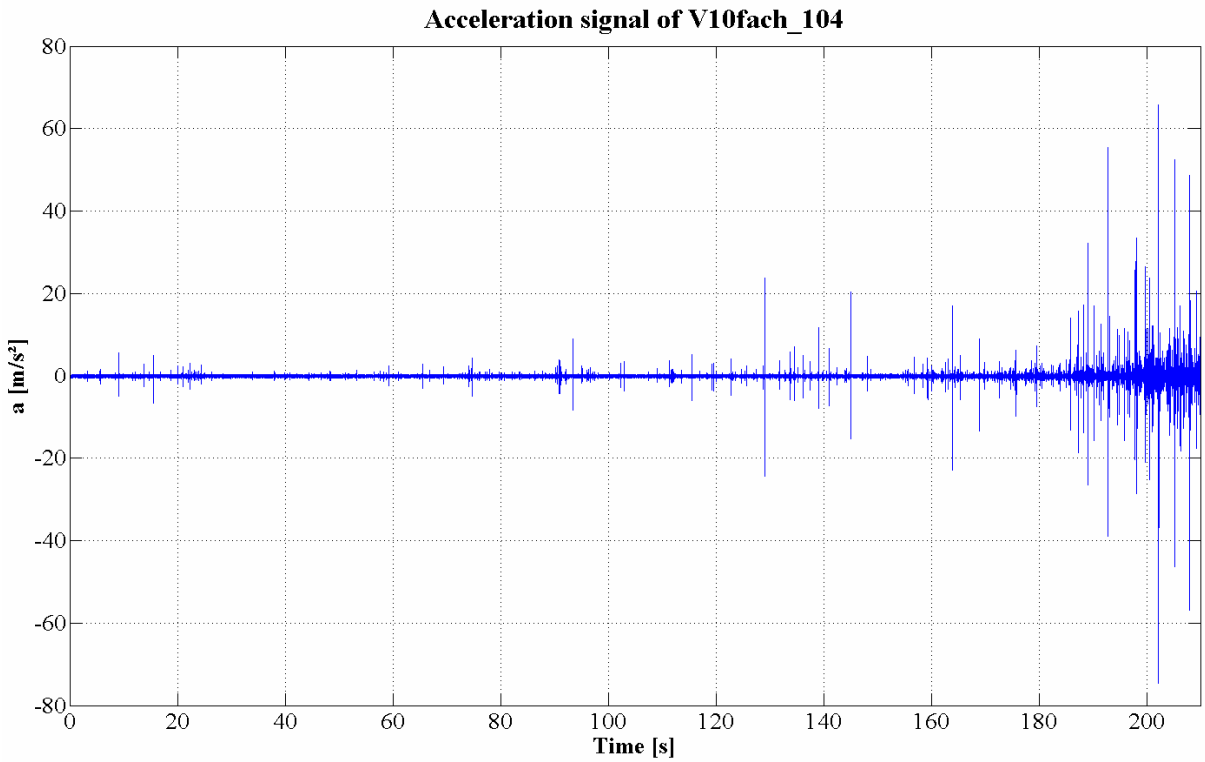

Fig. 4-6: Acceleration signal of the test 'V10fach_104'

In Fig. 4-6, the total data set of an acceleration signal is shown. In this example, the test lasted about 210 s and the maximum accelerations that occurred were about ± 80 m/s². At the signal, there are peaks which point to microacoustic events inside the sample. These peaks (i.e., top plot at Fig. 4-7) contain information about frequencies and amplitudes of these events. The FFT

application is the transformation of a finite-length digital signal into the spectrum in frequency domain.

The signal contains an ambient noise regarding the complete course of the test. The accelerations are oscillating around the zero line and the ambient noise reaches values of about a = ±1 m/s². The threshold value of the test has to be chosen in order to extract the microacoustic events out of the continuous signal. The event distinctly has to differ from the ambient noise of the signal.

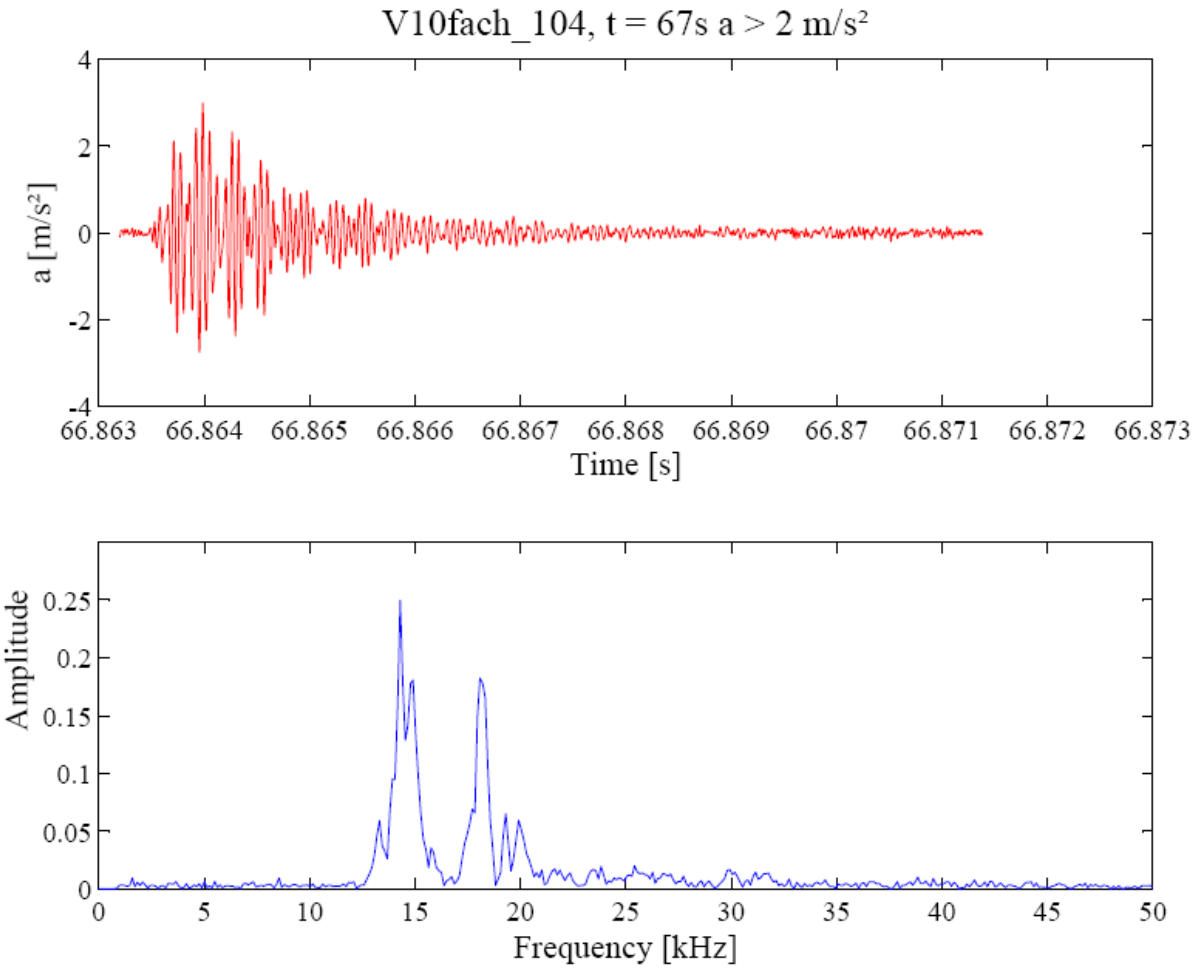

Fig. 4-7: Single event cut out of the signal

In the laboratory test, the threshold value is set at ± 2 m/s² (examinations for the threshold value are given in chapter 5.2). As soon as the value of acceleration is above ± 2 m/s², the peak is cut out of the signal. The single signal contains 128 sample points before and 1,919 sample points after the exceeding of the value (± 2 m/s²). Hence, the digital signal has a length of 2,048 samples. The signal with a sampling rate of 250 kHz has then a length of 8.192 ms. The event begins

and ends about the zero line. Then, the single event is analysed by the FFT to get the signal spectrum.

The event at the time of 67 s (see Fig. 4-7, top) is cut out of the acceleration signal and is analysed by the FFT algorithm. The spectrum of frequency gives information about the frequencies and amplitudes that characterize the event. Additionally, the point of time is given by cutting the event out of the total set of sample points and therefore, having the time component.

The algorithm to extract the signals is a self-written script in Matlab®. The signals are identified and cut out automatically within the script. There is a problem if two events occur in rapid succession and, therefore, the first signal is not completely fade out before the next one starts. Then, there are two events in the cut out interval of about 2,000 samples or 8 ms, respectively. If the signal is then analysed by the FFT algorithm, the signal spectrum gives information about both events. The frequencies interact and are superimposed with each other. Hence, the signal spectrum is not distinct.

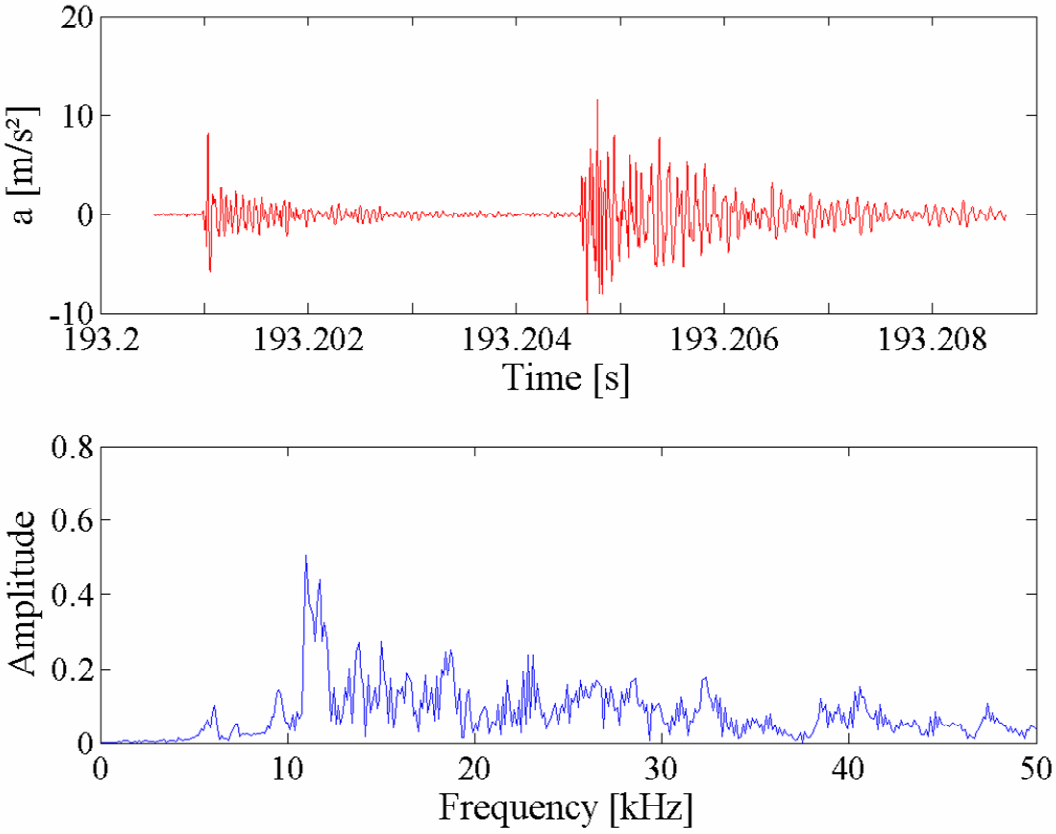

Fig. 4-8: Cut out signal with two events and the corresponding signal spectrum

Fig. 4-8 depicts this phenomenon. At the top, there is the cut out signal in which two events occur. Owing to the automatic mechanism, the signal spectrum contains the information of two events and, therefore, is not distinct. Furthermore, the second event within the cut out signal has a greater amplitude than the first and, hence, has a greater intensity. Nevertheless, the signal and its spectrum are not to use for the evaluation. These cut out signals have to be rejected and deleted to neglect a distortion of the results.

With this information, an analysis of the occurring events during the test set-up will be done in the following chapter ‘Analysis and Results of the Test Series’.

5 Analysis and Results of the Test Series

Up to now, there is a lack of knowledge about occurring frequencies in rock, especially in calcareous sandstone, resulting from changes in stress. The objective of this work is to examine the frequency behaviour in calcareous sandstone at different times during loading application.

During this research work, approximately 50 preliminary laboratory tests were carried out. Different adjustments as varying factors of gain (from no to 100-fold amplification) and various velocities of path-controlled load application were performed. The path-controlled velocities were set to 0.2 mm/min and 0.5 mm/min, respectively. The microacoustic emissions that were registered without amplification had too low amplitudes of accelerations and, therefore, many events were not recorded. Amplification by a factor of 10 and 100 increased the amount of microacoustic events, but with an amplification of 100, the events exceeded the limits of the sensors in the phase of postfailure. Hence, for the representation of the complete test series the amplification was tenfold and the specific phase of prefailure which is defined later in the text was examined by a gain factor of 100.

5.1 Phases in Stress-Time Curve

The uniaxial compression test was performed with path-controlled velocities of $v = 0.2$ mm/min and of $v = 0.5$ mm/min. The higher velocity of $v = 0.5$ mm/min was chosen to receive the complete signal of acceleration during the compressional test. The set-up with the lower velocity of $v = 0.2$ mm/min was taken to analyse the phase of prefailure more precisely.

Table 5.1: Maximum compressive strengths at time and strain

Test No.	σ_{max}	$t(\sigma_{max})$	$\varepsilon(\sigma_{max})$	**Test No.**	σ_{max}	$t(\sigma_{max})$	$\varepsilon(\sigma_{max})$
0.5	[N/m²]	[s]	[%]	**0.2**	[N/m²]	[s]	[%]
104	$14.2 \cdot 10^6$	194.7	0.63	**103**	$16.3 \cdot 10^6$	595.1	0.85
107	$12.6 \cdot 10^6$	182.6	0.58	**104**	$18.1 \cdot 10^6$	641.5	0.89
108	$12.9 \cdot 10^6$	205.0	0.86	**105**	$14.0 \cdot 10^6$	536.6	0.72
109	$13.5 \cdot 10^6$	205.3	0.83	**106**	$15.2 \cdot 10^6$	550.3	0.77
110	$12.0 \cdot 10^6$	186.9	0.70	**108**	$15.8 \cdot 10^6$	598.4	0.85

To compare the test series with varying path-controlled velocities, the results of ten test series regarding the maximum compressive strengths and their times as well as their strains are chosen and displayed in Table 5.1. In light-grey, there are the results of the tests which were carried out with a path-controlled velocity of 0.5 mm/min and tenfold amplification. The specimens failed at different maximum compressive strengths σ_{max} (from 12.0 N/m² to 14.2 N/m²) and their times of failure $t(\sigma_{max})$ also varied from 182.1 s to 205.3 s. The strain at the maximum compressive strengths covers the range from 0.58 % to 0.86 %. The light-blue part of Table 5.1 contains the maximum compressive strengths, their times and their strains of the test series which were loaded by a path-controlled velocity of 0.2 mm/min and a gain factor of 100. The specimens under lower velocities failed at higher compressive strengths (from 14 N/mm² to 18.1 N/mm²) and their times of failure occurred at a later time (from 536.6 s to 641.5 s), too. Analogous to the higher path-controlled velocity of 0.5 mm/min, the strain at the maximum compressive strengths increases and covers the range from 0.72 % to 0.89 %. Thus, the test series which are carried out with higher loading velocities have lower maximum compressive strengths. They are loaded by higher stresses in briefer time and, therefore, the test specimens have shorter periods of time to compensate the load application and break with a lower maximum compressive strength. Regarding the strain of the maximum compressive strength, it is increasing with decreasing path-controlled velocity. With lower path-controlled velocities, the specimens are capable to bear higher stresses because of greater time to compensate the load application – analogous to the time before. Thus, the maximum compressive strength and its strain hence depend on the chosen velocity.

The complete ten stress-strain curves described above with their maximum compressive strengths and their strains are shown in the following Fig. 5-1. The different maximum compressive strengths at various strains are clearly depicted.

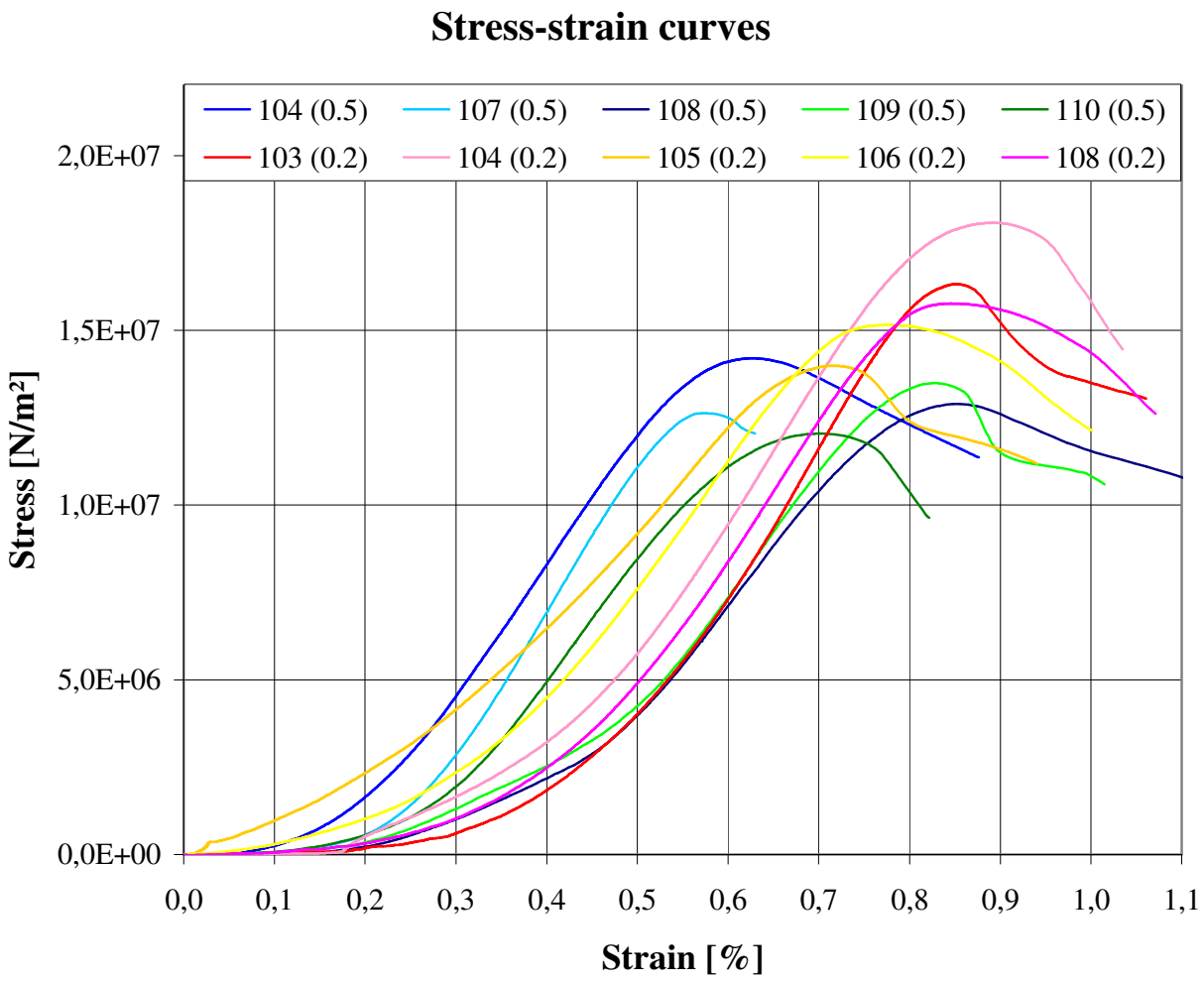

Fig. 5-1: Stress-strain curves with various path-controlled velocities

To show the similarities of the stress-strain curves with varying path-controlled velocities, the stress curves are normalized by the maximum compressive strength and its corresponding time. The transformation of strain to time is a convenient method because of the load application which is carried out with a path-controlled velocity and, therefore, strain and time are equivalent.

To compare the stress-time curves of different path-controlled velocities, the stress ratio depending on the maximum compressive stress of each curve is displayed over the time ratio (see Fig. 5-2). The time ratio is set at the maximum compressive stress of each test series.

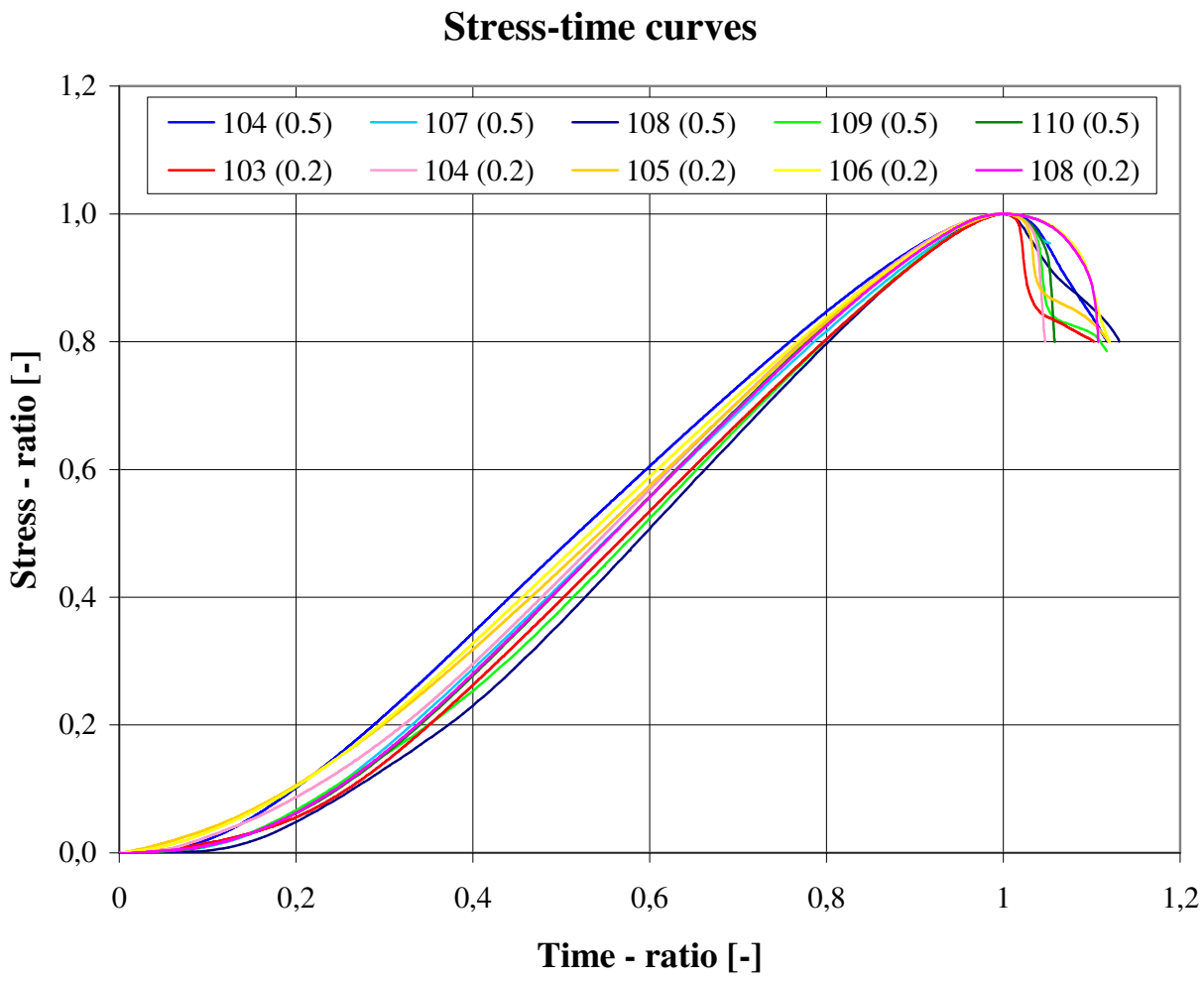

Fig. 5-2: Stress-time ratios of curves with various path-controlled velocities

With the stress and time ratios, the test series with different maximum compressive strengths and test durations are comparable. Regarding the shapes of the stress-time curves in Fig. 5-2, the specimens approximately behave the same under different loading velocities. Thus, the velocity does not influence the stress-time behaviour of the sample considering the shapes, especially the similar phases of the curves which are described in the following.

At the beginning, there are concave curves which merge into a linear elastic phase. Leaving the linear branch of the curve, the non-reversible deformations start – defined in this research as *prefailure*. If the maximum compressive strength is reached, the phase of *postfailure* starts and the macroscopic failure occurs.

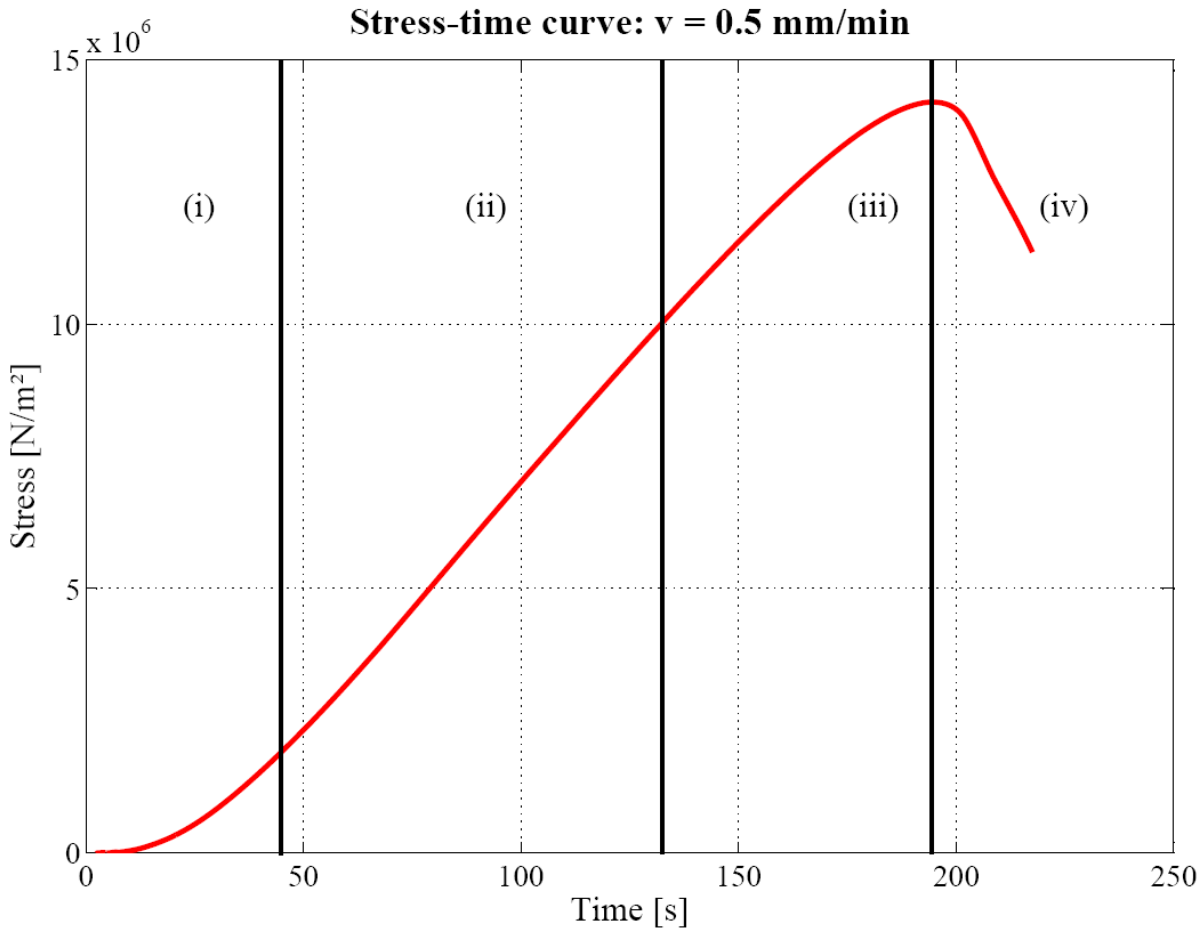

Fig. 5-3: Stress-time curve with a path-controlled velocity of 0.5 mm/min

The characterization and subdivision of the stress-time curve is exemplarily shown at a test series with a path-controlled velocity of 0.5 mm/min and is depicted in Fig. 5-3. Referring to SCHUBERT (2007), a subdivision of a uniaxial compression test in four phases is given as follows:

(i) At the beginning of the loading, there is a concave curve. One reason can be that the end faces are not parallel and, therefore, the load application is not exactly vertical. Another reason is a volume decrease resulting from closure of pre-existing microcracks inside the specimen.

(ii) The curve shows a nearly *linear* behaviour. After most of the microcracks have closed, an increase of stress produces rock compaction, consisting of pore deformation at an approximately linear rate. In porous rocks, like calcareous sandstone, the contacts between the grains break and the grains are rearranged due to stress concentrations around them.

(iii) With further increasing load application, microcracks increase and the strain increases disproportionately. At the end of linear elastic behaviour, the first non-reversible deformations start. The strength of the material has not yet reached the maximum strength but inside the sample local strength in sporadic points is exceeded. The exceedance of local strength results in breaking up the grain boundaries and, thus, in a release of elastic waves. Microcracks are prolonged and they coalesce with each other. In this work, the period between the ending of the linear elastic behaviour and the global maximum strength of the sample is defined as *prefailure*.

(iv) A further increase of load leads to a progressive rise of cracks and, finally, to the failure of the sample. The maximum strength of the sample is exceeded and the macroscopic failure occurs. In this work, this is defined as *postfailure*.

Table 5.2: Phases (i) to (iv) of the test series

Test No.	**Phase (i)**	**Phase (ii)**	**Phase (iii)**	**Phase (iv)**	**Test No.**	**Phase (i)**	**Phase (ii)**	**Phase (iii)**	**Phase (iv)**
	[s]	**[s]**	**[s]**	**[s]**		**[s]**	**[s]**	**[s]**	**[s]**
104	48	88	59	25	**103**	234	221	140	28
107	59	80	44	17	**104**	241	254	146	30
108	89	77	39	27	**105**	238	189	109	24
109	85	77	43	24	**106**	183	238	129	66
110	62	79	46	11	**108**	225	243	130	64
Mean	**68,6**	**80,2**	**46,2**	**20,8**		**224,2**	**229.0**	**130,8**	**42,4**

In Table 5.2, the time periods of different test series are summarized and separated by the various loading velocities (v = 0.5 mm/min in light-grey and v = 0.2 mm/min in light-blue). The different phases (i) – (iv) last various periods of time. Phases (i) and (ii) nearly take the same time depended on their loading velocities. The mean value of the prefailure phases almost halved and the phase till macroscopic failure further decreases. The short times of postfailure confirm

the brittle properties of the material calcareous sandstone. After reaching the maximum compressive strength, there is a rapid drop in the stress-time curve.

Referred to the four phases, the volume decrease of phase (i) nearly takes the same time than the compaction of the specimen with the pores closing. In the next phase of prefailure, the microcracks are prolonged and interact by coalescing. The phase takes less time than phases (i) and (ii), but the consequences on the loss of strength of the specimen are very significant.

Thus, the most important phase of the test is the period of time in which prefailure occurs, since observation of this period can provide information about the approaching macroscopic failure.

To examine the characteristics for the phase of prefailure, the bordering phases (ii) and (iv) are analysed and characterized in the following sections, too, and are compared to the phase of prefailure.

5.2 Amplitudes of Accelerations and Incidence of Events

As was shown in the previous section, the velocity of load application does not influence the stress which develops in the specimen due to loading. Hence, to reduce the amount of data and the computational time for data processing, the path-controlled velocity can be set to 0.5 mm/min. In Fig. 5-4, the accelerations which occurred in the sample during loading in the four phases and the resulting stress in the specimen (see Fig. 5-3) are shown over the time. The test series was done with an amplification factor of ten.

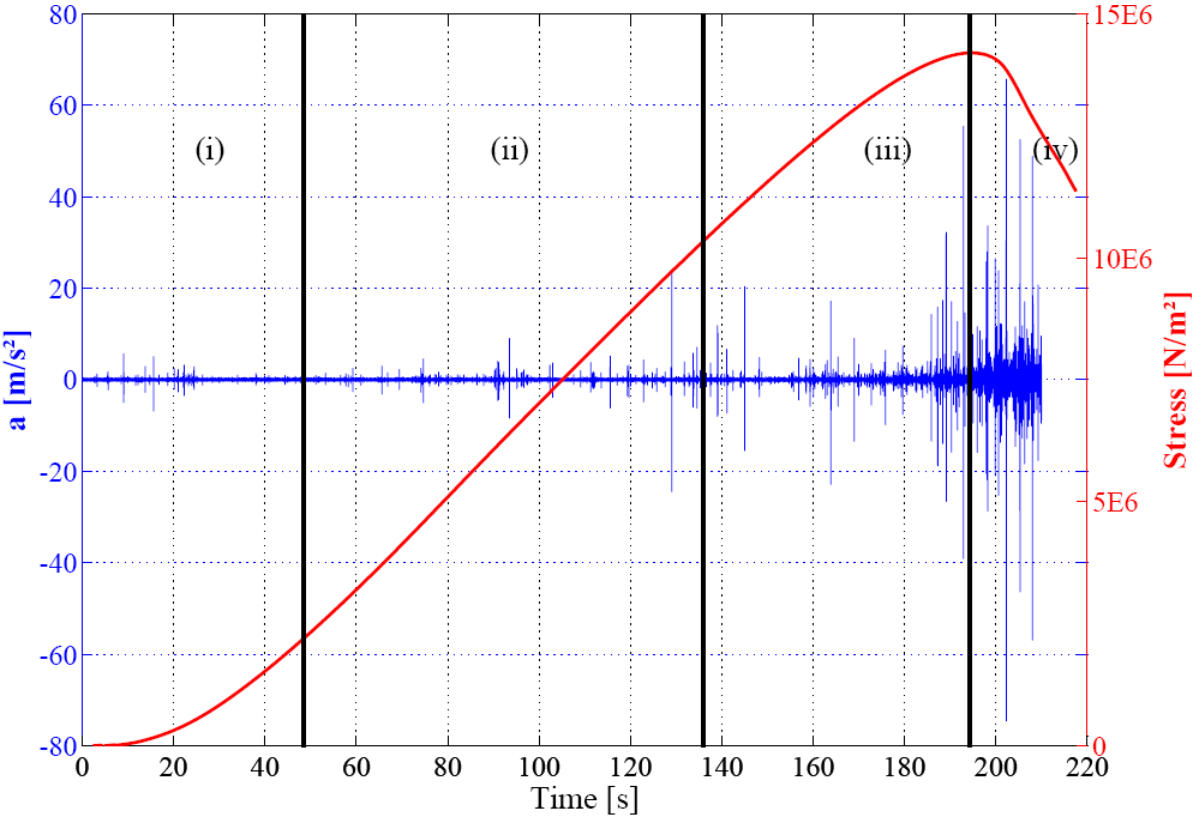

Fig. 5-4: Stress-time curve vs. acceleration signal

Regarding the amplitudes of accelerations of each single event (definition of an 'event' in subsection 4.3), it can be seen that the amplitudes of the acceleration signal in phase (i) stay below a = 10 m/s². They are occasional events in this phase in which pre-existing microcracks are closed and the volume of the sample is decreased, respectively.

In the following phase (ii), the accelerations stay below a = 10 m/s², too, but there's one single event at the end of this phase that exceeds the value of a = 10 m/s². The events are evenly distributed in the phase of the linear elastic behaviour. The compaction of the specimen which results from the collapse of the pores generates events with low amplitudes of acceleration.

During the phase of prefailure (phase (iii)), the recorded accelerations of the events frequently reach or even exceed the value of a = 20 m/s² and the incidence of events increases. Low and high amplitudes of accelerations are alternating. This phenomenon can be explained by the growth of pre-existing microcracks and by their coalescence to one greater microcrack. The amplitudes of accelerations are increasing and, after the coalescence of microcracks, the applied stress is exhausted and a period of lower amplitudes of acceleration

follows. At the end of the phase of prefailure, one single event exceeds the value of a = 50 m/s².

In the last phase (iv), both the incidence and the recorded accelerations of the events considerably increase. The accelerations reach peak values of greater than a = 50 m/s². The maximum acceleration is given by a_{max} = -75.57 m/s². In this phase, there is a progressive rise of microcracks which interact and coalesce on the basis of the applied stress. The maximum strength of the sample is exceeded and the macroscopic failure occurs.

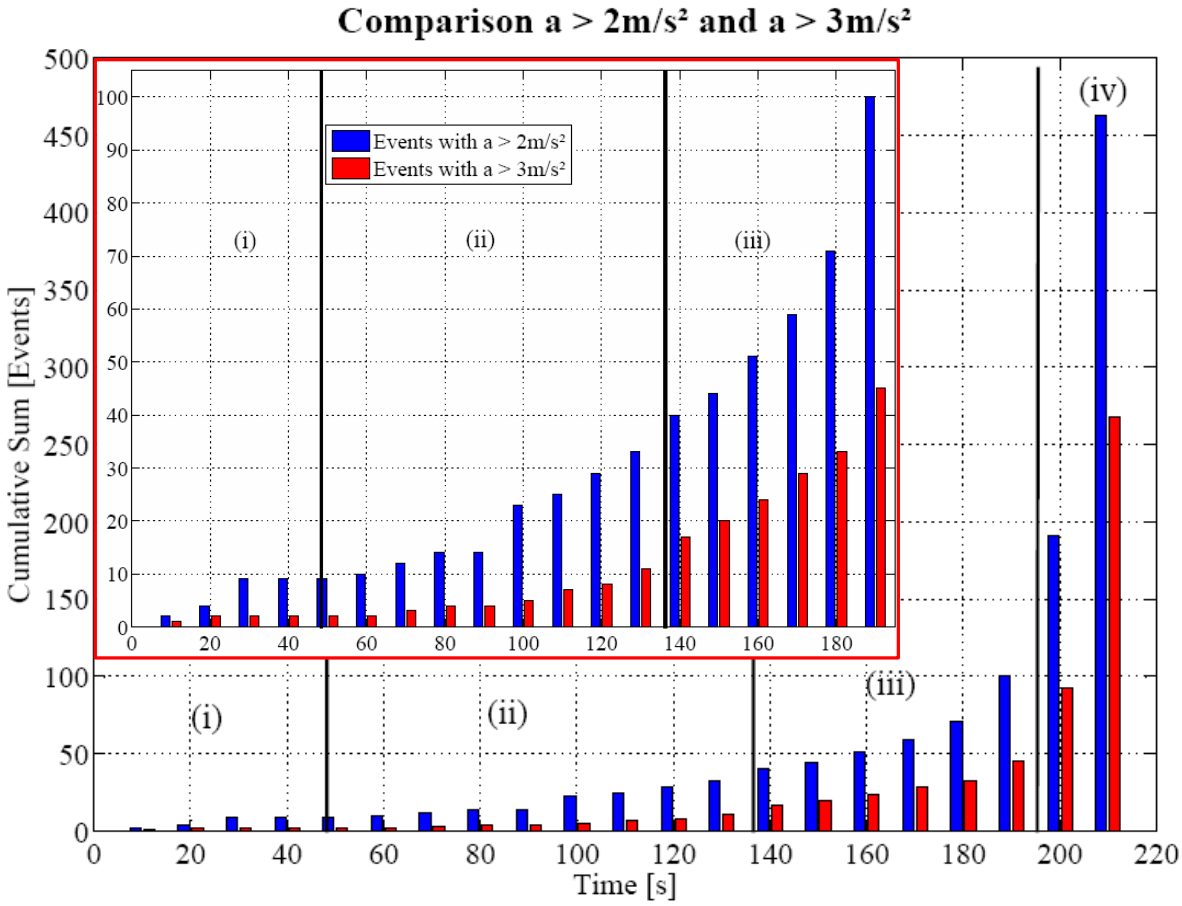

Fig. 5-5: Cumulative sum of events: phases (i) to (iv) (black frame) and phases (i) to (iii) (red frame)

The influence of the threshold of an event being an event was examined and the result is depicted in Fig. 5-5. The black frame of Fig. 5-5 shows the comparison of the amount of events which exceed a threshold value of a = 2 m/s² and a = 3 m/s² during the four phases. The blue bars indicate the cumulative sum of events that are greater than a = 2 m/s², the red bars analogue the events

$a > 3$ m/s². Each bar represents the cumulative sum of events during ten seconds. Independently of the threshold value, the cumulative sum of the recorded events is increasing. But it can be seen that the cumulative sum of events with $a > 2$ m/s² reaches double the amount of events with $a > 3$ m/s². Hence, in half of the events, accelerations between $2 \text{ m/s}^2 < a < 3 \text{ m/s}^2$ were observed.

The threshold value of $a = 2$ m/s² is chosen to distinguish between the ambient noise and the 'real' events. It is important to set the threshold value as low as possible and as high as necessary to get all information out of the signal.

The red frame in Fig. 5-5 depicts phases (i) to (iii), the last phase (iv) of postfailure is neglected and cropped of the diagram to get a closer look to the first three phases. In phase (i), there are only few events with $a = 2$ m/s² and $a = 3$ m/s². Whereas, nine events produce accelerations with $a > 2$ m/s², only two events produce accelerations with $a > 3$ m/s².In the linear elastic phase, the cumulative sum slightly increases over time. The events $2 \text{ m/s}^2 < a < 3 \text{ m/s}^2$ still take about two thirds of the sum of events. The cumulative sum of events with $a > 2$ m/s² increases from nine to 36 during the 88 seconds of phase (ii). In the phase of prefailure, the cumulative sum strongly increases. It starts with 40 events with $a > 2$ m/s² and ends with 100 events in a time of 59 seconds. That's almost a triplication of events in less time. The events with $a > 3$ m/s² take half of the events in the cumulative sum. Hence, the amplitudes of accelerations – besides the incidence– of the events increase as well.

The analysis of accelerations and incidence of occurring events shows different behaviour during the states of the loading. Starting with low amplitudes of accelerations and a small incidence in phase (i), there's a flat increase of events in the linear elastic phase. These events mainly have amplitudes of accelerations that range between $2 \text{ m/s}^2 < a < 3 \text{ m/s}^2$. In phase (iii) – the phase of prefailure – the gradient of increases is steeper and the amplitudes of accelerations increase. There is still half of the cumulative sum of events between $2 \text{ m/s}^2 < a < 3 \text{ m/s}^2$, but the events which are $a > 3$ m/s² take the second half of the cumulative sum. Hence, the peak accelerations of the events are increasing.

With the examination of the incidence of events and their amplitudes of acceleration, first characteristics are found out for the different phases during

load application. To complement the characteristics of the different phases, the recorded events are examined for their frequencies.

5.3 Signal Spectra

The time domain plot consists of ambient noise and the occurring events. In order to obtain the frequency content of a microacoustic signal, a Fourier analysis is performed which transforms the signal from time to frequency domain. The frequency corresponding to the maximum peak amplitude is known as the predominant frequency. The predominant frequency is the basic characteristic of a microacoustic signal.

Analysing the continuous signal with the FFT algorithm gives information about the occurring frequencies and their amplitudes in the recorded signal. To get a temporal relation of the frequencies obtained by the FFT, all related time steps are saved during the transform. So, it is possible to determine characteristic frequencies at different points of time and to define their dependency on the load stage. Hence, in a first step, the different signal spectra are regarded that occur in the different phases.

As mentioned before, the cut out signal of a microacoustic event gives information about the kind of microfracturing or the source event inside the sample, respectively. MANTHEI et al. (1993) gives a relationship between the duration and the frequency range of a generated event: The duration of an event is the time of the fracture process; the predominant frequency is proportional to the reciprocal duration of the event. The spectrum of an event with a long duration and a high energetic fracture process only contains low frequency components. Whereas, events with short durations and low energetic fracture processes result in signal spectra with high frequency components. Applying this to the microacoustic emissions of the laboratory test, the spectra with higher frequency components are generated, i.e., by the closure of pores or by the enlargement of single microcracks, whereas the spectra containing lower frequencies have higher energetic processes like interaction and coalescence of microcracks.

Up to now, there is no physical law to explain this phenomenon, but here is an attempt. Regarding a small event like the collapse of pores in the linear elastic

phase, the trigger event is locally and strongly limited. It takes only small deformations and short time. Hence, higher frequencies are generated by the fracture process. A greater energetic trigger event, e.g. the interaction and coalescence of microcracks, takes more space and time for the deformation and, therefore, the frequencies of the signal are decreasing.

The relationship between the energy content of a microacoustic event and its frequency components can be applied to the results of the laboratory tests, especially in considering the signal spectra. A classification of low or high energetic events by means of the frequencies is possible and can be applied to the signal spectra. In this research, low frequency components are given by $f < 20$ kHz and $f > 20$ kHz are declared as high frequency components.

5.3.1 Linear Elastic Phase (ii)

27 events with accelerations $a > 2$ m/s² were recorded in the linear elastic phase. They were cut out of the continuous signal and then analysed by the FFT algorithm to get the corresponding signal spectra of the events. The signal spectra of the 27 events have different distinguishing marks as different amount of peaks, various predominant frequencies or the range of frequencies changes. As examples, four of them are depicted in Fig. 5-6.

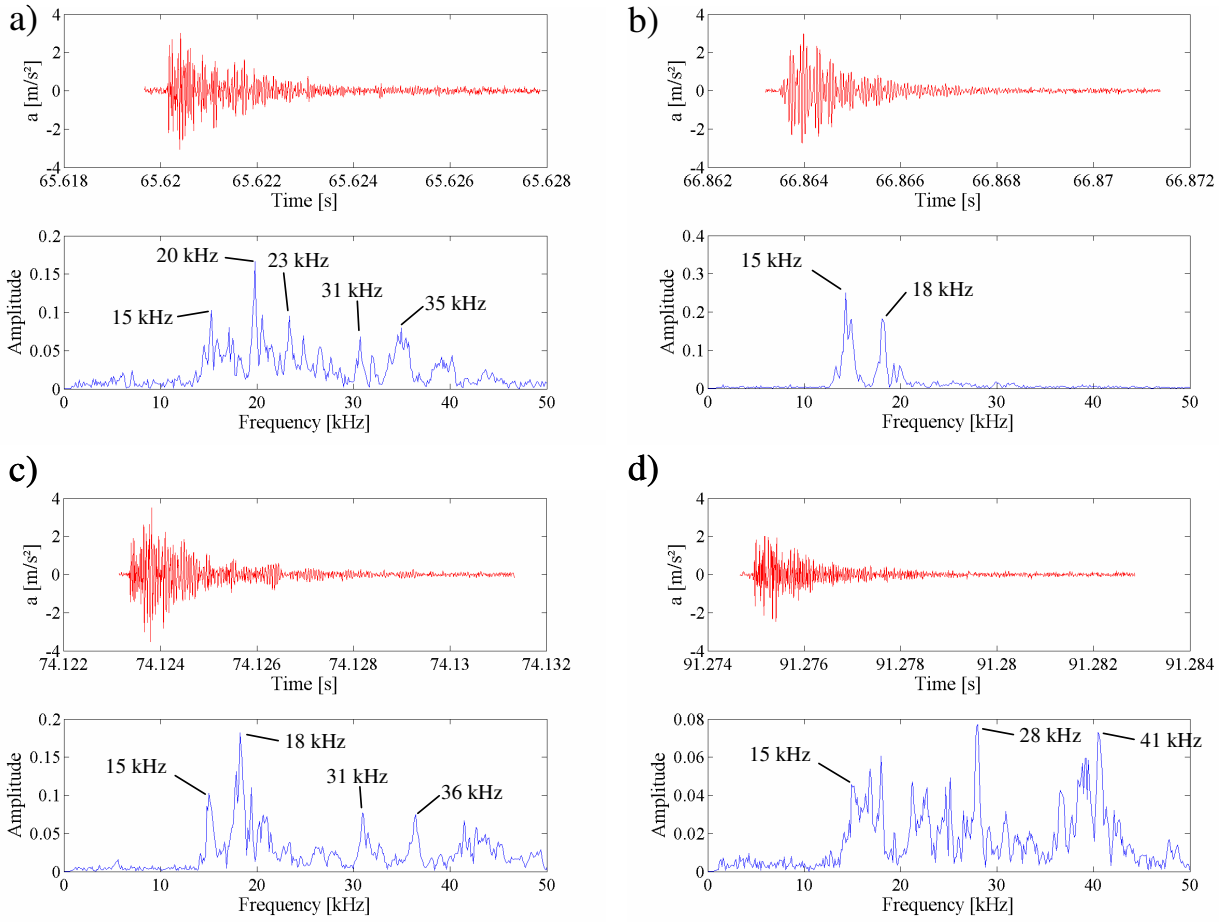

Fig. 5-6: Acceleration signals and their signal spectra a) to d) in the linear elastic phase

The red curve always indicates the acceleration signal that is cut out of the continuous signal. The blue curve below displays the corresponding signal spectrum of the signal. The signal spectra have different attributes in their appearances. In the signal spectrum of Fig. 5-6 a) for example, there are five peak amplitudes from 15 kHz to 35 kHz. The predominant frequency is given at 20 kHz. In this spectrum, there a low and high frequency components that are generated by a sum of different processes inside the specimen. Whereas, signal spectrum b) contains only two amplitude peaks at values of about 15 kHz and 18 kHz which, firstly, points to a longer duration of the fracture process and, secondly, to less types of processes. Regarding the spectrum of c), the predominant frequency is given at 18 kHz and three further frequency peaks (15 kHz, 31 kHz and 36 kHz) occur with amplitudes of about 0.1. In the last spectrum of Fig. 5-6 d), the frequencies begin at a value of 15 kHz and end at f = 41 kHz. In between, they are spread over low and high frequency

components. Thus, the signal is summed by different types of short and long durations' fracture processes.

The rest of 23 events in the linear elastic phase can be matched to one of the four examples of Fig. 5-6. The signal spectra in phase (ii) mostly contain low and high frequency components, thus, the signal is composed by different types of fracture processes. E.g., the high frequencies point to pores that are crushing. The lower frequencies result from enlargement of microcracks. Signal spectra with both low and high frequency components point to a combination or interaction of fracture processes. The predominant frequency reaches from 15 kHz (Fig. 5-6 b)) to 41 kHz (Fig. 5-6 d)). All signal spectra have in common that the lowest frequency peak is at about f = 15 kHz.

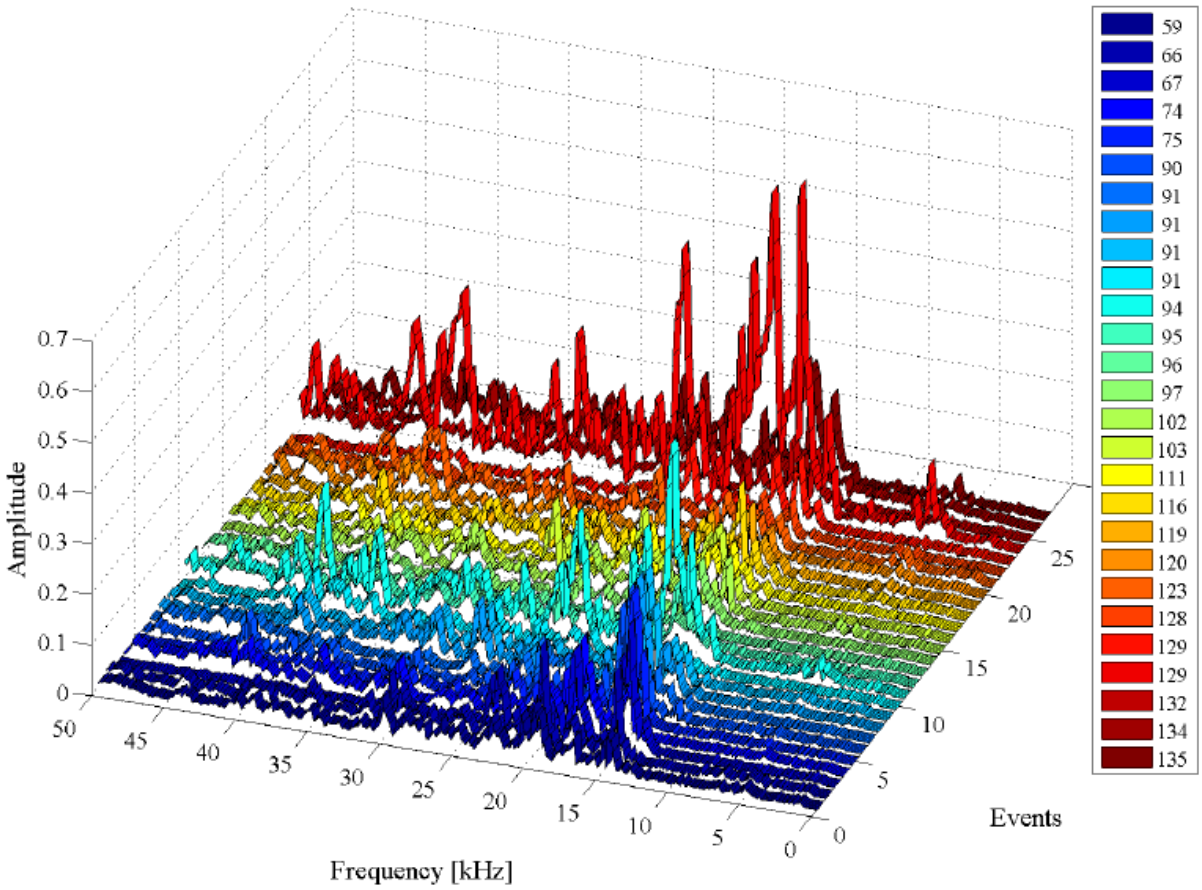

Fig. 5-7: Signal spectra of linear elastic phase

A different representation with the same facts is depicted in Fig. 5-7, where the spectra are shown in chronological order. (This and the following three-dimensional representations of the signal spectra are included in Appendix A with an enlarged format.) The time when the signal spectrum occurred is given

by the colour of the legend on the right side. E.g., the first dark blue line of the diagram belongs to the spectrum at the time of 59 s, the yellow spectrum at the middle of the diagram is given at the time of 111 s, and so on. The time step between the signal spectra is not proportional or fixed. It depends on the incidence of events during the different phases. For example, during the linear elastic phase, 27 microacoustic events with an acceleration greater than $a = 2$ m/s² occurred and are depicted in Fig. 5-7.

Regarding the signal spectra in this way of representation (Fig. 5-7), a significant characteristic becomes obvious again. Nearly all frequencies of the signal spectra in the linear elastic phase are greater than 15 kHz. There are two exceptions in the spectra at the second 94 s and 129 s, the 11^{th} and 24^{th} signal spectrum in the graph. In these spectra, there already occur frequencies below $f = 15$ kHz, but the amplitudes are quite small compared to the further amplitudes of their spectra.

Apart from that, the highest amplitudes have frequencies greater than 15 kHz. The signal spectra contain both components of lower and higher frequencies and the frequencies are evenly distributed.

5.3.2 Phase of Prefailure (iii)

The phase of prefailure begins with leaving the linear elastic branch of the stress-time curve. Each event with $a > 2$ m/s² that occurred during this phase is again cut out of the signal and analysed by the FFT algorithm to get the signal spectrum of each single event. In the phase of prefailure, 93 events occurred. Four of them which are representative of phase (iii) were chosen and are depicted in Fig. 5-9 with their cut out signals and their signal spectra.

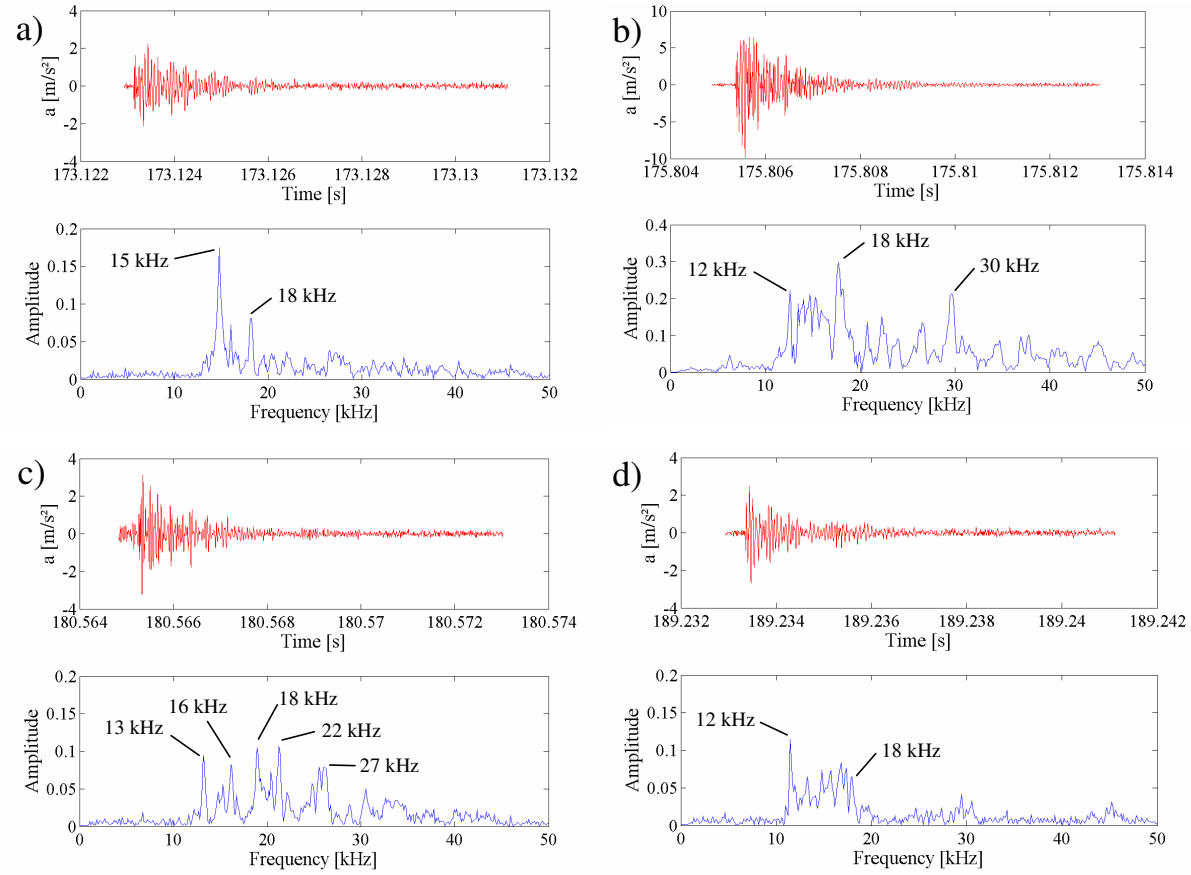

Fig. 5-8: Acceleration signals and their signal spectra a) to d) in the phase of prefailure

The signal spectrum of Fig. 5-8 a) has a predominant frequency of f = 15 kHz and a further peak at 18 kHz. These two peaks are the only ones inside the spectrum and they are low frequency components (f < 20 kHz), thus, the event at the time of 173 s results from fracture processes with longer duration and, therefore, has a higher energy content. High frequency components (f > 20 kHz) are not existent in this signal. In Fig. 5-8 b), the signal spectrum contains a frequency range from 12 kHz to 18 kHz with nearly same amplitudes of the frequencies and a further peak at 30 kHz. The predominant frequency is given by 18 kHz. The signal of Fig. 5-8 c) shows about five peaks in the range from 13 kHz to 27 kHz. A predominant frequency cannot be detected because all amplitudes of the frequencies are regularly distributed. Fig. 5-8 b) and Fig. 5-8 c) contain both low and high frequency components but the frequencies > 30 kHz are decreasing. This characteristic indicates that events with low energy contents are decreasing because, e.g., fracture processes with higher energy contents increase as prolongation of microcracks and their interaction and coalescence. In the last spectrum of Fig. 5-8, spectrum d), there are only low frequency components existent. The range reaches from 12 kHz to 18 kHz and

the predominant frequency is given at the lower limit with 12 kHz. The higher frequency components are completely missing in this spectrum.

The signal spectra in the prefailure phase differ from the ones of the linear elastic phase as follows: Firstly, the incidence of high frequency components ($f > 20$ kHz) is decreasing because the pores inside the sample are completely closed. And, secondly, the predominant frequencies are shifting to lower frequencies (12 kHz in Fig. 5-8 d) and 18 kHz in Fig. 5-8 b)). Thus, the energy content of the events is increasing in the phase of prefailure because microcracks are interacting and coalescing. There is a change in the fracture processes.

Since during the prefailure phase which lasts approx. 60 seconds, the number of events with $a > 2$ m/s² increases to 93 in total, the three-dimensional representation is split in three figures, Fig. 5-9, Fig. 5-10 and Fig. 5-11.The first plot represents the time from 136 s to 178 s, the second plot displays the time from 179 s to 190 s and the last representation shows the period of time from 190 s to 195 s, the end of the prefailure phase.

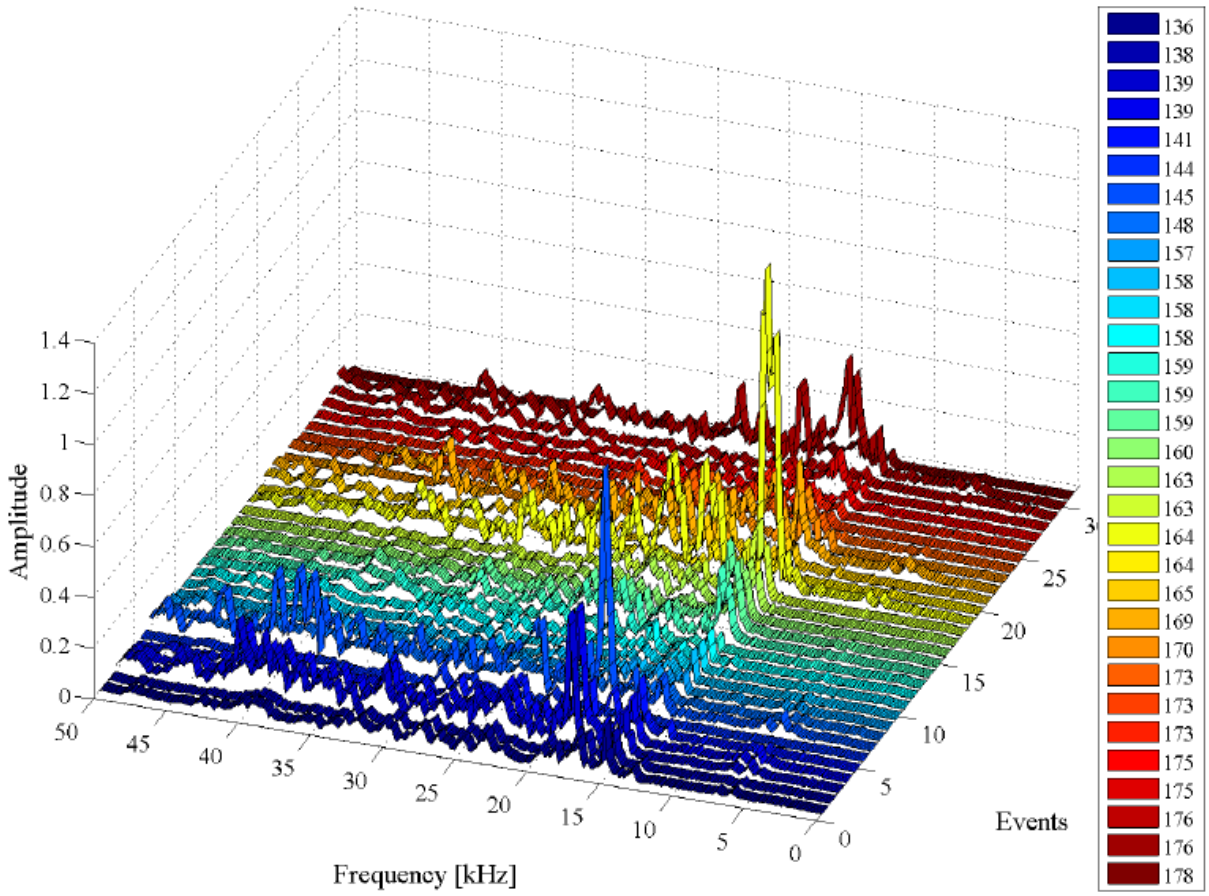

Fig. 5-9: Signal spectra of phase of prefailure – time from 136 s to 178 s

Analogous to the representation of the linear elastic phase, the signal spectra of the first 42 seconds of the prefailure phase are depicted in Fig. 5-9 with indication of their time of occurrence. The colour bar on the right side again displays this time.

The signal spectra still contain both components of lower and higher frequencies. But there is a decrease of the lowest value of the first frequency peak in the signal spectra. The spectrum at time 136 s has the first peak at a frequency of 15 kHz. With increasing time, the frequency of the first peak decreases. In the last signal spectra of Fig. 5-8 at 178 s, the peak value has a frequency of 13 kHz. Later in this section, Fig. 5-12 depicts the decrease of the frequency of the first peak over the complete phase of prefailure.

A further conspicuousness is an accumulation of events and a following silent period. It directly starts at the first spectra from 136 s to 145 s. There is an accumulation of seven events in nine seconds. The amplitudes of the frequencies are increasing and both lower and higher components are occurring in the spectra. After the high amplitude of the spectra at 145 s, there is one event with amplitudes < 0.1 and it follows a period without significant frequency emissions of about 9 s (see also red arrow in Fig. 5-12). The reason for this period can be that the prior events are generated from increasing microcracks which in the following interact and coalesce. The coalescence contain a high amount of energy, so the applied stress is exhausted and it takes some time to apply sufficient stress to generate further fracture process inside the sample. Hence, after a period of events with increasing amplitudes, there follows a period without significant frequency emissions in which the stress has to be accumulated for further fracture processes. This phenomenon recurs in Fig. 5-9 at time 170 s with a smaller period without microacoustic emissions of 3 s (see also red arrow in Fig. 5-12).

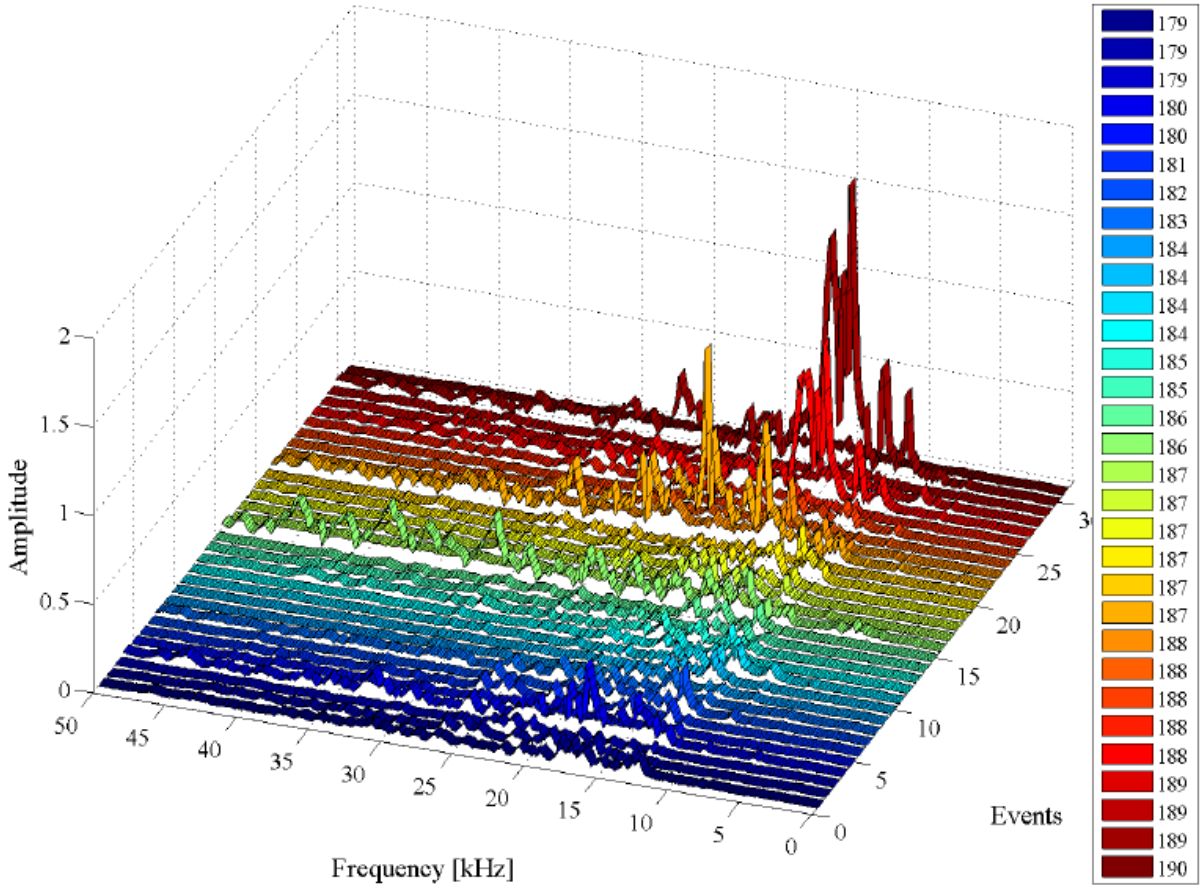

Fig. 5-10: Signal spectra of phase of prefailure – time from 179 s to 190 s

Fig. 5-10 shows the time from 179 s to 190 s in the phase of prefailure. Regarding the first signal spectrum at 179 s, a postponement of the first peak to lower frequencies is obvious. The peak value of the first spectrum has a frequency of 13 kHz. The last signal spectrum in Fig. 5-10 has its first peak at a frequency of 10 kHz. Thus, with increasing time, there is a further decrease of the lowest frequency value (see also Fig. 5-12).

In the time from 179 s to 190 s, there are less signal spectra with both components of lower and higher frequencies. Occasionally, the signal spectra contain a wide range of frequencies, but the highest amplitudes occur in the frequency range from 10 kHz to 20 kHz, hence, at the low frequency components < 20 kHz. The phenomenon described at Fig. 5-9 of an accumulation and a following period without microacoustic emissions cannot be detected in the second phase of the prefailure phase. Therefore, the described phenomenon occurs mainly at the beginning of the phase (iii) because the specimen is in the state of the first non-reversible deformations and the applied stress level enables the sample to ‘relax’. With increasing stress, the fracture

processes increase, too, which also explains the decrease of the frequency components.

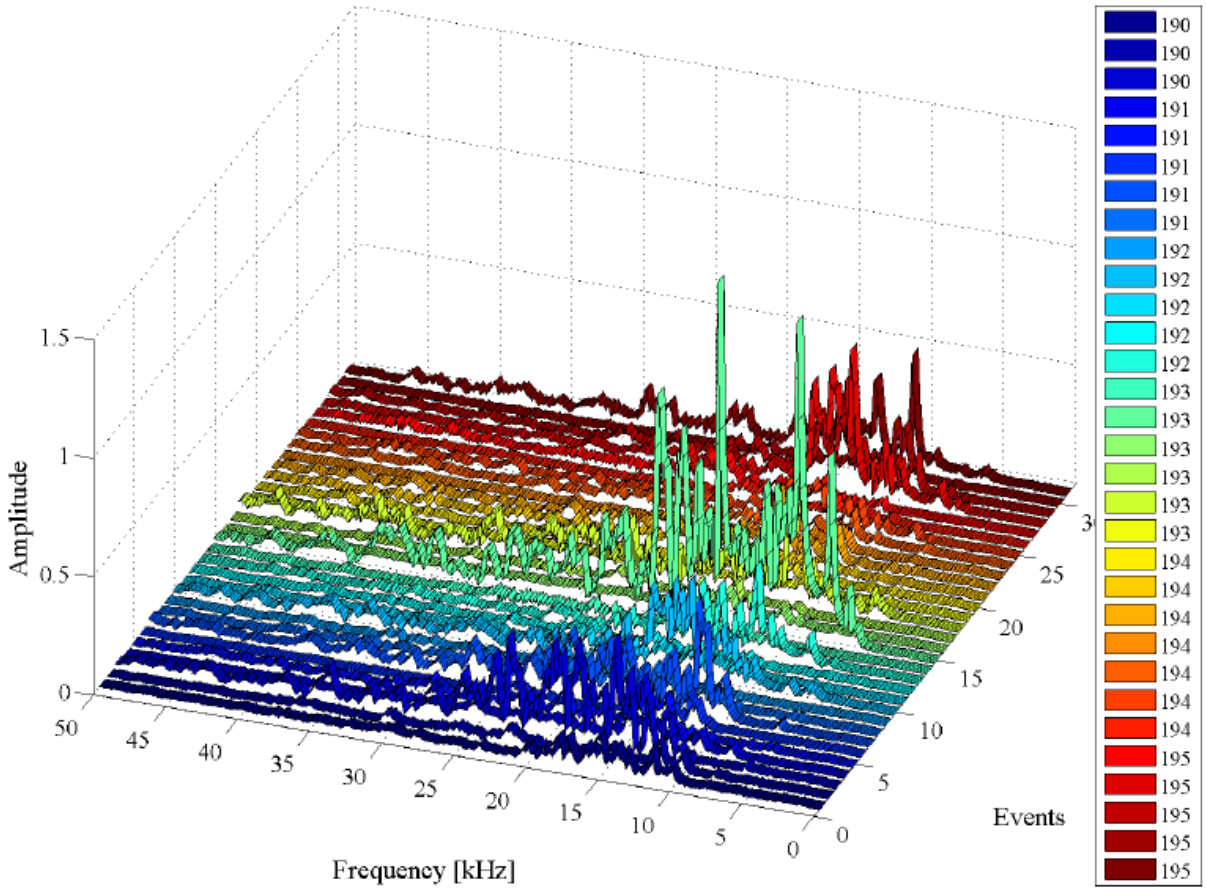

Fig. 5-11: Signal spectra of phase of prefailure – time steps 190 s to 195 s

In the last phase of prefailure (see Fig. 5-11), the lowest peak frequency rests at a value of 10 kHz. Sporadically, there are first peaks with lower frequencies but the main peak remains at a frequency of 10 kHz.

As detected in Fig. 5-10, there are occasionally signal spectra with both components of lower and higher frequencies in the last phase of the prefailure phase. But the majority of signal spectra have their occurring frequencies in the lower frequencies – namely in the frequency range from 10 kHz to 20 kHz. The highest amplitudes of the spectra are in this range.

Regarding the different periods of time that are included in the figures Fig. 5-9, Fig. 5-10 and Fig. 5-11, it is obvious that whereas all graphs depict the frequencies of 31 spectra, the period of time in which this number of spectra occur decreases (Fig. 5-9: 42 s, Fig. 5-10: 11 s and Fig. 5-11: 5 s). Hence, there

is an increase of events with progressing time. This phenomenon has already been described in Chapter 5.2.

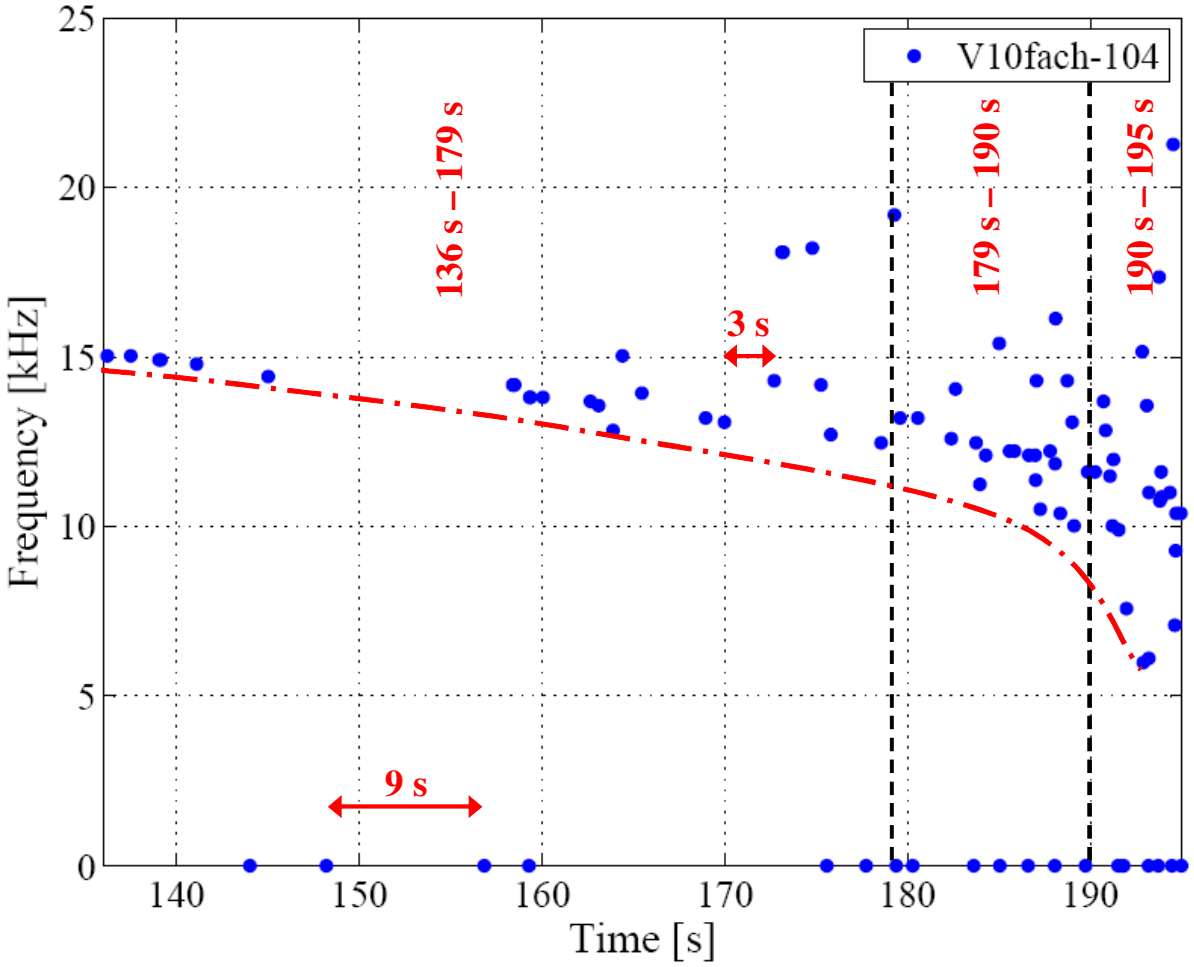

Fig. 5-12: Frequencies with amplitudes > 0.1 in the prefailure phase

As shown before, there is a decrease of the first frequency peak in the signal spectra in the prefailure phase. Since the three-dimensional representation of phase (iii) is split into three figures and a complete view of this phase is not given, a two-dimensional plot of the behaviour of the frequency peak over time is shown in Fig. 5-12. The blue dots indicate the first frequency peak of each signal spectrum that has a greater amplitude than 0.1. The dots of the frequency peaks with f = 0 kHz did not exceed the threshold of an amplitude of 0.1 in the signal spectra and, therefore, the first frequency peak of these signal spectra is not depicted. The dot-dash line indicates the temporal course of the first frequency peak in the phase of prefailure which behaves exponentially over time.

Since during increasing applied stress the local strength inside the specimen is exceeded and the global strength decreases, there is an increase of fracture processes inside the specimen which includes an increase of events with higher energy contents and, therefore, a decrease of the frequency components.

The results of the test series of Table 5.1 and Table 5.2, respectively of the prefailure phase are given in section 5.3.4.

5.3.3 Phase of Postfailure (iv)

After reaching the maximum compressive strength of the sample, the fourth and last phase of the laboratory test begins. It concerns the phase of the postfailure in which the sample reachs the macroscopic failure.

In the phase of postfailure, there is a rapid increase of events (see Fig. 5-5) and the time interval between the single events is decreasing. Partly, the events occur in high sequences, so that a consideration and analysis of the single event is impossible. If there is only a small time interval between the events, the second event starts before the first one has subsided again to the ambient noise (see Chapter 4.3). Hence, there is a great amount of cut out signals in the phase of postfailure that are not unique.

331 signals were automatically cut out by the Matlab® script for the postfailure phase. 105 of them contained two or more events; hence, a unique solution for these 105 signals is not given by the FFT analysis. The 105 signals were manually sorted out and are not taken for the evaluation of this phase. The remaining 226 unique signals can be analysed by the FFT analysis and evaluated to get a reasonable consideration of the microacoustic events.

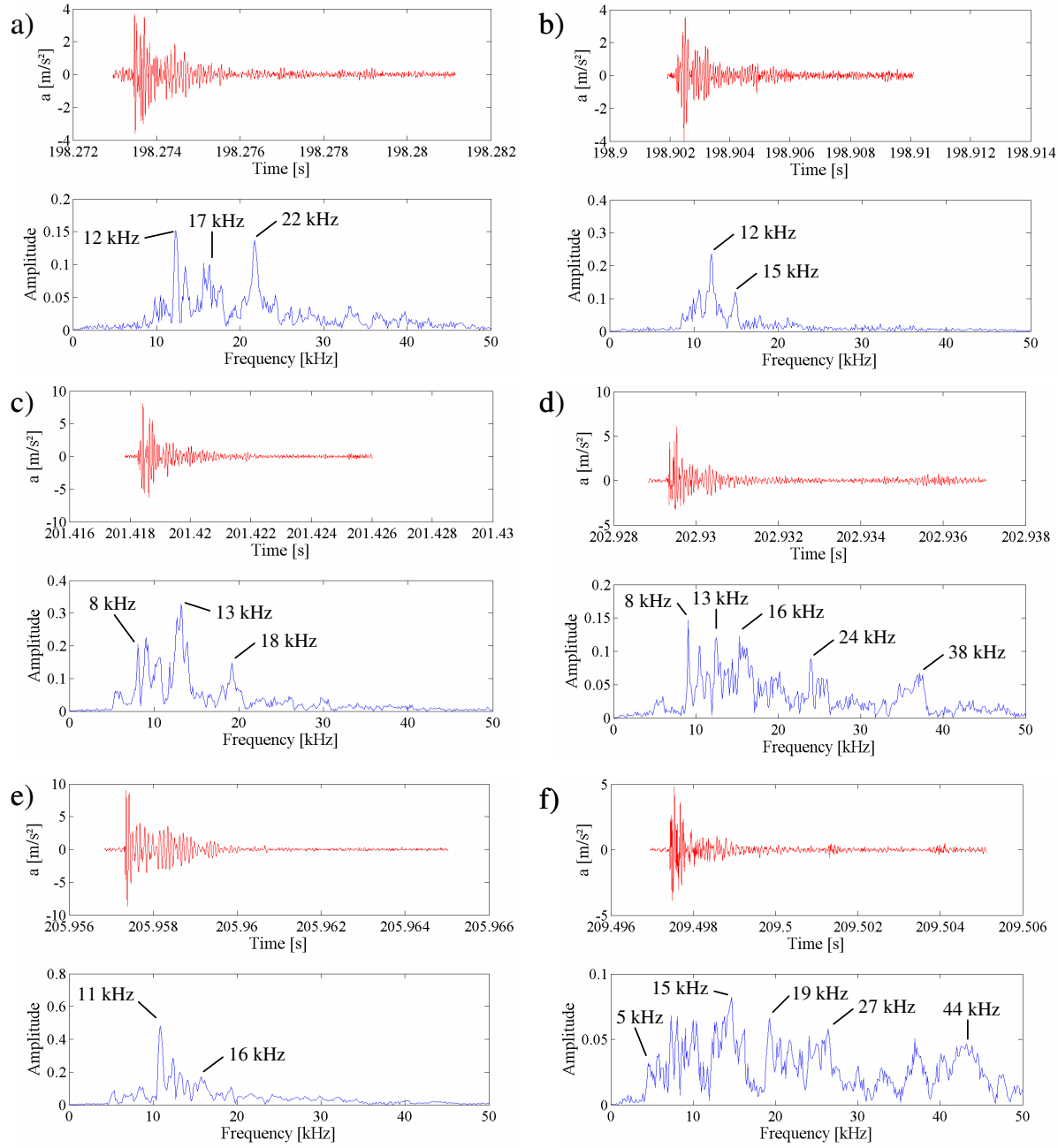

Fig. 5-13: Acceleration signals and their signal spectra a) to f) in the phase of postfailure

In Fig. 5-13, six of the 226 signal spectra are chosen to display different types of spectra. They differ in their frequency range or in their number of peak values. The signal spectrum in Fig. 5-13 a), e.g., contains three peak values at 12 kHz, 17 kHz and 22 kHz. The frequency range is limited from 12 kHz to 22 kHz. Fig. 5-13 c) also contains three frequency peaks, but the lowest frequency is given at 8 kHz and the highest at 18 kHz. The signal is composed of different types of fracture processes which generate specific frequency components. In Fig. 5-13 b) and e), there are only two frequency peaks; hence, there are less fracture

processes for generating the microacoustic event. The signal spectra of Fig. 5-13 d) and f) contain a larger number of frequency peaks and the frequency range is extended in d) from 8 kHz to 38 kHz and in f) from 5 kHz to approx. 44 kHz. Therefore, the events result from many parallel fracture processes inside the specimen.

In Fig. 5-13, only six of 226 signals are depicted. In order to determine the characteristics of the total part of postfailure and to illustrate the differences to the linear and prefailure phase, the signal spectra are again displayed in the three-dimensional and chronological plot.

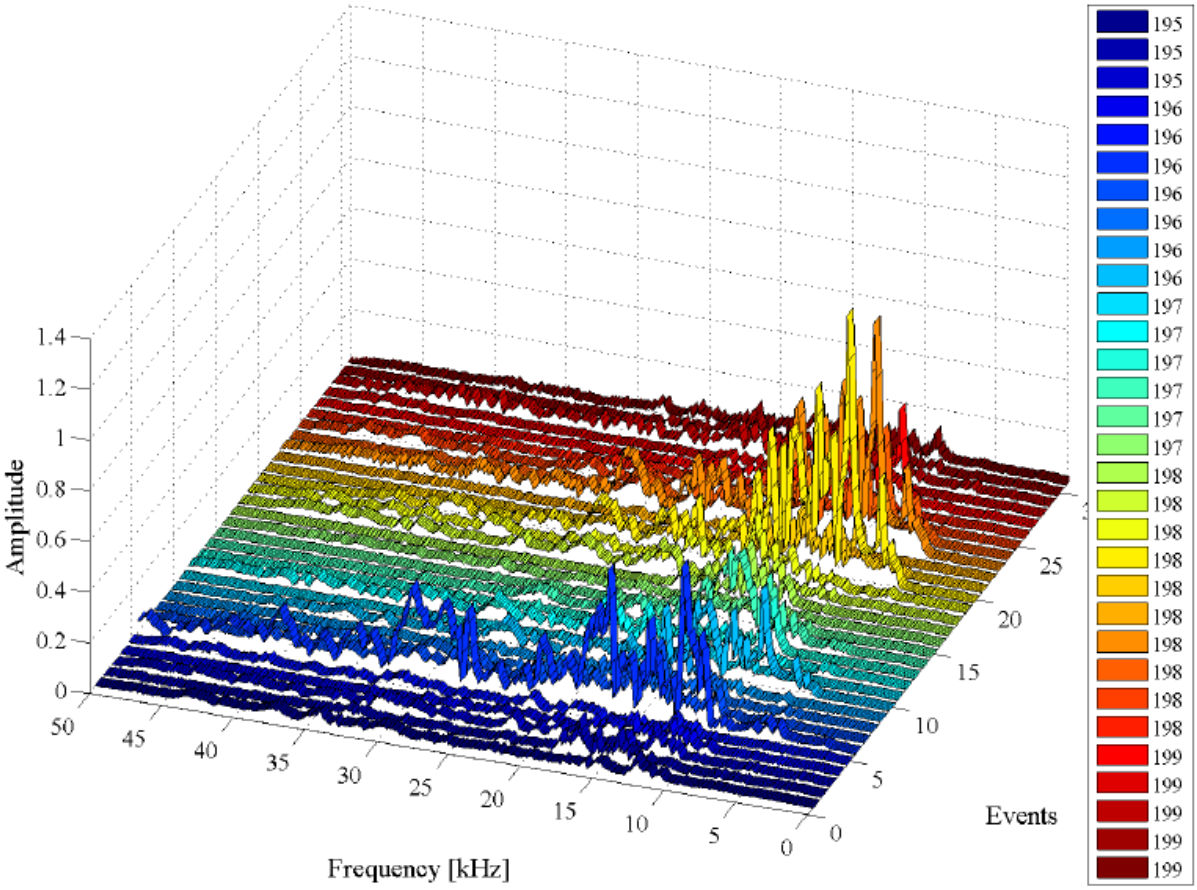

Fig. 5-14: Signal spectra of phase of postfailure – time from 195 s to 199 s

The first four seconds and their 31 signal spectra of the phase of postfailure are shown in Fig. 5-14 in their chronological order of occurrence. At the beginning of the postfailure phase, the first five signal spectra have very small amplitudes and their lowest frequency peak is at the values from 10 kHz to 12 kHz – analogous to the last phase of the phase of prefailure. The amplitudes of the frequencies in Fig. 5-14 rise and fall but are mainly at the lower frequency

components; hence, the fracture processes result from greater events. With progressing time, the lowest frequency peak decreases. From the 10^{th} signal spectrum on, the lowest frequency peaks frequently fall below a value of 10 kHz. The predominant frequencies take place at the low frequency components ($f < 20$ kHz). There are still frequency components with higher frequency values ($f > 20$ kHz) but they only occur occasionally and have smaller amplitudes than the lower frequencies. Hence, the microacoustic events with lower energy contents decrease and the energy of the fracture processes inside the specimen increase with progressing time.

The plots of the spectra during the time 199 s and 202 s – each containing 31 signal spectra – are depicted in the Appendix A since they behave similar to Fig. 5-14.

The next 31 signal spectra of the phase of postfailure occurred in the time period of 202 s to 204 s and are depicted in Fig. 5-15. At the times of approx. $t = 202$ s, the lowest frequency components are at 8 kHz. With progressing time, the lowest frequency component further decreases. The last signal spectrum in Fig. 5-15 has its lowest frequency at 7 kHz. The predominant frequency components are at the lower frequency range. There are only few signal spectra with high frequency components ($f > 20$ kHz) and these frequency components have low amplitudes. Hence, the influence of higher frequencies is decreasing in time. Again, the fracture processes inside the sample generate frequencies at the lower components and, therefore, have increasing energy contents.

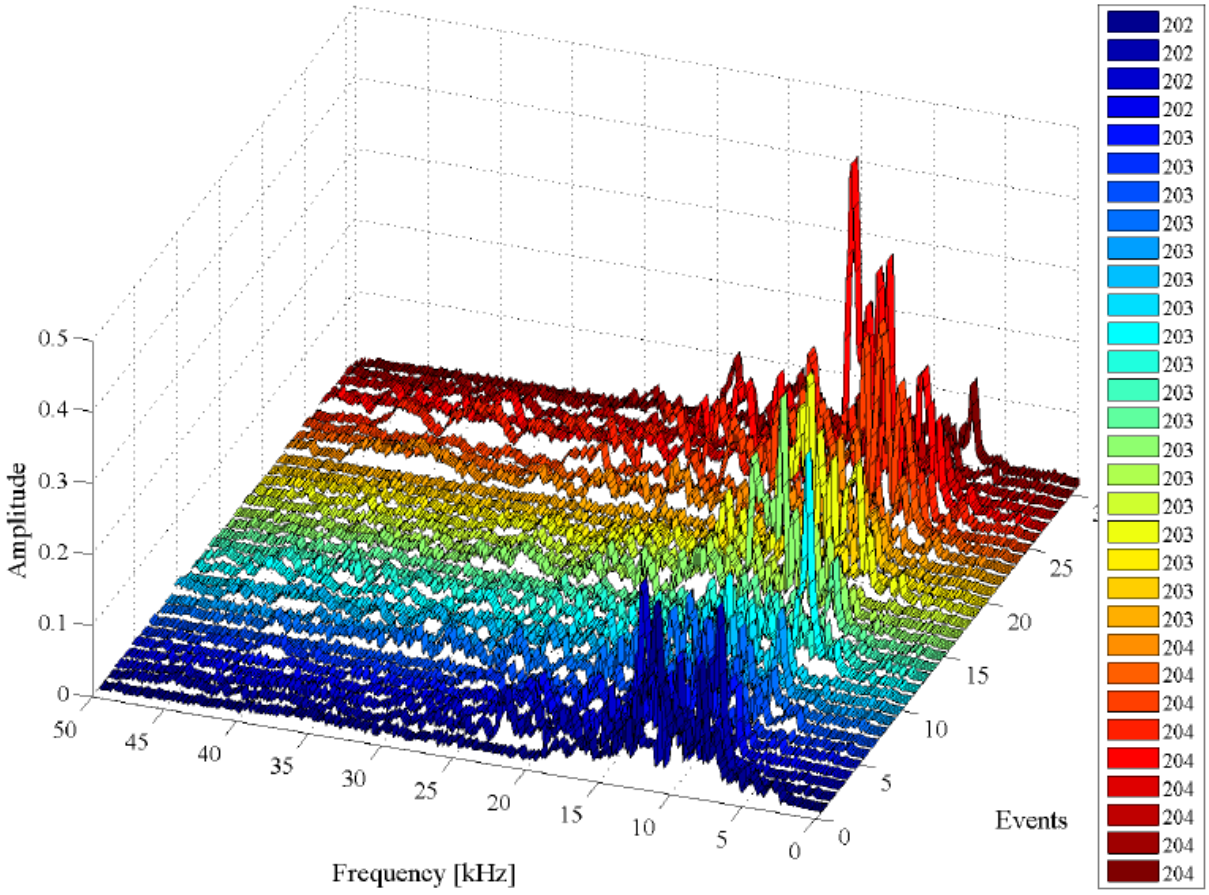

Fig. 5-15: Signal spectra of phase of postfailure – time from 202 s to 204 s

The congruent signal spectra in Fig. 5-15 point to equal fracture processes and equal energy contents inside the sample. As mentioned earlier, in the phase of postfailure, there is a progressive rise of cracks. The already coalesced microcracks further increase and coalesce with further microcracks. The energy content of the fracture processes increases and the frequency components decrease with progressing time in phase (iv). The course of frequencies is also shown in Fig. 5-17 in a two-dimensional plot.

The representation of the spectra during the time 204 s and 206 s is skipped and is depicted in the Appendix A since there are three signal spectra in the plot with high amplitudes and, therefore, the remaining signal spectra are hardly to examine owing to their relatively low amplitudes.

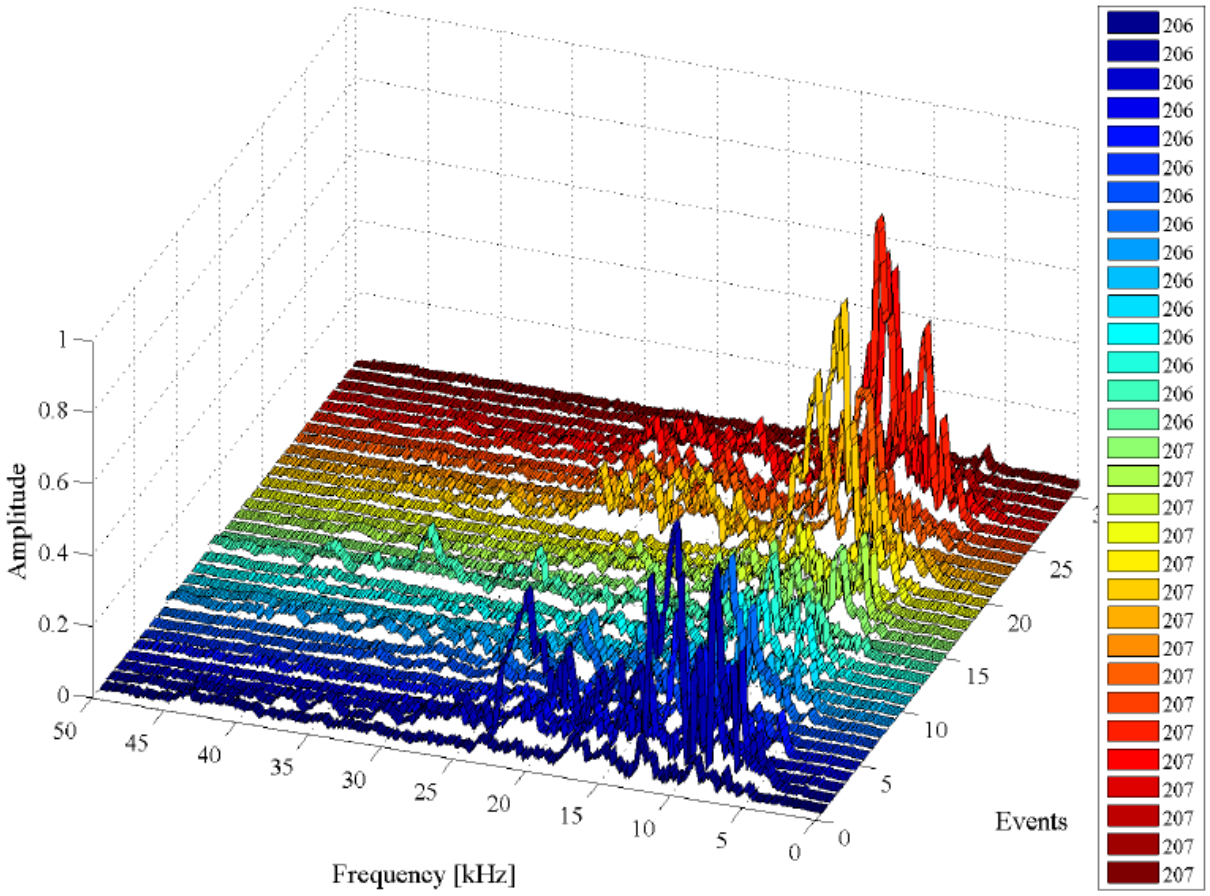

Fig. 5-16: Signal spectra of phase of postfailure – time from 206 s to 207 s

The signal spectra at the time from 206 s to 207 s in Fig. 5-16 show similar characteristics as the plots before (Fig. 5-14 and Fig. 5-15). The amplitudes of the frequencies rise and fall but are mainly at the lower frequency components; hence, the fracture processes result from greater events. The main frequency range covers low frequency components and the lowest frequency peaks have values of about 6 kHz. The high frequency components are nearly vanished and, therefore, are less decisive for the analysis.

The plots of the spectra during the time 207 s and 210 s are depicted in the Appendix A. In the plot of the signal spectra from 207 s to 209 s, there is again one signal spectrum which contains a frequency component with a very high amplitude so the rest of the signal spectra show relatively small amplitudes and an evaluation is not practical. The last twelve signal spectra from 209 s to 210 s have the same characteristics than Fig. 5-16 and, therefore, can be skipped, too.

In conclusion, the signal spectra in the phase of postfailure show specific characteristics: The predominant frequencies occur at the lower frequency

components (f < 20 kHz), whereas, the higher frequency components are rare and have small amplitudes. In addition, the lowest frequency peak of the signal spectra decreases with progressing time (see also Fig. 5-17). Hence, the fracture processes inside the specimen are very similar and, therefore, the signal spectra are nearly congruent and behave the same. The decrease of the lowest frequency peak results from the increase of the energy contents of the microacoustic events. More and more microcracks interact and coalesce until the specimen fails macroscopically.

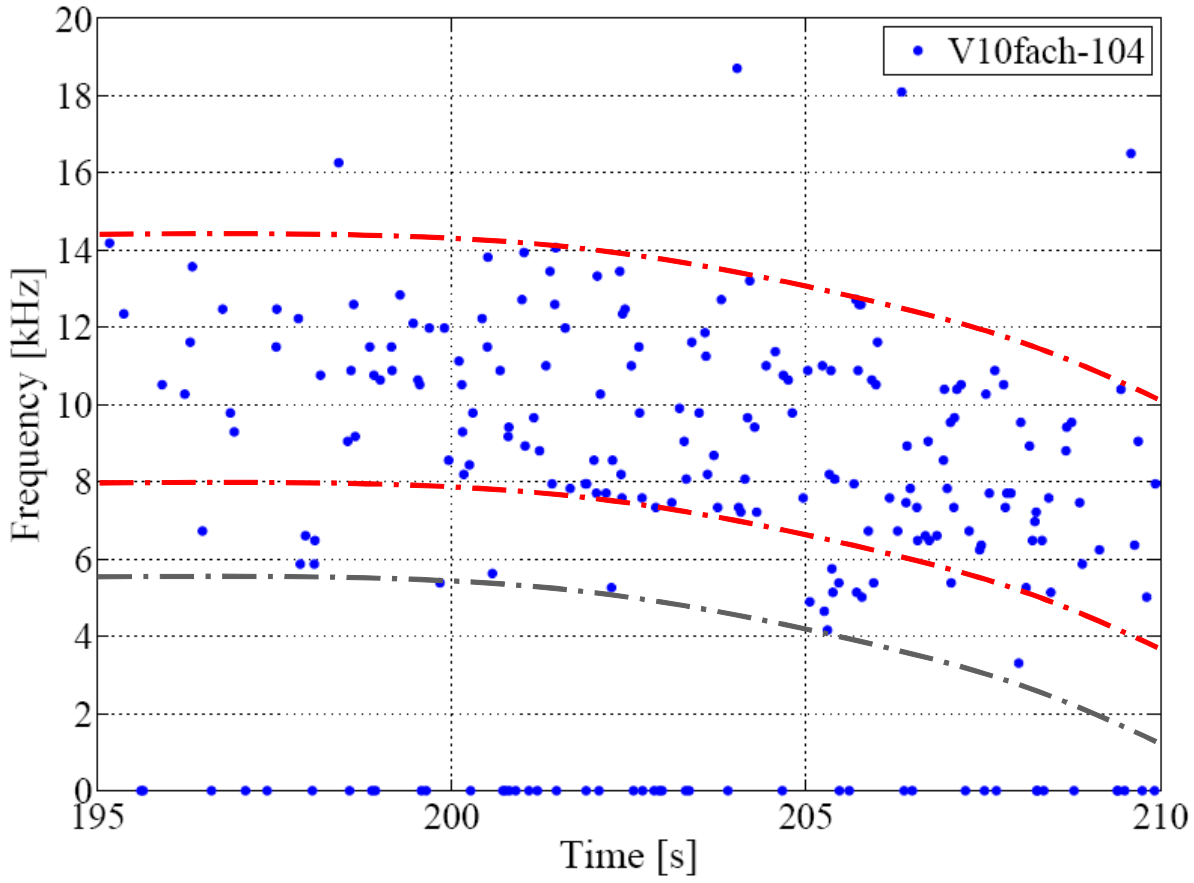

Fig. 5-17: Frequencies with amplitudes > 0.1 in the postfailure phase

The decrease of the lowest frequency peak in the postfailure phase is depicted in Fig. 5-17. Analogous to Fig. 5-12, the first frequency peak of each signal that exceeds an amplitude of 0.1 is indicated as blue dots in the plot. The dots of the frequency peaks with f = 0 kHz did not exceed the threshold of 0.1 in the signal spectra and, therefore, the 'real' frequency of these spectra is not depicted in Fig. 5-17. The dot-dash lines indicate the temporal course of the frequency range in the phase of postfailure. The red lines limit the main range of frequencies with amplitudes of > 0.1 at 8 kHz and 14 kHz in the beginning of phase (iv) and

decrease to 4 kHz and 10 kHz until the end of the postfailure phase. The grey dot-dash line indicates a lower boundary to mark frequencies that occasionally fall under the lower red line. Hence, the decrease of the lowest frequency with progressing time and the limited range of frequency in the phase of postfailure are shown illustratively.

5.3.4 Further Test Series and their Phases of Prefailure

The test series, mentioned in section 5.1, are analysed by regarding the frequencies at their maximum amplitudes in the phase of prefailure. In this analysis, the frequencies of the maximum amplitudes are taken to have a closer look to the frequency components (low and high) and to the course of the lowest frequency peaks.

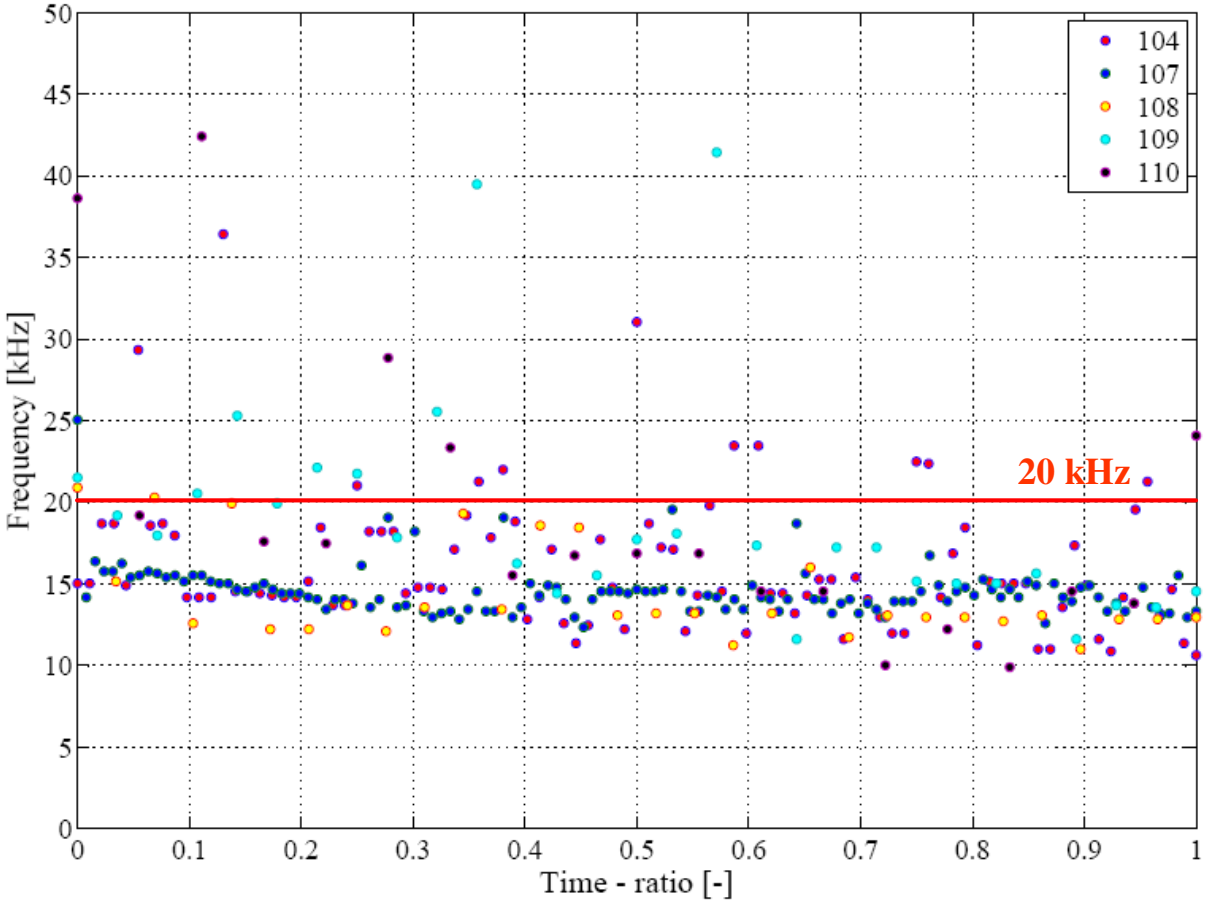

Fig. 5-18: Frequencies of maximum amplitudes with a gain factor of 10

Fig. 5-18 depicts five test series with a path-controlled velocity of 0.5 mm/min and a factor of gain of 10. The colour dots indicate the frequencies at the maximum amplitude of the signal spectra of each test series. To compare the different times of the phase of prefailure (see Table 5.2), the length of phase (iii)

is set to 1 s. So, the phases of prefailure start at time-ratio ‘0’ (the beginning of phase (iii)) and end at ‘1’ which corresponds to the maximum compressive strengths of each test series. The red line indicates the boundary of f = 20 kHz between low and high frequency components.

The signal spectra of the test series contain in the beginning of the prefailure phase both high and low frequency components depending on the maximum amplitudes of their signal spectrum. The high frequency components decrease with progressing time. At the end of phase (iii), the frequencies of the maximum amplitudes are at the low components (< 20 kHz). Regarding the course of the low frequency components with progressing time, there is also a decrease from 15 kHz to 10 kHz. Both phenomenon are already described and analysed in section 5.3.2.

The test series with a path-controlled velocity of v = 0.2 mm/min and an amplification factor of 100 are depicted in Fig. 5-19. The frequencies that are indicated as colour dots have the highest amplitudes within their signal spectra. The boundary of high and low frequency components is plotted as red line at 20 kHz.

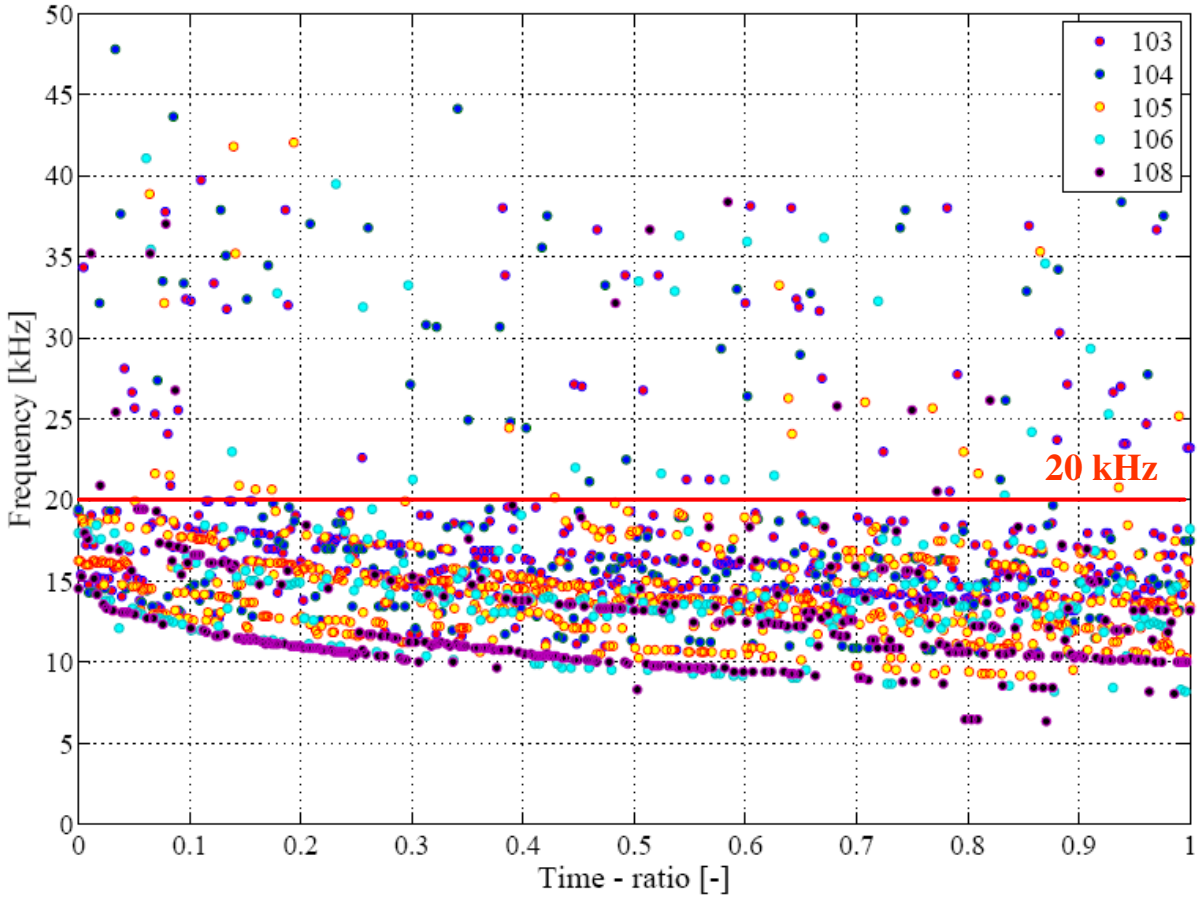

Fig. 5-19: Frequencies of maximum amplitudes with a gain factor of 100

In the test series with lower path-controlled velocity and greater amplification, the number of microacoustic emissions increases. Mainly, since the higher amplification registers even smaller events. The signal spectra contain both high and low frequency components. In the beginning of phase (iii), there are components up to 50 kHz. The number of high frequency components slightly decreases with progressing time. The highest frequency components at the end of the prefailure phase are still at approx. 37 kHz. Here is a difference to the tenfold amplification where the high frequency components are nearly disappeared at the end of phase (iii) (see Fig. 5-18). Apart from that, most of the frequency components with the highest amplitudes of the spectra are at the low frequencies (< 20 kHz).

In Fig. 5-19, there is also a decrease of the frequency peaks with the highest amplitudes but the course differs from the one with the tenfold amplification. The frequencies also begin at 15 kHz but they decrease faster to 8 kHz and 10 kHz.

The test series with the different settings have in common that the signal spectra at the beginning of the prefailure phase contain both high and low frequency components with a decrease of the high components to the end of phase (iii). The decrease of the frequency peaks with the maximum amplitudes of the spectra behaves similar but the test series with the higher amplification show a faster decrease. The explanation of the different behaviour can be the higher amplification of the signal which implies a larger number of microacoustic events and a slightly different kind of microacoustic emissions. With the higher amplification, microacoustic events are registered which would be missed by a lower gain factor. Therefore, the events are slightly different and behave in a different way.

Apart from the differences owing to amplification, it can be concluded that the signal spectra in the prefailure phases give information about the energy content of the fracture processes inside the specimen – independently on the amplification of the signal.

5.4 Key Results

In the preceding sections, the microacoustic emissions which occur during a uniaxial compressional test were analysed with regard to their intensities, to their signal spectra and to their frequency behaviour with progressing time. Regarding the shapes of the stress-time curves, the laboratory tests can be divided in four different phases. These are phase (i) in which there is a concave curve owing to not parallel end faces of the specimen or a volume decrease resulting from closure of pre-existing microcracks, respectively. Phase (ii) describes the linear elastic phase where the pores of the calcareous sandstone are deformed and crushed. In the phase of prefailure (phase (iii)), grain boundaries are breaking up and microcracks increase, interact and coalesce. In the last phase of postfailure, there is a progressive rise of cracks and, finally, the sample fails macroscopically.

The acceleration signal is then laid on the stress-time curve and the phases are applied to the acceleration signal. Beginning with phase (i), there are only a few events and the amplitudes of accelerations are low ($a < 10$ m/s²). In phase (ii), the linear elastic phase, the amount of events and the amplitudes of the accelerations are slightly increasing. The events are evenly distributed in this phase. The phase of prefailure is characterized by higher amplitudes of the

accelerations and by an increase of events towards the end of the phase. In the last phase, the amplitudes of accelerations are the highest and there is an accumulation of events. The macroscopic failure is approaching. Another examined aspect is the threshold value of the acceleration signal which is chosen to cut the single events out of the signal. It turned out that the threshold value should be set at a value of $a = 2$ m/s² to get the maximum information out of the signal. If the threshold value is chosen at a higher level, important information of the events are lost because a large number of events has its accelerations between 2 m/s² and 3 m/s². The consideration of the amplitudes of accelerations and the incidence of the events gives first remarks to characterize the different phases of the laboratory tests.

The analysis of the acceleration signal with a FFT algorithm gives information about the occurring frequencies and their amplitudes in the frequency domain. In the consideration of the signal spectra, phase (i) is neglected because the phase of prefailure interests the most and, therefore, only the bordering phases – the linear elastic and the postfailure phases – are analysed. The signal spectra in the linear elastic phase contain both the low ($f < 20$ kHz) and high ($f > 20$ kHz) frequency components. The main feature of the lower frequency components is that they do not fall below the characteristic value of about 15 kHz. Entering the phase of prefailure, the significant distinction to the prior phase is the peak value of the lowest frequency component which is constantly decreasing in time. The lowest frequency component reaches towards the end of the prefailure phase a value of about 10 kHz and rests at this value for a while. Another characteristic is the decrease of the high frequency components. The low frequency components have greater amplitudes than the high frequency components and, therefore, determine the character of the spectra. The fourth phase of the laboratory test (iv) displays the phase of postfailure. In this phase, the amount of events is rapidly increasing. The signal spectra mainly contain only low frequency components, the high frequency components only reach very small amplitudes. The peak of the low frequency components continuously decreases and tears between a value of 6 kHz and 8 kHz.

In conclusion, the most significant characteristic is the decrease of the peak of the lowest frequency component. In the linear elastic phase, there is a constant peak value of the lowest frequency. A linear decrease of the lowest frequency component occurs in the prefailure and in the postfailure phase, there is a further

decrease of the peak value. But what is the explanation for the specific behaviour during the different phases?

As mentioned before, the cut out signal of a microacoustic event gives information about the kind of microfracturing or the source event inside the sample, respectively. According to MANTHEI et al. (1993), the signal spectra with higher frequency components are generated, i.e., by the closure of pores or by the enlargement of single microcracks, whereas the spectra containing lower frequencies have higher energetic processes like interaction and coalescence of microcracks.

The relationship between the energy content of a microacoustic event and its frequencies can be applied to the results of the laboratory tests, especially in considering the signal spectra. A classification of low or high energetic events by means of the frequencies is possible and can be applied to the signal spectra.

Regarding again the linear elastic phase, there are both low and high frequency components in the signals. Hence, there are microacoustic emissions with high and low energetic events with different fracture mechanisms as sources of the microacoustic event. The low energetic events, i.e., the high frequency components in the signal spectrum, signify a small event such as collapsing pores due to stress concentrations (compare Section 5.1). The high energetic events, i.e., the low frequency components in the signal spectrum, have their origins in greater events such as the growth of microcracks. In phase (ii), the registered microacoustic events contain both high and low energetic events and, therefore, different types of microacoustic emissions with differing trigger events.

Within the following phase of prefailure, the occurrence of low and high energetic events is changing. In the beginning (compare Fig. 5-9), there are still components of high and low frequencies, hence, the microfracture mechanisms are comparable to the linear elastic phase. The signal spectra contain both high and low frequency components. But with progressing time, the amount of high frequency components is decreasing. Hence, there is a change in the fracture mechanisms during the loading inside the sample. The low energetic events are decreasing, i.e., the pores inside the sample completely collapsed and the only compressible elements that remain are the grains of the porous rock (compare

Section 5.1). Then, these grains are still compressed and another type of trigger event results from the compressive loading. These trigger events probably result from microcrack growth and a unification of two or more microcracks to one single or new one. Hence, the microacoustic emissions contain greater energy content and, therefore, the frequency components are decreasing to a lower value. There are still occasionally high frequency components but they are not the predominant frequencies of the signal spectra in the prefailure phase. Having a closer look at the lower frequency components in the phase of prefailure, it is detected that the value of the lowest frequency peak is decreasing with time. The relationship between the energy content and the frequency component gives the conclusion that the microfracture mechanisms now contain greater energy content. Several microcracks merge to a new one. With the unification of several microcracks and the breaking up of grain boundaries, the macroscopic failure is approaching.

In the phase of postfailure, the increasing load leads to a progressive rise of cracks and finally to the failure of the sample. The signal spectra of the microacoustic emissions mainly contain low frequency components, i.e., the microfracture mechanisms have higher energy contents compared to the prior load steps. High frequency components are almost vanished and, hence, the phase of postfailure is characterized by events of great fracture processes. That is the progressive microcrack propagation with concomitant union of microcracks. The energy of the microacoustic events increases and, therefore, the frequency component decreases until the sample macroscopically fails.

In conclusion, the frequency components of the signal spectra give information about the energy content of microacoustic event that occurred inside the sample, although the microfracture mechanism cannot be precisely determined. But the consideration of the frequency components of the signal spectra allows a classification to the different phases of the laboratory test and, hence, recorded signals and their spectra can be assigned to the phases of the laboratory test.

6 Summary and Outlook

Rockbursts occur in mining areas throughout the world. A rockburst is the significant damage caused to underground excavations by a seismic event which is considered to be the transient energy released by a sudden fracture or failure in the rockmass. A seismic event results in the emission of a seismic vibration transmitted through the rock. The recording of these seismic vibrations gives information about the cause of the event. Previous test series and investigations in the laboratory and in situ mainly concerned the intensities and incidences of occurring events. But there was a lack of experiences about the occurring frequencies in the phases of load application, especially in the phase of prefailure. In the present research work, specimens of calcareous sandstone are uniaxially loaded in the laboratory and the acoustic emissions are recorded and analysed considering the intensities, the incidences and the frequency behaviour of the microacoustic events.

The consideration of the frequency behaviour of microacoustic events during loading was not yet investigated and, therefore, the experimental results of this research work are the first of their kind. In an extensive test program, the acoustic emissions were recorded and analysed. Different phases of load application were determined and examined regarding the intensities, incidences and, mainly, the frequencies. The most important phase was the one of prefailure in order to give specific indicators for the occurring macroscopic failure of the specimen.

In the laboratory test series, it was observed that the amplitudes of accelerations and the incidence of the microacoustic events increased in the course of the compressional test. Furthermore, there was a change in the frequency behaviour of the microacoustic emissions. Whereas in the linear elastic phase, the lowest frequency peaks of the signal spectra had a nearly constant value of f = 15 kHz,

the phase of prefailure was characterized by a decrease of the lowest frequency peaks to f = 10 kHz. A further decrease of the lowest frequency peaks occurred in the phase of postfailure. The decrease of the lowest frequency peaks was the most significant characteristic of the test series done in the laboratory and gave the conclusion that the microfracture mechanisms contained greater energies with progressive load application. Thus, the microcracks grew, interacted and coalesced and, therefore, the energy content of the fracture processes changed due to loading. The growth, the interacting and the coalescence of microcracks resulted in greater fracture processes and, therefore, in an increase of the energy contents of the recorded events. This increase of energy content was detectable in the decrease of the frequency peaks, mainly in the phase of prefailure with a decrease from 15 kHz at the beginning to 10 kHz at the end of this phase.

In conclusion, the frequency components of the signal spectra give information about the energy content of a microacoustic event that occurred inside the sample. Thus, the consideration of the frequency components of its signal spectra allows an assignment to the different phases of the laboratory test. Hence, recorded signals and their spectra can be assigned to their state of fracture and their state of loading by investigating the frequencies of the microacoustic events.

Within the present research work, specific indicators were found for the material of calcareous sandstone to identify – on the basis of the frequencies of microacoustic emissions – the present state of fracture and loading. With these first investigations at artificial materials, an application to natural materials (e.g. granite and rock salt) and in situ stresses has to be carried out in future research works.

Further test set-ups have to be done to apply the results of the laboratory test to in situ conditions. A change in the system of loading, i.e., the unloading and reloading of the sample would represent the in situ stress situation more precisely (e.g. loading: tunnel driving, unloading: relaxation after stress redistribution). To adapt the in situ stress even more, the sample of calcareous sandstone should be dynamically loaded by the press (e.g. loading by a tunnelling machine). A combination of both loading and unloading and dynamical loading could be a further test set-up. With these various types of loading, the intensities and frequency behaviour of the microacoustic events can

be further investigated and the knowledge about the behaviour of occurring acoustic emissions increases.

In addition, the laboratory tests should be done with different materials, e.g., rock salt or granite. Rock salt is characterized by different rock fabric and mechanical behaviour and, therefore, the microfracture mechanisms are changing and the microacoustic emissions contain a varying band of frequencies. It is the same for granite, although granite has an almost brittle material behaviour, the fabric is different compared to calcareous sandstone and, hence, the range of frequency will vary, too. With different ranges, other types of sensors are required that cover various frequency ranges. Concluding, the tests with differing materials will give material specific information for each rock fabric.

With the results of the different loading systems and the various materials, an application to in situ should be possible. Presently, for example, there are measurements in salt mines where microacoustic activity is registered regarding intensity and rate of occurrence of microacoustic emissions (see Chapter 2.5.3.3). The specific frequencies investigated by laboratory tests could competently replenish the present monitoring of mines in order to predict the approaching fracture processes of rock. Apart from that, there is the necessity to adapt the measurement chain to a greater area of monitoring and changing frequency ranges.

In conclusion, the research work presents first investigations regarding the frequency behaviour of microacoustic events of calcareous sandstone during uniaxial compressional test series. The state of fracture and loading of a material can be determined by the analysis of the frequencies of the occurring microacoustic events and, therefore, the present work serves as a basis for further research works with natural materials and varying stress conditions.

Appendix A

Signal Spectra

A.1 Signal Spectra – Linear Elastic Part (ii)

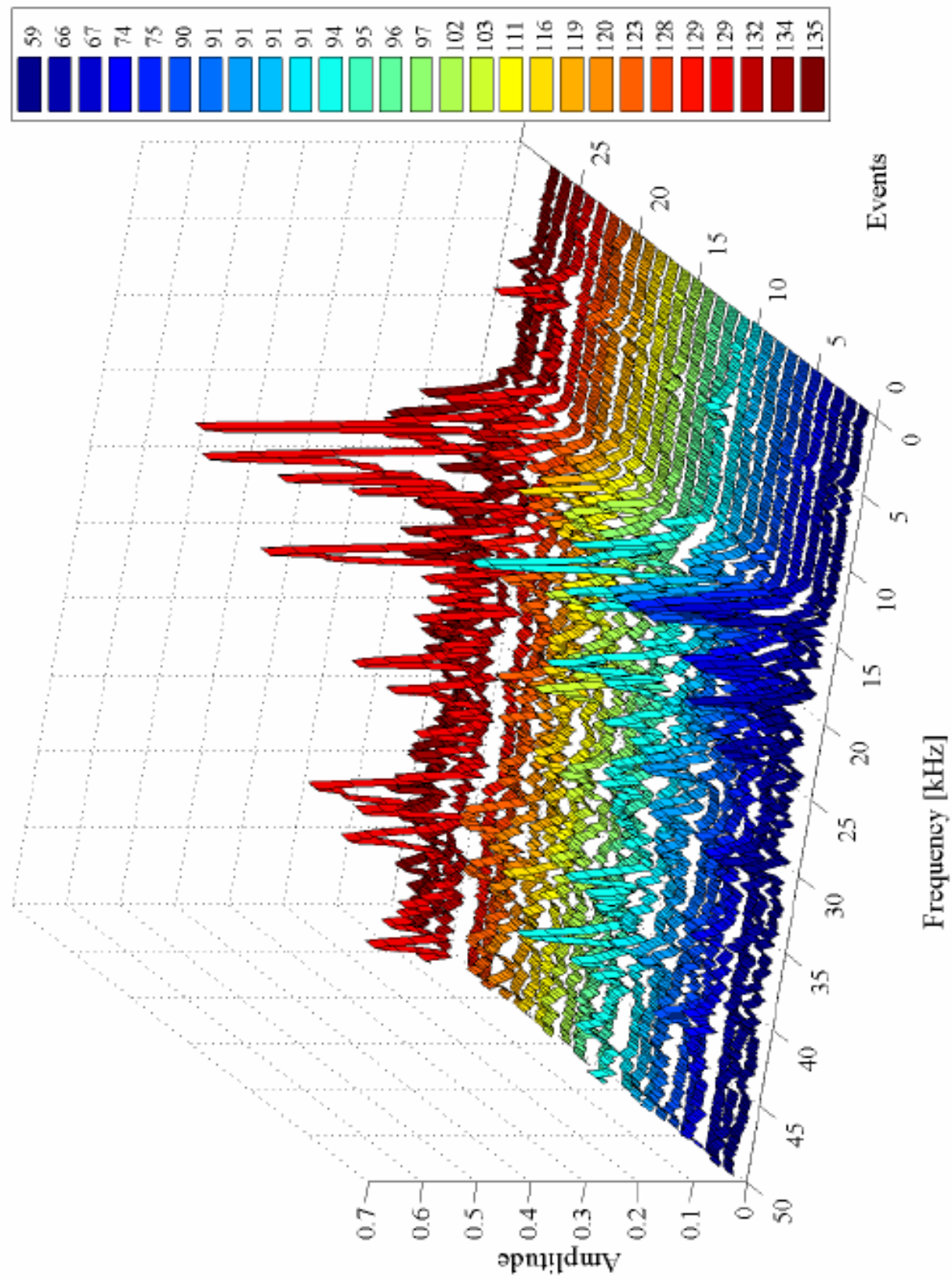

Fig. A.1: Signal spectra of linear elastic phase

A.2 Signal Spectra – Part of Prefailure (iii)

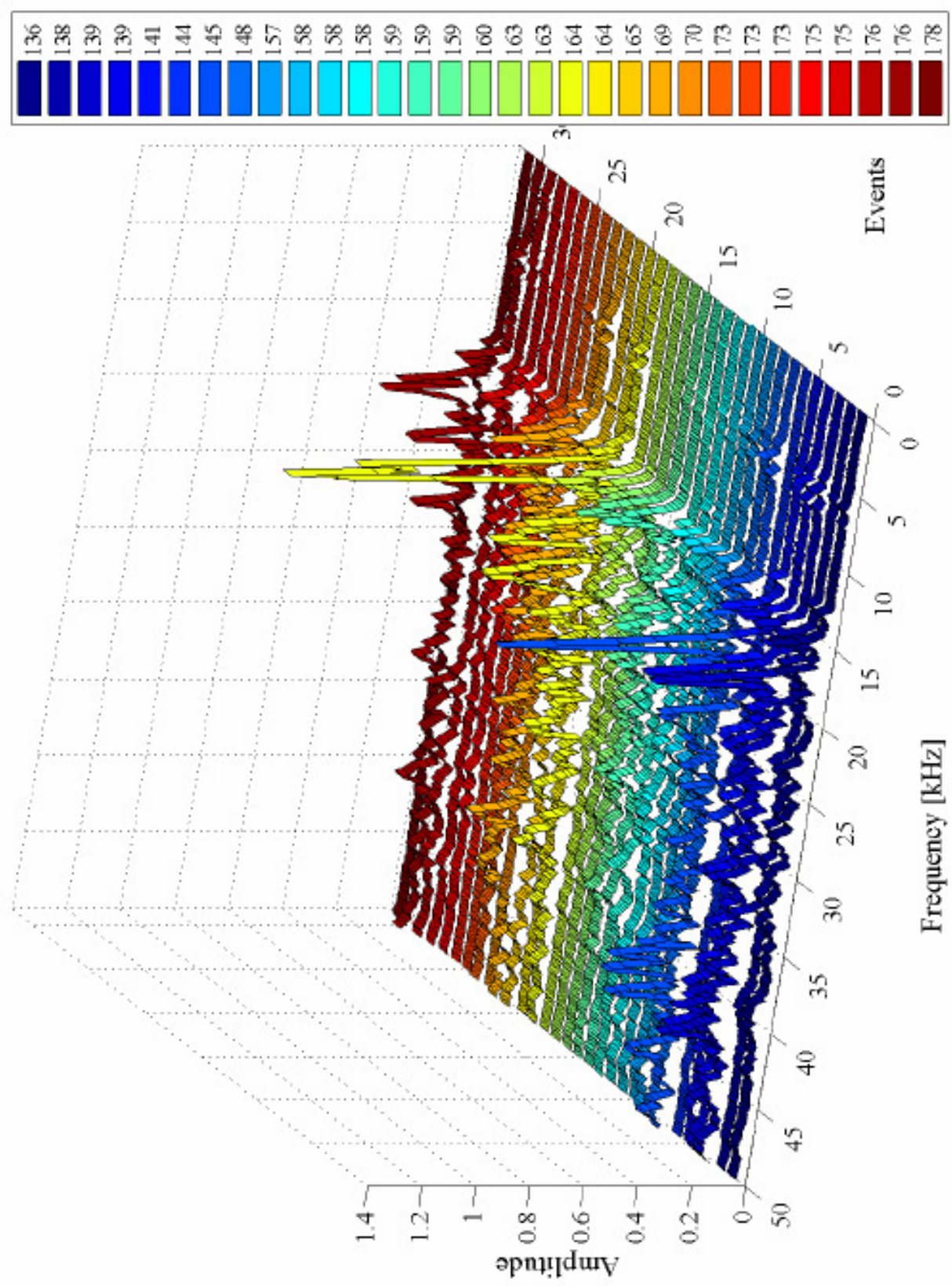

Fig. A.2: Signal spectra of phase of prefailure – time steps from 136 s to 178 s

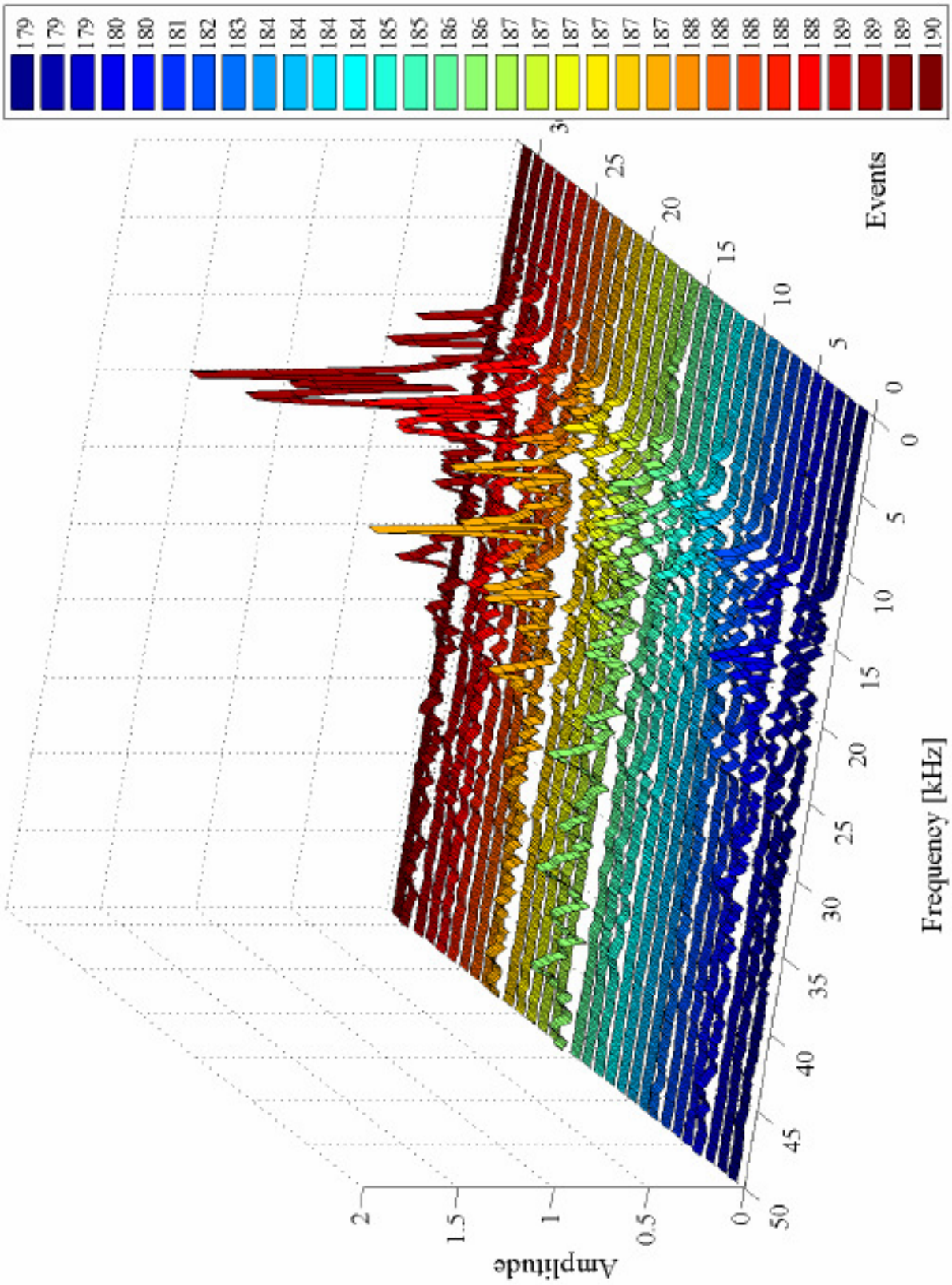

Fig. A.3: Signal spectra of phase of prefailure – time steps from 179 s to 190 s

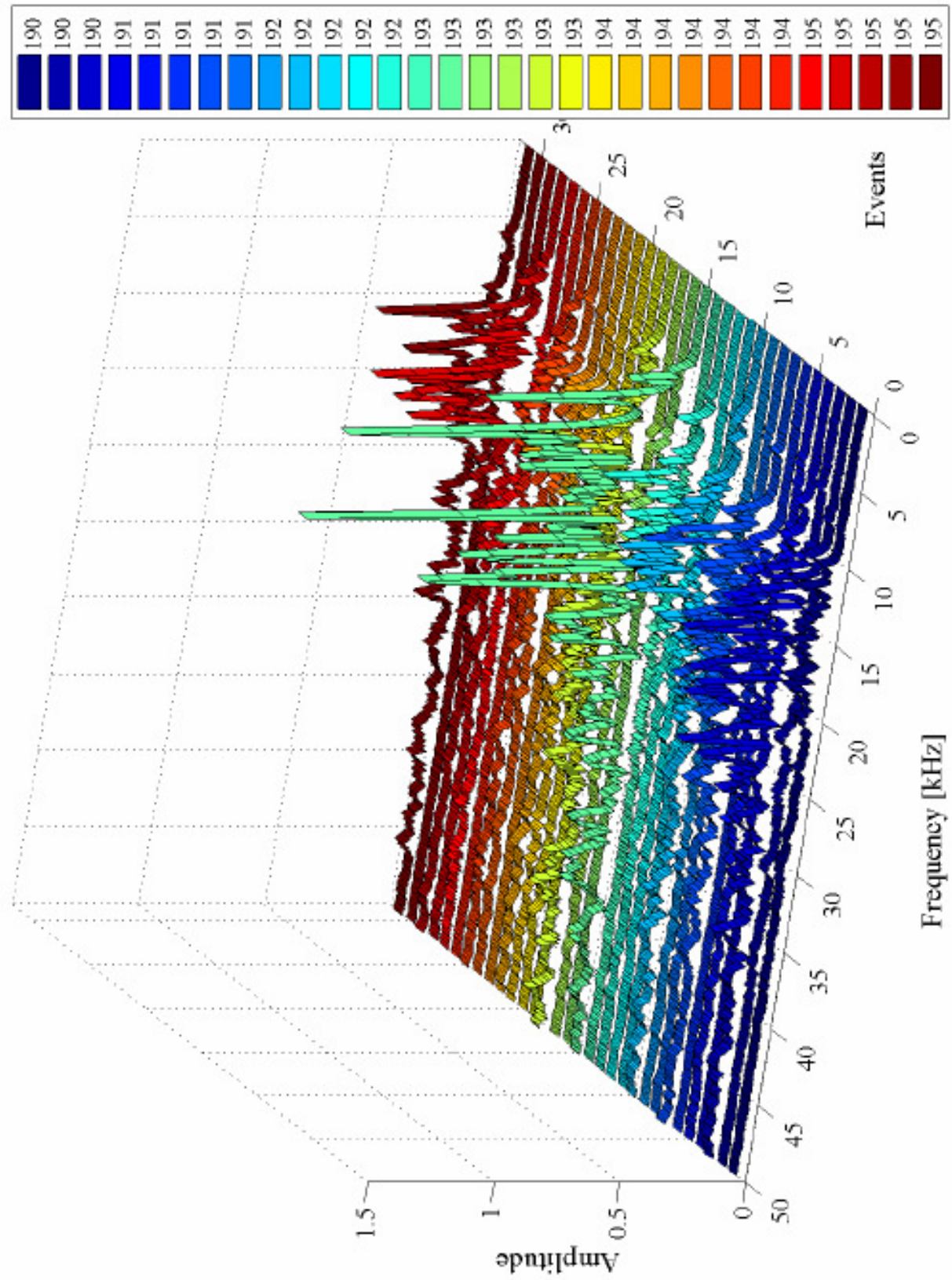

Fig. A.4: Signal spectra of phase of prefailure – time steps from 190 s to 195 s

A.3 Signal Spectra – Part of Postfailure (iv)

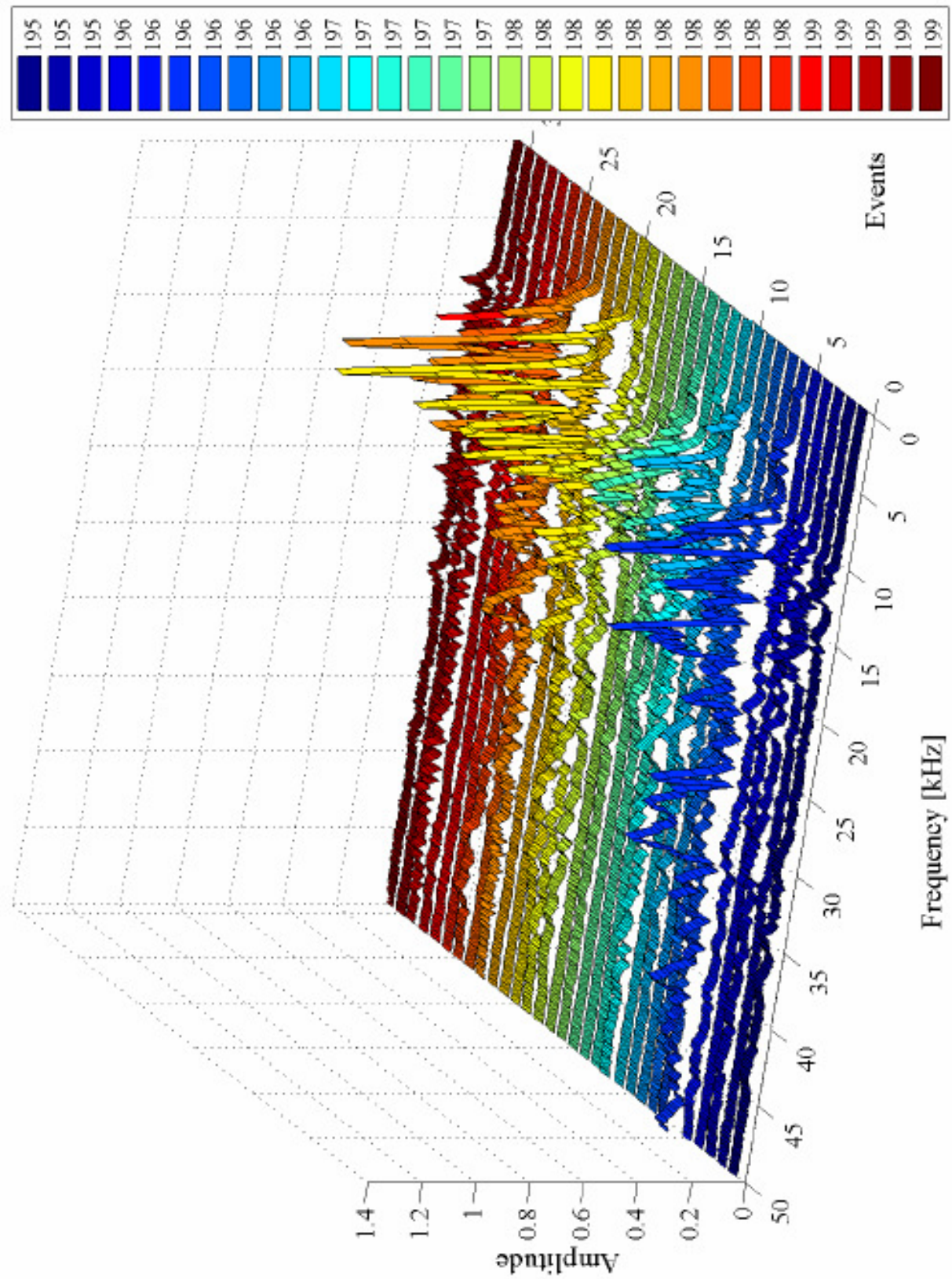

Fig. A.5: Signal spectra of phase of postfailure – time steps from 195 s to 199 s

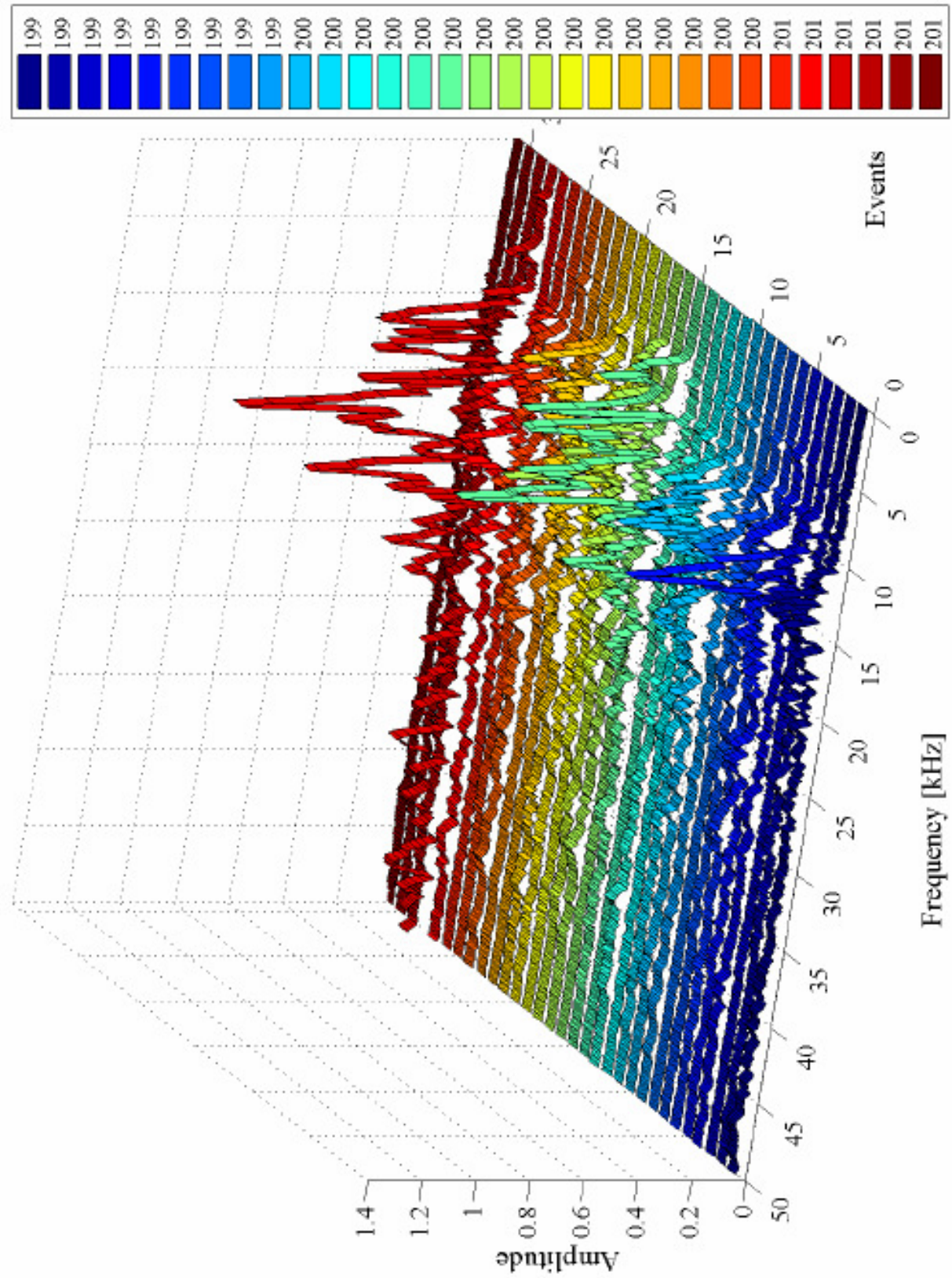

Fig. A.6: Signal spectra of phase of postfailure – time steps from 199 s to 201 s

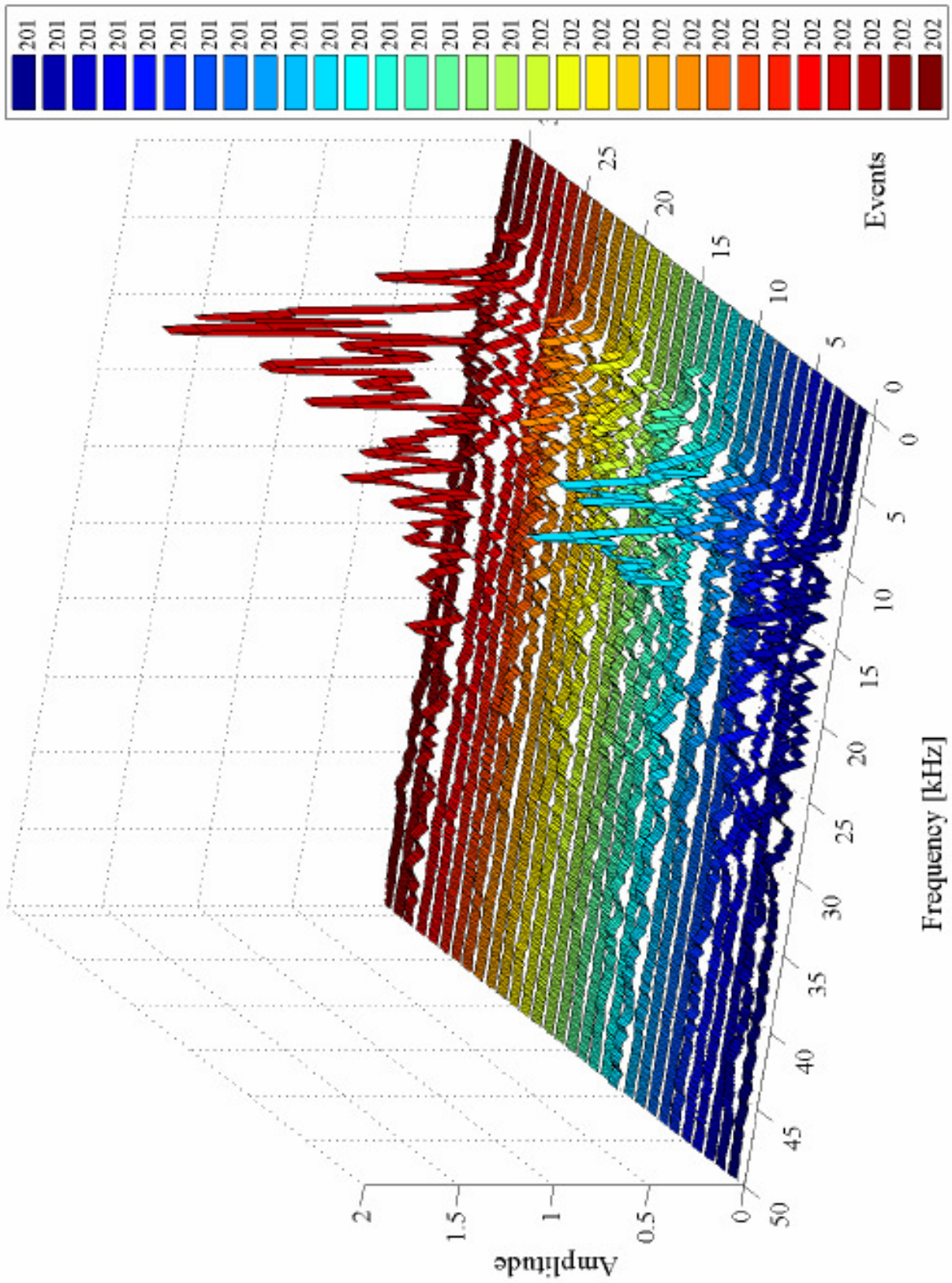

Fig. A.7: Signal spectra of phase of postfailure – time steps from 201 s to 202 s

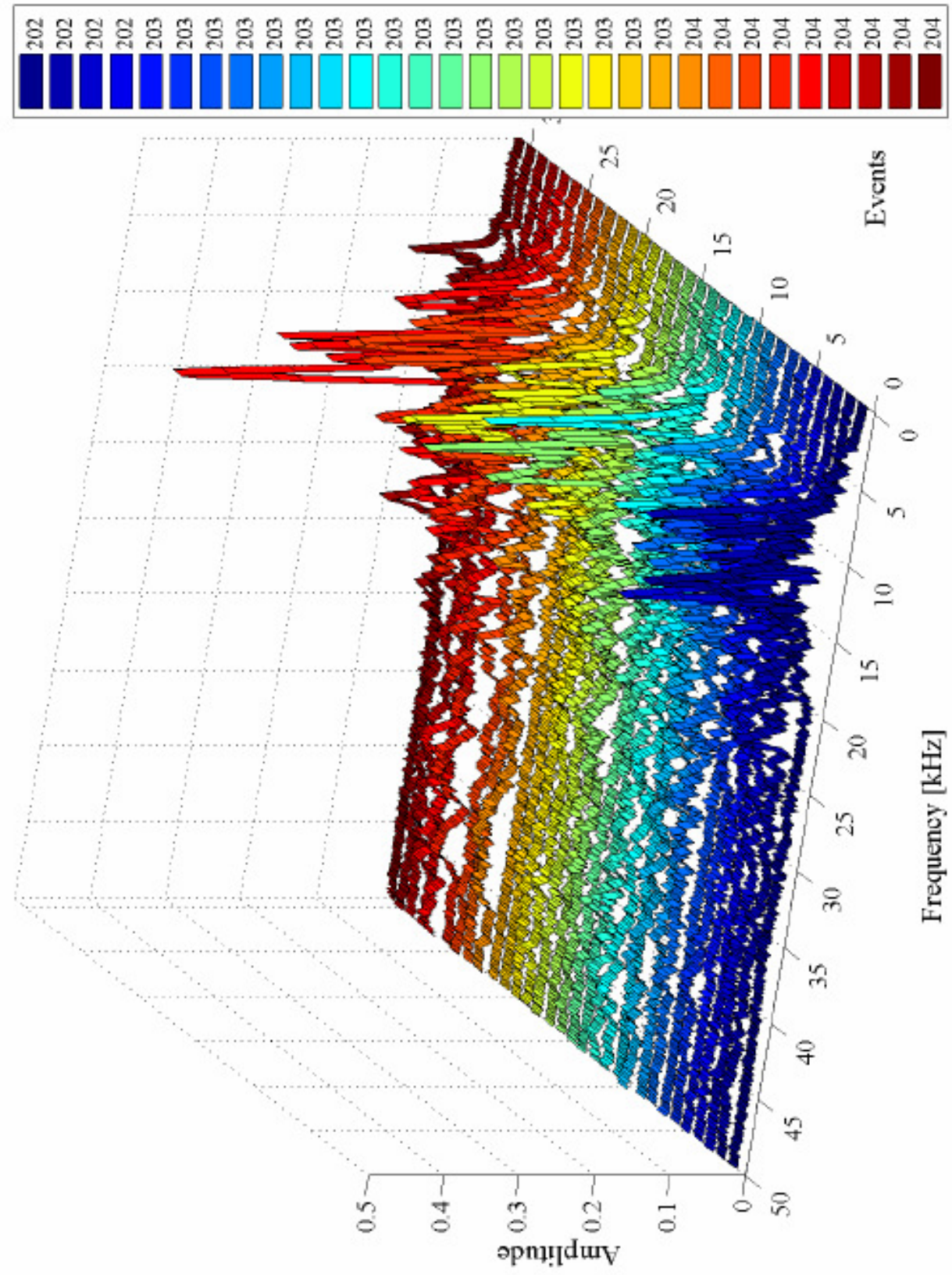

Fig. A.8: Signal spectra of phase of postfailure – time steps from 202 s to 204 s

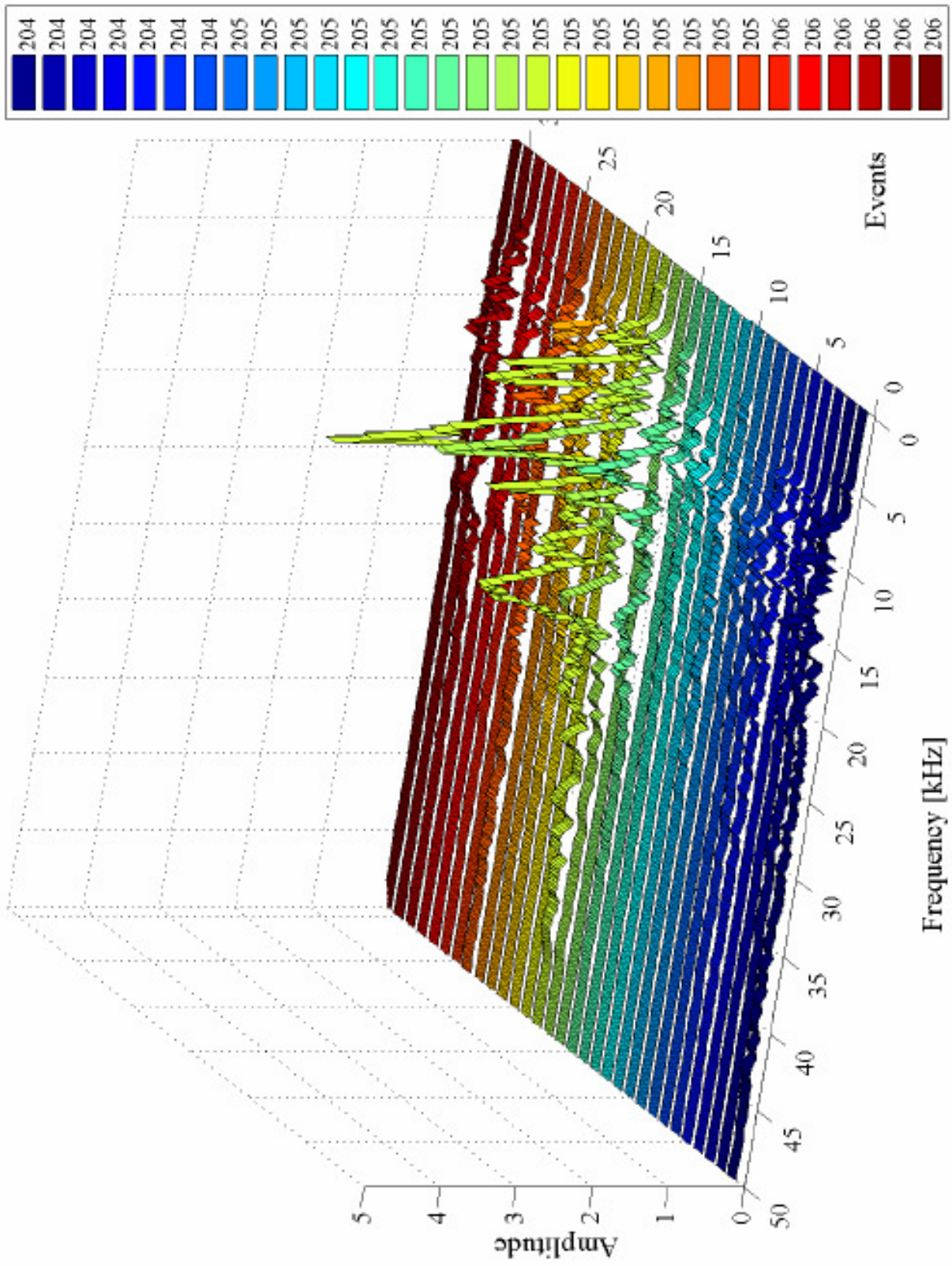

Fig. A.9: Signal spectra of phase of postfailure – time steps from 204 s to 206 s

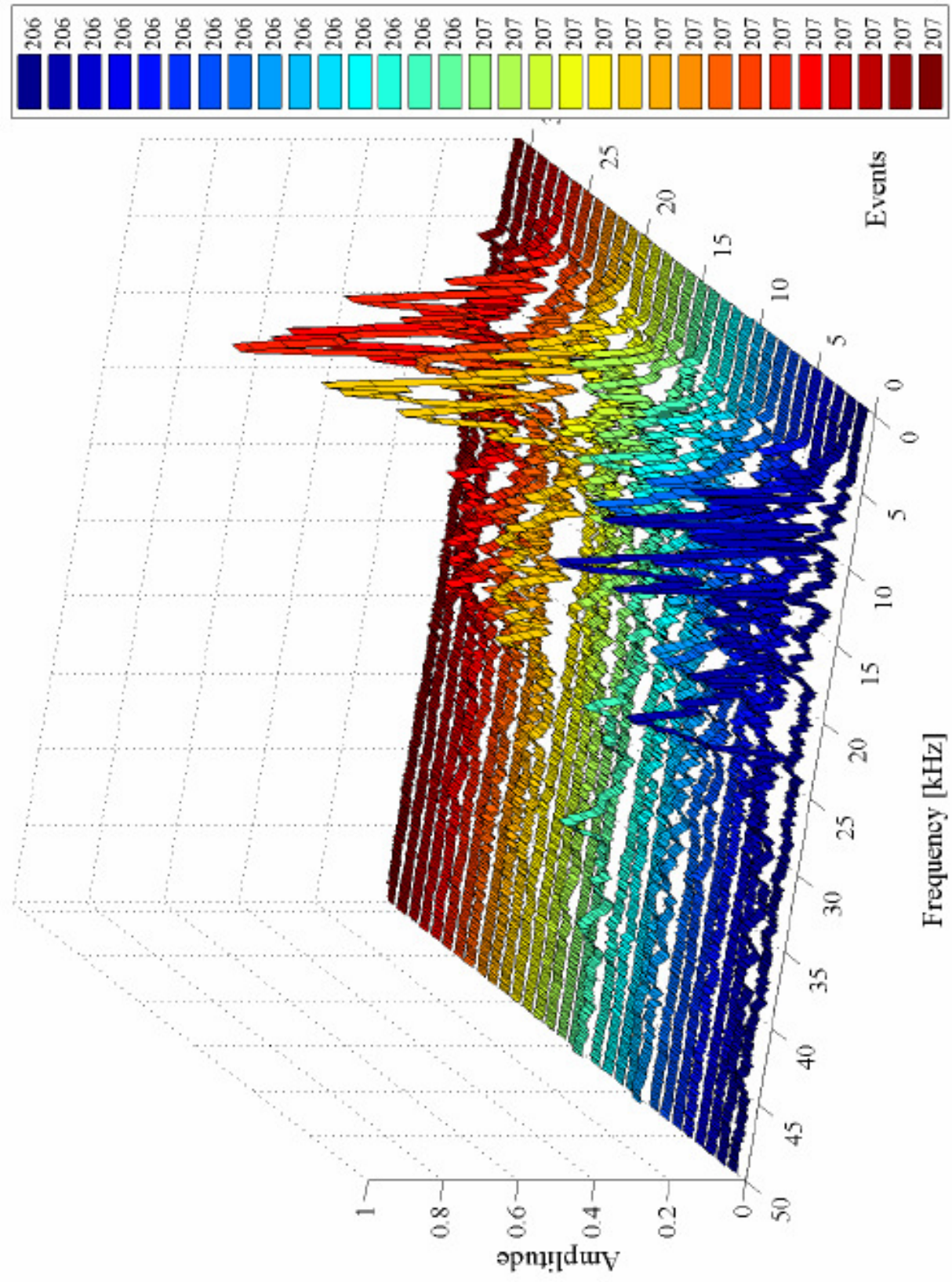

Fig. A.10: Signal spectra of phase of postfailure – time steps from 206 s to 207 s

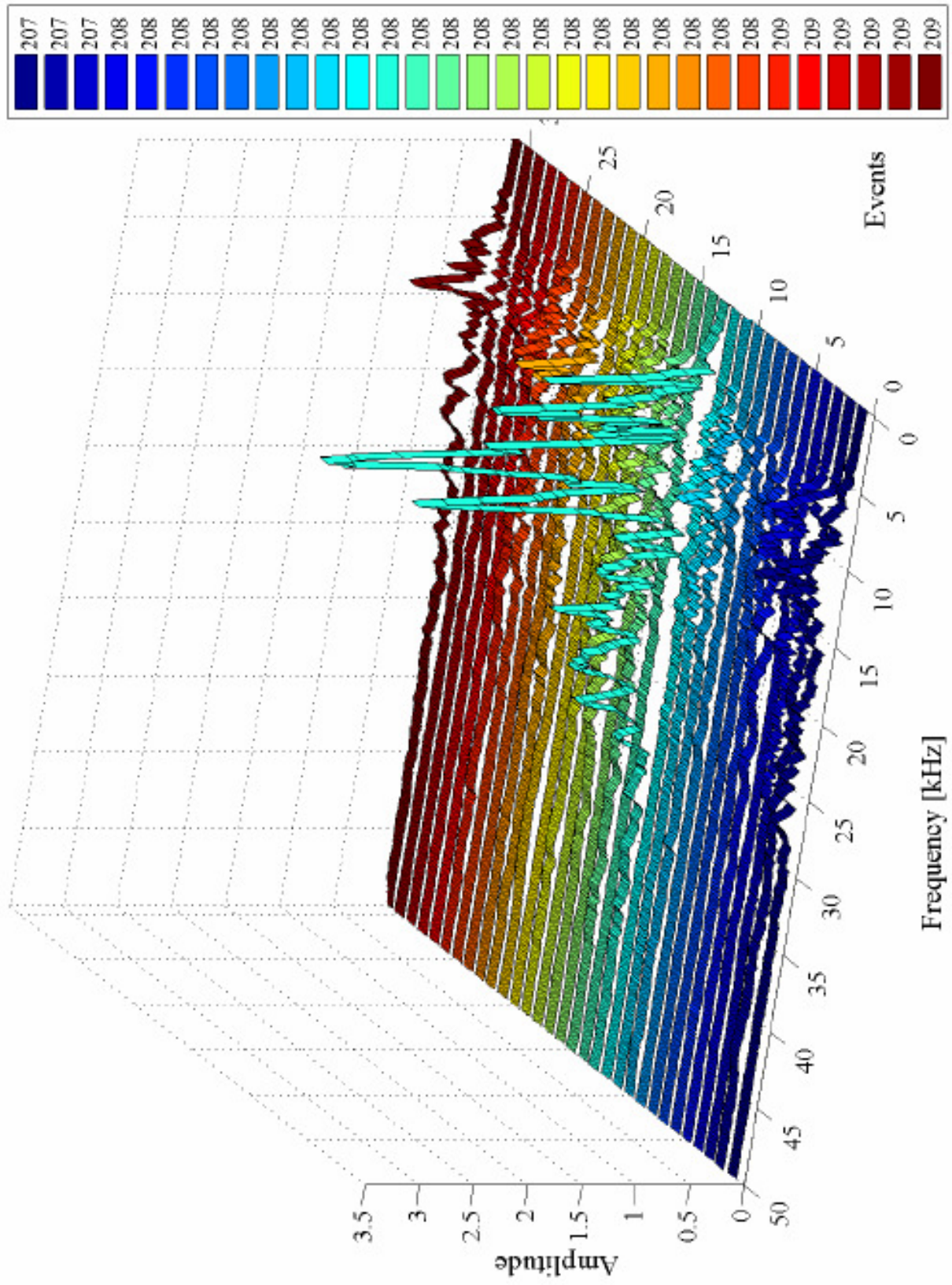

Fig. A.11: Signal spectra of phase of postfailure – time steps from 207 s to 209 s

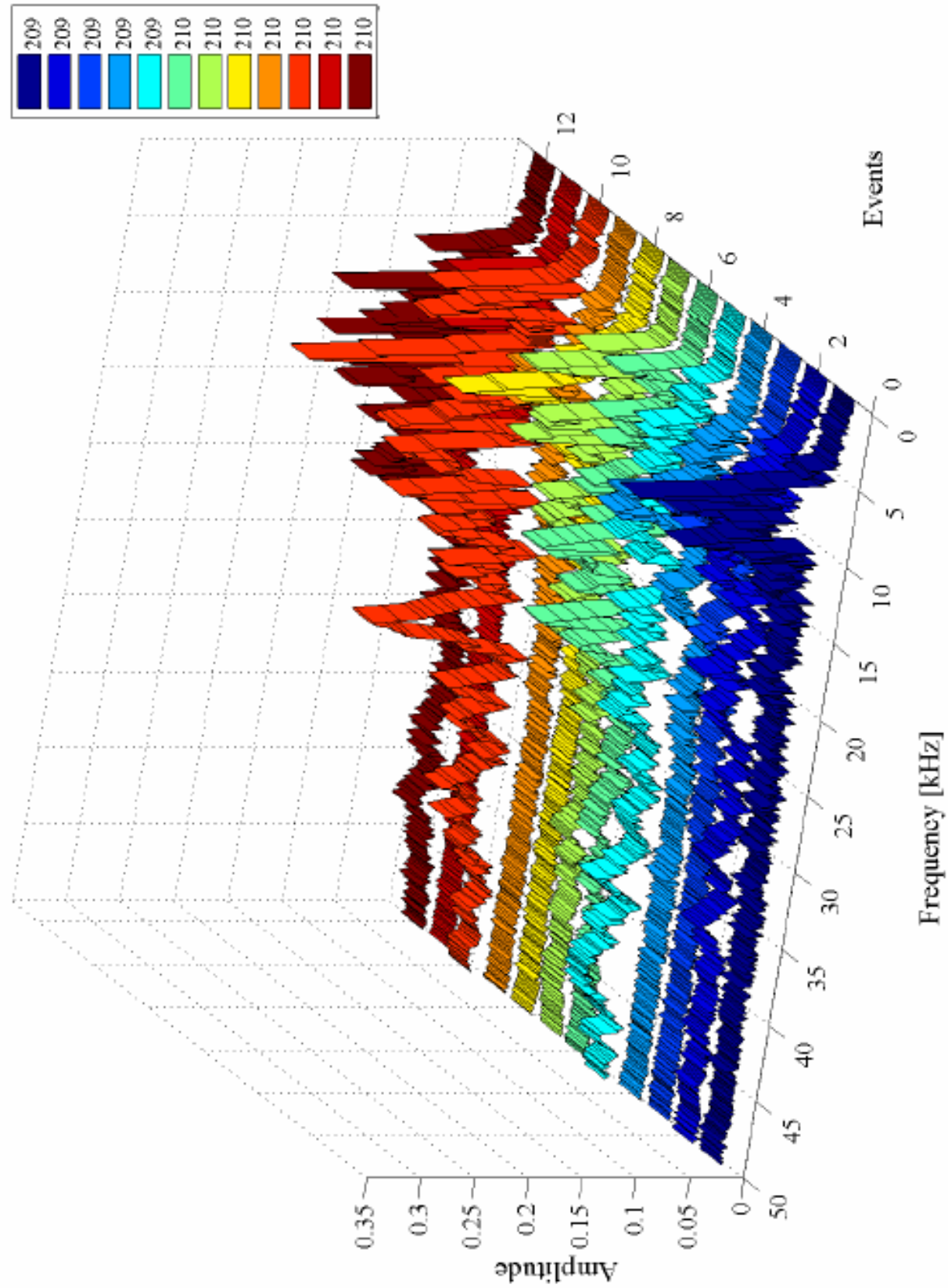

Fig. A.12: Signal spectra of phase of postfailure – time steps from 209 s to 210 s

Nomenclature

Abbreviations in Chapter 2 'Rockbursts, Fracture Mechanisms and AE'

a, b	Constants
b-value	b-value of Gutenberg-Richter
c, d	Semi-axes
c'	Cohesion
d_m	Distance between receiver m and AE location
E	Young's modulus
I_{local}	Intensity at a certain location
I_0	Epicentral intensity
M	Seismic magnitude
M_L	Local magnitude
N	Number of earthquakes
n	Number of sensors
P	Pore pressure
R	Distance from hypocentre
z	Focal depth
U	Total energy
U_e	Change of internal strain energy
U_f	Friction energy

U_k	Kinetic energy
U_s	Surface energy
V_P, V_{P0}	P-wave velocities
V_S, V_{S0}	S-wave velocities
W	Work of external forces
W_i	Waveform amplitude
W_{RMS}	'Root mean square' waveform amplitude
α	Attenuation coefficient
β	Shape parameter
γ	Specific surface energy
$\varepsilon_1, \varepsilon_2, \varepsilon_3$	Crack density parameter
$\Phi(V)$	Event amplitude distribution
λ	Separation parameter
μ	Coefficient of friction
σ_n	Normal stress
σ_t	Theoretical strength
σ_1	Maximal principal stress
σ_∞	Uniform tensile stress
τ	Shear stress

Abbreviations in Chapter 4 'Data Acquisition and Data Processing'

f	Frequency
f_c	Nyquist critical frequency
H	Function of frequency
h	Function of time
h_n	Samples
T	Interval of time
Δt	Time step (duration)

t	Time step (number)
δ_p	Design parameter for passband
δ_s	Design parameter for stopband
Δ	Sampling interval
Ω_{pH}	Upper passband cutoff frequency
Ω_{pL}	Lower passband cutoff frequency
Ω_{sH}	Upper stopband cutoff frequency
Ω_{sL}	Lower stopband cutoff frequency

Abbreviations in Chapter 5 ‘Analysis and Results of the Test Series’

a	Amplitude of acceleration
f	Frequency
$\sigma_{\max}$	Maximum compressive strength
$t(\sigma_{\max})$	Time of failure
v	Loading velocity

References

Ahorner, L.	1998	Entstehung und Ablauf des Gebirgsschlages von Völkershausen am 13. März 1989 im Kalibergbaugebiet des Werratals, Thüringen, aus seismologischer Sicht; Geol. Jahrbuch, Reihe E, Hannover
Aki, K., Lee, W. H. K.	2003	Glossary of Interest to Earthquakes and Engineering Seismologist; Appendix 1 in International Handbook of Earthquake and Engineering Seismology, Part B (eds. W.H.K. Lee, H. Kanamori, P.C. Jennings, C. Kisslinger), Academic Press, London, San Diego, Burlington, 1793-1856
Ayling, M.R.	1991	An Experimental Study of Physical Property Changes in Crustal Rocks Undergoing Triaxial Deformation; Ph.D. Thesis, University of London.
Ayling, M. R., Meredith, P. G., Murrell, S. A. F.	1994	Microcracking during Triaxial Deformation of Porous Rocks Monitored by Changes in Rock Physical Properties, I. Elastic-Wave Propagation Measurements on Dry Rocks; Tectonophysics 245, pp. 205-221
Bennett, T. J., Marshall, M. E., Cook, R. W.	2000	Regional Signal Characteristics for Use in Screening Seismic Events in Rockburst Areas; 21st Seismic Research Symposium, Geophysics Group, Maxwell Technologies, Inc.
BGR	2005	Erdbeben in Deutschland 1996, Herausgeber: Bundesanstalt für Geowissenschaften und Rohstoffe

Blanpied, M. L., Lockner, A. D., Byerlee, J. D.	1991	Fault Stability Inferred from Granite Sliding Experiments at Hydrothermal Conditions, Geophys. Res. Lett. 18, 609-612
Bombolakis, E.	1964	Photoelastic Investigation of Brittle Crack Growth within a Field of Uniaxial Compression; Tectonophysics, 1, pp. 343-351
Bombolakis, E.	1968	Photoelastic Study of Initial Stages of Brittle Fracture in Compression; Tectonophysics, 6, pp. 461-473
Bombolakis, E.	1973	Study of Brittle Fracture under Uniaxial Compression; Tectonophysics, 18, pp. 231-248
Brace, W. F., Paulding, B. W., Scholz, C. H.	1966	Dilatancy in the Fracture of Crystalline Rocks, J. Geophys. Res. 71: 3939-3953
Cai, D., Fang Y., Sui W., Zhang L., Li J., Geng N.	1988	The b-Value of Acoustic Emission during the Complete Process of Rock Fracture; Acta Seismologica Sinica 2, 129-134
Calder, P. N., Archibald, J. F., Madsen, D., Bullock, K.	1990	High Frequency Precursor Analysis prior to a Rockburst; Rockbursts and Seismicity in Mines, (Edited by Fairhurst), pp. 177-181
Evans, A. G.	1978	Acoustic Emission Sources in Brittle Solids; In: Fundamentals of Acoustic Emission (Edited by K. Ono), pp. 209-227. Materials Dept., UCLA, Los Angeles
Friedman, M., Handin, J., Alani, G.	1972	Fracture Surface Energy of Rocks, Int. J. Rock Mech. Min. Sci., 9: 757-766
Griffith, A. A.	1920	The Phenomenon of Rupture and Flow in Solids; Phil. Trans. Roy. Soc. London, Ser. A 221, 163-198
Griffith, A. A.	1924	The Theory of Rupture; Proc. Ist. Int. Congr. Appl. Mech., eds. C. B. Biezeno and J. M. Burgers, Delft: Tech. Boekhandel en Drukkerij J. Walter Jr., 54-63
Grünthal, G.	1998	European Macroseismic Scale 1998 (EMS-98). Conseil de l'Europe, Cahiers du Centre Européen de Géodynamique et de Séismologie, Luxembourg, Volume 15

Grünthal, G., Minkley, W.	2005	Bergbauinduzierte seismische Aktivität als Quelle seismischer Belastungen; Bautechnik 82, Heft 8, S. 508-513
Gupta, H.	1992	Reservoir-Induced Earthquakes; Development in Geotechnical Engineering, 64, Elsevier
Hallbauer, D. K., Wanger, H., Cook, N. G. W.	1973	Some Observations Concerning the Microscopic and Mechanical Behaviour of Quartzite Specimens in Stiff, Triaxial Compression Tests; Int. J. Rock Mech. Min. Sci., 10, pp. 713-726
Hirata, T.	1987	Omori's Power Law Aftershock Sequences of Microfracturing in Rock Fracture Experiment; J. Geophys. Res. 92, 6215-6221
Hoek, E., Bieniawski, Z. T.	1965	Brittle Fracture Propagation in Rock under Compression; J. Fract. Mech., 1, pp. 137-155
Holcomb, D. J., Costin, L. S.	1986	Detecting Damage Surfaces in Brittle Materials Using Acoustic Emissions, J. Appl. Mech. 108, pp. 536-544
Holub, K.	1997	Predisposition of Induced Seismicity in Some Czech Coal Mines; Pure a Applied Geophysics 150, 435-450
Hoshino, K., Koide, H.	1970	Process of Deformation of the Sedimentary Rocks; Proc. 2nd Congr. Int. Soc. Rock Mech., Belgrade, Vol. 1, pp. 2-13
Husen, S., Deichmann, N., Kissling, E., Giardini, D.	2005	Locally Induced Seismicity in Switzerland, Poster (http://geoscience-meeting.scnatweb.ch/sgm2005/SGM05_abstracts/11_Natural_hazards/session_11_posters.pdf)
Imoto, M., Ishiguro M.	1986	A Bayesian Approach to the Detection of Changes in the Magnitude-Frequency Relation of Earthquakes; J. Phys. Earth 34, 441-455
Jaeger, J. C., Cook, N. G.	1976	Fundamentals of Rock Mechanics, London, Chapman and Hall
Jones, C., Murrell, S.A.F.	1989	Acoustic Compressional Wave Velocity and Dilatancy in Triaxially Stressed Rock; In: V. Maury and D. Fourmaintraux (Editors), Rock at Great Depth, Vol. I. Balkema, Rotterdam, pp. 241-249
Kappei, G.	2005	2. Fachgespräch zur Situation im Atommüll-Endlager Asse II, Überblick über das Geschehen auf der Schachanlage Asse II seit Oktober 2001

Kissling, E., Rehbock-Sander, M.	2007	Gotthard-Basistunnel – Bergschläge und Mikrobeben in der MFS Faido; Tagungsband Swiss Tunnel Congress 2007
Kövesligethy, R. von	1907	Seismischer Stärkegrad und Intensität von Beben; Gerlachs Beiträge Geophysik., VIII; Leipzig
Kranz, R. L.	1979	Crack Growth and Development during Creep of Barre Granite; Int. J. Rock Mech. Min. Sci., 16, pp. 23-35
Kranz, R. L.	1983	Microcracks in Rock – A Review, Tectonophysics 100, 449-480
Lenhardt, W. A.	1998	Erdbeben der vierten Art – Lokales seismisches Gefährdungspotential durch Eingriffe in die Natur; Bautechnik 75, Heft 10
Leydecker, G., Grünthal, G., Ahorner, L.	1998	Der Gebirgsschlag vom 13. März 1989 bei Völkershausen in Thüringen im Kalibergbaugebiet des Werratals – Makroseismische Beobachtungen und Analysen; Geolog. Jahrbuch, Reihe E, Heft 55
Liu, H. P., Livanos, A. C. R.	1976	Dilatancy and Precursory Bulging along Incipient Fracture Zones in Uniaxially Compressed Westerly Granite; J. Geophys. Res., 81, pp. 3495-3510
Lockner, D. A., Byerlee, J. D.	1977a	Acoustic Emission and Fault Formation in Rock; Pro. 1st Conf. Microseismic Activity in Geological Structures and Materials, eds. H. R. Hardy and F. W. Leigthon. Clausthal: Trand-tech Publ., pp99-107
Lockner, D. A., Byerlee, J. D.	1977b	Acoustic Emission and Creep in Rock at High Confining Pressure and Differential Stress; Bull. of the Seismological Society of Amer. 67, 247-258
Lockner, D. A., Byerlee, J. D., Kuksendo, V., Ponomarev, A., Sidorin, A.	1991	Quasi-static Fault Growth and Shear Fracture Energy in Granite; Nature 350, 39-42
Lockner, D. A., Byerlee, J. D., Kuksendo, V., Ponomarev, A., Sidorin, A.	1992	Observations of Quasistatic Fault Growth from Acoustic Emission; In: Fault Mechanics and Transport Properties of Rocks (Edited by B. Evans and T.-f. Wong), pp. 3-31. Academic Press

Lockner, D. A.	1993	The Role of Acoustic Emission in the Study of Rock Fracture, Int. J. Rock Mech. Min. Sci. & Geomech., vol. 30, No. 7, pp. 883-899
Lockner, D. A., Byerlee, J. D.	1993	How Geometric Constraints Contribute to the Weakness of the Mature Faults; Nature, 363, pp. 574-576
Manthei, G., Eisenblätter, J.	1993	Mikroakustische Messungen im Salzgestein, Kali und Steinsalz, Band 11, Heft 3/4, April 1993
McGarr, A., Simpson, D.	1997	Keynote Lecture: A Broad Look at Induced and Triggered Seismicity, Rockbursts and Seismicity in Mines, Gibowicz & Lasocki (eds.), Balkema, Rotterdam, pp. 385-396
Meredith, P. G., Main, I. G., Jones, C.	1990	Temporal Variations in Seismicity during Quasi-Static and Dynamic Rock Failure; Tectonophysics 175, 249-268
Minkley, W., Mühlbauer, J.	2005	Re-Stabilisation of the Carnallitic Working Areas in the Merkers Potash Mine, Post-Mining 2005, November 16-17, Nancy, France
Mizutani, H., Yamada, I., Masuda, K.	1985	Time-dependent Properties of Rocks and its Implications on Earthquake Prediction; Earthq. Predict. Res. 3, 595-605
Mogi, K.	1962	Study of the Elastic Shocks Caused by the Fracture of a Heterogeneous Material and its Relation to Earthquake Phenomena, Bul. Earthq. Res. Inst. 40, 125-173
Obert, L.	1941	U.S. Bureau of Mines, Rept. Invest. RI-3555
Obert, L., Duvall, W.	1942	U.S. Bureau of Mines, Rept. Invest. RI-3654
O'Connell, R. J., Budiansky, B.	1974	Seismic Velocities in Dry and Saturated Cracked Solids; J. Geophys. Re. ,79, pp. 5412-5426
Olsson, W. A.	1974	Microfracturing and Faulting in Limestone; Tectonophysics, 24, pp. 277-285
Orowan, E.	1949	Fracture and Strength of Solids; Rep. Progr. Phys. 12, 185-232
Paterson, M. S.	1978	Experimental Rock Deformation – Brittle Field, Berlin, Springer-Verlag

Peng, S., Johnson, A. M.	1972	Crack Growth and Faulting in Cylindrical Specimens of Chelmsford Granite; Int. J. Rock Mech. Min. Sci. & Geomech. Abstr. 13, 103-112
Perkins, T. K., Krech, W. W.	1966	Effects of Cleavage Rate and Stress Level on Apparent Surface Energies on Rock, J. Soc. Pet. Eng., 6: 308-314
Press, W. H., Teukolsky, S. A., Vetterling, W.	1992	Numerical Recipes: The Art of Scientific Computing, Cambridge University Press
Reid, H. F.	1910	The Mechanism of the Earthquake; The California Earthquake of April 18, 1906, Report of the State Earthquake Investigation Commission, Vol. 2, Washington, DC: Carnegie Institution, pp. 1-192
Richter, C. F.	1958	Elementary Seismology; San Francisco (Freeman)
Rong, C., Xiao-Xin, Y., Hung-Sen, X.	1979	Studies of the Fracture of Gabbro; Int. J. Rock. Mech. Min. Sci.; 16, pp. 187-193
Sammonds, P. R., Meredith, P. G., Main, I. G.	1992	Role of Pore Fluids in the Generation of Seismic Precursors to Shear Fracture; Nature 359, 228-230
Sangha, C. M., Talbot, C. J., Dhir, R. K.	1974	Microfracturing of a Sandstone in Uniaxial Compression; Int. J. Rock Mech. Min. Sci., 11, pp. 107-113
Schmitt, J., Stahlmann, J., Gattermann, J., Herrenknecht, M, Rehm, U.	2006	Numerische Simulation eines maschinellen Tunnelvortriebs mit einer Gripper-TBM, Technische Akademie Esslingen, Tagungsband 2006
Scholz, C. H.	1968a	The Frequency-Magnitude Relation of Microfracturing in Rock and its Relation to Earthquakes, Bull. Seismol. Soc. Am., 58: 399-415
Scholz, C. H.	1968b	Microfracture, Aftershocks and Seismicity, Bull. Seismol. Soc. Am., 58: 1117-1130
Scholz, C. H.	1968c	Microfracturing and the Inelastic Deformation of Rock in Compression, J. Geophys. Res. 73, 1417-1432

Scholz, C. H.	2002	The Mechanics of Earthquakes and Faulting (2nd Edition), Cambridge: Cambridge University Press
Schubert, W.	2007	Skriptum Felsmechanik und Tunnelbau, TU Graz
Semadeni, T. J.	1985	An Overview of the Past Present and Future Trends in Ground Control in the Sudbury Mining Camp; Ontario Ministry of Labour Report
Semadeni, T. J., Calder, P. N.	1990	High Frequency Microseismic Monitoring Applied to the Determination of Stress Levels in Hard Rock Mines; Rockbursts and Seismicity in Mines, Fairhurst (ed.), Balkema, Rotterdam
Shebalin, N.	1958	Correlation Between Earthquake Magnitude and Intensity; Studia Geophys. Et Geod. 2, pp. 86-87
Siebert, S.	2004	Geographie Infothek: Erdbeben, Infoblatt Erdbeben in Deutschland, Klett, Leipzig (www.klett.de)
Simmons, G., Richter, D.	1976	Microcracks in Rock, In: R.G.J. Strens (Editor), The Physics and Chemistry of Minerals and Rocks. Wiley, New York, N.Y., pp. 105-137
Sobolev, G., Spetzler, H., Salov, B.	1978	Precursors to Failure in Rock while Undergoing Anelastic Deformations; J. Geophys. Res., 83, pp. 1775-1784
Soga, N., Mizutani, H., Spetzler, H., Martin, R.J.	1978	The Effect of Dilatancy on Velocity Anisotropy in Westerly Granite; J. Geophys. Res., 83(B9): 4451-4456
Sondergeld, C.H., Estey, L. H.	1981	Acoustic Emission Study of Microfracturing during the Cyclic Loading of Westerly Granite; J. Geophys. Res., 86, pp. 2915-2924
Sondergeld, C.H., Estey, L. H.	1982	Source Mechanisms and Microfracturing during the Uniaxial Cycling of Rock, Pure Appl. Geophys., 120: 152-166
Spetzler, H. A., Sobolev, G. A., Sondergeld, C.H., Salov, B. G., Getting, I. C., Koltsov, A.	1981	Surface Deformation, Crack Formation and Acoustic Velocity Changes in Pyrophyllite under Polyaxial Loading; J. Geophys. Res., 86, pp. 1070-1080

Spies, T., Alheid, H.-J., Schulze, O.	2000	Ultraschallseismische Verfahren zur Untersuchung der hydraulischen Integrität des Gebirges; Glückauf-Forschungshefte 61 (2000) Nr. 4
Sponheuer, W.	1960	Methoden zur Herdtiefenbestimmung in der Makroseismik; Freib. Forsch.-H., C 88: 1-120, Berlin
Tan, Li	2007	Digital Signal Processing – Fundamentals and Applications, Elsevier
Taponnier, P., Brace, W. F.	1976	Development of Stress Induced Microcracks in Westerly Granite, Int. J. Rock Mech. Min. Sci. 13: 103-112
Thompson, B. D., Young, R. P., Lockner, D. A.	2006	Fracture in Westerly Granite under AE Feedback and Constant Strain Rate Loading: Nucleation, Quasi-static Propagation, and the Transition to Unstable Fracture Propagation, Pure and Applied Geophys., Band 163, Nr. 5, pp. 995-1019
Todd, T.P.	1973	Effect of Cracks on the Elastic Properties of Low Porosity Rocks, Ph.D. Thesis, Mass. Inst. Of Tech., Cambridge, Mass.
Young, R. P.	1999	Acoustic Remote Monitoring of Rock and Concrete Structures for Nuclear Waste Repositories, International Seminar on Retrievability of HLW and Spent Nuclear Fuel, Stockholm
Walsh, J. B.	1965	The Effect of Cracks in the Compressibility of Rock; J. Geophys. Res. 70, 381-389
Weeks, J. D., Lockner, A. D., Byerlee, J. D.	1978	Changes in b-Value during Movement on Cur Surfaces in Granite; Bull. of the Seismological Society of Amer. 68; 333-341
Zhaoyong, X., Naiguang G. Shirong M.	1990	Acoustic Emission m-Values of Rock Failure and Mechanic Properties in Rock; J. Seismological Res. 13, 291-297